# A CONTROL ALGORITHM TO MINIMIZE TORQUE RIPPLE AND ACOUSTIC NOISE OF SWITCHED RELUCTANCE MOTORS

# A THESIS SUBMITTED TO THE GRADUATE SCHOOL OF NATURAL AND APPLIED SCIENCES OF MIDDLE EAST TECHNICAL UNIVERSITY

BY

ERDAL BİZKEVELCİ

IN PARTIAL FULFILLMENT OF THE REQUIREMENTS FOR THE DEGREE OF DOCTOR OF PHILOSOPHY IN ELECTRICAL AND ELECTRONICS ENGINEERING

JUNE 2008

# Approval of the Thesis

# "A CONTROL ALGORITHM TO MINIMIZE TORQUE RIPPLE AND ACOUSTIC NOISE OF SWITCHED RELUCTANCE MOTORS"

submitted by ERDAL BİZKEVELCİ in partial fulfillment of the requirements for the degree of Doctor of Philosophy in Electrical and Electronics Engineering Department, Middle East Technical University by,

Prof. Dr. Canan Özgen	
Dean, Graduate School of Natural and Applied Sciences _	
Prof. Dr. İsmet Erkmen Head of Department, <b>Electrical and Electronics</b>	
Prof. Dr. H. Bülent Ertan Supervisor, Electrical and Electronics Engineering,	
Prof. Dr. Kemal Leblebicioğlu Co-supervisor, Electrical and Electronics Engineering,	
Examining Committee Members:	
Prof. Dr. Muammer Ermiş Electrical and Electronics Engineering, METU	
Prof. Dr. H. Bülent Ertan Electrical and Electronics Engineering, METU	
Prof. Dr. Kemal Leblebicioğlu Electrical and Electronics Engineering, METU _	
Prof. Dr. Işık Çadırcı Electrical and Electronics Engineering, Hacettepe Univ.	
Assist. Prof. Dr. M. Timur Aydemir Electrical and Electronics Engineering, Gazi Univ.	
Date: _	

I hereby declare that all information in this document has been obtained and presented in accordance with academic rules and ethical conduct. I also declare that, as required by these rules and conduct, I have fully cited and referenced all material and results that are not original to this work.

Name, Last Name	:	Erdal Bizkevelci
Signature	:	

# ABSTRACT

# A CONTROL ALGORITHM TO MINIMIZE TORQUE RIPPLE AND ACOUSTIC NOISE OF SWITCHED RELUCTANCE MOTORS

Bizkevelci, Erdal

Ph.D., Department of Electrical and Electronics Engineering

Supervisor	:	Prof. Dr. H. Bülent Ertan
Co-Supervisor	:	Prof. Dr. Kemal Leblebicioğlu
		June 2008, 205 pages

Despite its simple construction, robustness and low manufacturing cost, the application areas of SR motors are remained limited due to the high level of acoustic noise and torque ripple. In this thesis work, two different type of controllers are designed and implemented in order to minimize the acoustic noise and torque ripple which are considered as the major problems of SR motors. In this scope, first the possible acoustic noise sources are investigated. A sliding mode controller is designed and implemented to reduce the shaft torque ripple which is considered as a major source of acoustic noise. The performance of the controller is experimentally tested and it is observed that especially in low speed region reduction of torque ripple is significant. The torque ripple minimization performance of the controller is also tested at different speeds and the acoustic noise levels are recorded simultaneously. Comparing the noise mitigation with the noise reduction the correlation between the acoustic noise and shaft torque ripple

is investigated. The results obtained from this investigation indicated that the torque ripple is not a major source of acoustic noise in SR motors. After this finding, radial force which is the other possible acoustic noise source of SRM is taken into consideration. The effects of control parameters on radial force and the motor efficiency are investigated via simulations. With the intuition obtained from this analysis, a switching angle neuro-controller is designed to minimize the peak level of radial forces. The performance of the mentioned controller is verified through noise records under steady state conditions. Regarding to the radial force is the major source of acoustic noise. On the other hand, another controller is designed and implemented which increases the average torque per ampere value in order to increase the efficiency of the motor. It is seen that this controller has a good effect on increasing the efficiency but does not guarantee to operate at maximum efficiency.

Keywords: Switched reluctance motor, torque ripple minimization, acoustic noise minimization, sliding mode controller, advance and conduction angle controller, switched reluctance motor efficiency.

# ANAHTARLAMALI RELÜKTANS MOTORLARDA TORK DALGALANMALARINI VE AKUSTİK GÜRÜLTÜYÜ AZALTMAK İÇİN BİR KONTROL YÖNTEMİ

#### Bizkevelci, Erdal

# Doktora, Elektrik-Elektronik Mühendisliği Bölümü Tez Yöneticisi : Prof. Dr. H. Bülent Ertan Ortak Tez Yöneticisi : Prof. Dr. Kemal Leblebicioğlu Haziran 2008, 205 sayfa

Basit yapısı, sağlamlığı ve düşük üretim maliyetine rağmen yüksek işitsel gürültüsü ve şaft moment salınımı nedeniyle AR motorun uygulama alanları sınırlı kalmıştır. Bu tez çalışmasında, AR motorun önde gelen problemleri olan işitsel gürültüyü ve şaft moment salınımını enazlayan denetleyiciler tasarlanarak gerçekleştirilmiştir. Bu kapsamda, öncelikle olası gürültü kaynakları araştırılmış ve bunlardan biri olarak kabul edilen şaft moment salınımını enazlayan bir kayan kip denetleyici geliştirilmiştir. Denetleyicinin başarımı deneysel olarak sınanmış ve şaft moment salınımının özellikle düşük hız bölgesinde önemli ölçüde azaldığı gözlenmiştir. Sözkonusu denetleyicinin değişik hızlardaki başarımı eşzamanlı işitsel gürültü kayıtları ile karşılaştırılarak moment salınımı ile işitsel gürültü arasında bir ilinti olup olmadığı irdelenmiştir. Elde edilen sonuçlar doğrultusunda

şaft moment salınımının etkin bir işitsel gürültü kaynağı olmadığı kanısına varılmıştır. Bunun ardından motorun diğer olası gürültü kaynağı olan radyal kuvvetler ele alınmıştır. Motor kontrol parametrelerinin radyal kuvvetler ve motor verimi üzerindeki etkileri incelenerek bu kuvvetlerin tepe değerini enazlayan bir avans ve iletim açısı denetleyicisi yapay sinir ağı kullanılarak tasarlanmış ve gerçeklenmiştir. Sözkonusu denetleyicinin performansı sabit hız ve yük koşullarında gürültü kayıtlarıyla doğrulanarak işitsel gürültünün ana kaynağının radyal kuvvetler olduğu belirlenmiştir. Bunun yanısıra motorun verimini artırmak için ortalama birim akım başına düşen ortalama moment miktarını artıran bir denetleyici tasarlanmış ve gerçeklenmiştir. Geliştirilen verim artırıcı denetleyicinin motor verimini artırdığı ancak en yüksek verimde çalışmayı garanti etmediği sonucuna varılmıştır.

Anahtar kelimeler: Anahtarlamalı relüktans motor, şaft moment salınım azaltımı, işitsel gürültü azaltımı, kayan kip denetleyici, avans ve iletim açısı denetleyicisi, anahtarlamalı relüktans motor verimi.

To My Beloved Wife Sezin

# ACKNOWLEDGEMENTS

I wish to thank my supervisor Prof. Dr. H. Bülent Ertan for his guidance, insight and suggestions throughout the research.

I would like to express my deepest gratitude to my co-supervisor Prof. Dr. Kemal Leblebicioğlu for the theoretical support and getting me out of the deadlocks for many times.

I gratefully thank Prof. Dr. Muammer Ermiş, Assist. Prof. Dr. M. Timur Aydemir and Prof. Dr. Işık Çadırcı for participating in my thesis defence committee and expressing their suggestions in order to make the necessary corrections.

I wish to express my sincere appreciation to Abdullah Nadar who showed me a generous tolerance and maturity during my hard times and presented a great research environment with his management experience.

I am always indebted to İlhan Gürpınar, Dilaver Yurdagül, Doğuhan Özer and Erdinç Berke for their support in my hardware development and test bench construction period.

The invaluable support of Levent Burak Yalçıner who allocated his time for the finite element analysis of the test motor is gratefully acknowledged.

The interest of the benevolent members of Hardware Development and Power Systems Group of TÜBİTAK-UZAY in my research is much appreciated but I especially wish to emphasize my grateful thanks to my talented colleagues Muhammed Raşid Paç and Doğan Gezer for setting me partially free by taking my professional engineering workloads over as much as possible.

I gratefully thank Erdoğan Güner for his criticism, sincerity and kindness. His deep experiences in both engineering and personal subjects always gave me light and hope.

The financial support of TÜBİTAK to this research as a scientific project is gratefully acknowledged (Project No: 106E033, Armoden).

I would like to thank Arçelik A.Ş., Uğur Kan and Bülent Küçükcoşkun for allocating their valuable time, laboratory and technical infrastructure for the acoustic noise measurements of the test motor.

I wish to express my grateful thanks to Assist. Prof. Dr. Ahmet M. Hava who always gave me inspiration, encouragement and invaluable engineering hints in my hopeless times. The research environment he established made me breathe the air of a school of power electronics. His talented group members Ömer Göksu, Fuat Onur Bağlan, Osman Selçuk Şentürk and Mehmet Can Kaya got me to feel in confidence with their handy engineering support as well as the hot drink service during the cold and long laboratory nights. I also wish to thank Deniz Durdağ for the sound recordings of the SRM drive. Finally, I wish to express my deepest gratitude to my beloved wife Sezin who showed me amazing indulgence, patience and respect throughout the seemingly endless study. Regardless of any kind of results of the research period, I truly owe her a great apology and beg her pardon for being a nervous, careless, impatient and unkind husband during the twilight years of my endeavour.

# **TABLE OF CONTENTS**

ABSTRA	.CTiv
ÖZ	
ACKNO	WLEDGEMENTSix
TABLE (	OF CONTENTSxii
СНАРТЕ	ERS
1. IN	<b>FRODUCTION1</b>
1.1.	Background 1
1.2.	Basic description of SRM
1.3.	Historical review
1.4.	<i>Objective of the Thesis</i> 7
1.5.	Outline of the Thesis
2. SR	M SIMULATOR
2.1.	Previous Work
2.2.	Model of the SRM
2.3.	Electrical System
2.4.	Mechanical System
2.5.	SRM State Equations
2.6.	Converter Operation
2.7.	SRM Simulator
2.7	7.1. Static Torque Curve Measurements
2.7	7.2. Flux Linkage Measurements
2.7	7.3. Determination of the Rotational Inertia and the Friction
Co	pefficients
2.7	7.4. Simulator Block Diagram
2.8.	Angle Definitions

2.8	8.1.	Electrical Position
2.8	3.2.	Per Unit Angle
2.8	3.3.	Advance Angle
2.8	3.4.	Conduction Angle
2.9.	Verifi	cation of the SRM Simulator Torque Predictions
2.10.	Verifi	cation of the SRM Simulator Current Waveform Predictions 38
3. TO	RQUE	RIPPLE MINIMIZATION OF SRM DRIVES 41
3.1.	Introd	luction
3.2.	Previ	ous Work
3.3.	A Slic	ling Mode Controller to Minimize SRM Torque Ripple51
3.3	3.1.	Controller Design
3.3	3.2.	Controller Implementation
3.3	3.3.	SRM Model
3.3	3.4.	Sliding Mode Control (SMC)55
3.3	3.5.	SMC Design
3.3	3.6.	Simulation Results
3.3	3.7.	More realistic simulation results
3.3	3.8.	Hardware Implementation67
3.3	3.9.	Experimental Results
3.3	3.10.	Acoustic Noise Measurements
3.4.	Concl	lusions77
4. EFI	FECTS	S OF ADVANCE AND CONDUCTION ANGLES ON SRM
CONT	ROL	
4.1.	Const	ant Speed Variable Advance and Conduction Angles Simulations
	80	
4.2.	The E	ffect of Torque Ripple on SRM Acoustic Noise
4.3.	Conci	lusion
5. AC	OUST	IC NOISE IN SRM DRIVES 103
5.1.	Previ	ous Work

	5.2. Acoi	<i>ustic Noise Sources in SRM Drives</i>	108
	5.2.1.	Magnetic Noise Sources	110
	5.2.2.	Stator Reaction	112
	5.2.2.1	Effect of the radial force component on the stator yoke	113
	5.2.2.2	Effect of the tangential force component on the stator pole	115
	5.2.3.	Rotor Reaction	118
	5.2.4.	Frequency of the tangential and radial forces:	119
	5.2.5.	Acoustic Noise Stemming From Radial Forces	123
	5.2.5.1	Acoustic Noise Model of the Stator	123
	5.2.5.2	Radial Force Data	126
	5.2.5.3	Model Parameters	128
	5.2.6.	Solution Suggestion	130
6	. A CONT	ROLLER DESIGN TO MINIMIZE ACOUSTIC NOISE	IN
S	RM DRIVI	ES	134
	6.1.1.	The Effects of Control Parameters on Radial Forces	134
	6.1.2.	Efficiency	143
	6.1.3.	Experimental Results	144
	6.1.4.	Controller Block Diagram	150
	6.1.5.	An Introduction to Feedforward Neural Networks	151
	6.1.6.	Proposed Neuro-controller	158
	6.1.6.1	Neural Network Training	160
7	. ACOUST	FIC NOISE MEASUREMENTS AND CONCLUSIONS	164
	7.1. Intro	oduction to Acoustic Noise and its Measurement	164
	7.2. Qua	ntification of Acoustic Noise	165
	7.2.1.	Sound Power Level (SWL or $L_w$ )	165
	7.2.2.	Sound Pressure (SPL or L <sub>p</sub> )	166
	7.2.3.	Sound Intensity (I)	167
	7.2.4.	Add, subtract and average sound pressure:	169
	7.2.5.	Octave Band Analysis	170

7.2.6.Sound Perception of Human Ear173				
7.2.7. Calculation of A-Weighted Sound Power Level from one-th				
octave-band sound levels 176				
7.3. Noise Measurements of the Test Motor				
7.4. Conclusions				
REFERENCES 190				
A. SPECIFICATIONS OF THE EQUIPMENT 195				
A.1. Dimensions, Electrical and Magnetic Properties of the Test Motor 195				
A.3 Other Equipment				
B. CALCULATION OF THE ROTATIONAL INERTIA AND THE				
FRICTION CHARACTERISTICS OF THE DRIVE TRAIN				
B.1 Rotational Inertia of the Drive Train:				
B.2 Friction coefficients				
CURRICULUM VITAE				

# **CHAPTER 1**

# **INTRODUCTION**

In this chapter, an introduction to switched reluctance motors is given to highlight the objectives and the roadmap of the thesis. First, the general definitions and the physical structure of the motor is defined as simple as possible to form a picture of the operation. Second, after a short meeting with the machine, the mathematical expressions and the basic theory of operation are summarized to perceive the problem to be solved. Third, the advantages and disadvantages of the machine are emphasized. Fourth, a historical review of the previous work is given to apprehend the effort made to domesticate the motor. Fifth, the objectives, motivations and the methodology of the thesis are presented. After this disclosure of the roadmap, the outline of the thesis is given as the final step of the introductory chapter.

## 1.1. Background

The theory of variable reluctance motors was established by 1838 but these are under interest since 1960's with the developments in high-power semiconductor switching devices. First application areas investigated for these devices were positioning applications. In the early 1970's, it was noticed that doubly salient motors can be used for continuous variable speed applications. The main acceleration of research falls into late 1980's with the cheapening and picking up microprocessors.

## 1.2. Basic description of SRM

The economical and technical attraction of the motor come from its simple and rugged construction. Both the physical simplicity or the mathematical complexity of the machine come from the same reason: Having salient poles on either the stator or the rotor side (Figure 1). It has windings only on the stator side and no other current carrying parts or magnets on the rotor (Figure 2).

The main distinguishing feature of the SRM is the need for a power electronic device and its microprocessor based controller with the required position feedback even for an ordinary rotation. Note that, since the switched reluctance motor is motionless without its controller, it must be considered as an integral motor and the cost comparison must be made with any type of the motor which is presented with its controller.

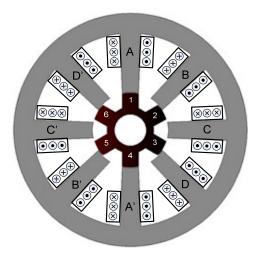


Figure 1 A four phase 8/6 SRM structure

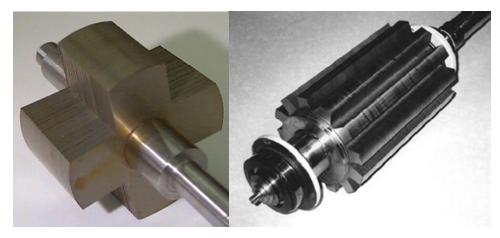


Figure 2 SRM rotors with 4 and 12 poles.

Over the past decade, since the efficiency, noise and speed control is more important than before, nearly none of the motors are used without a controller. This predilection of application areas makes SRM an important salient alternative among the other controlled competitors.

## **Advantages of SRM**

- It has a good starting torque, since the torque is proportional to the square of current.
- High speed and/or wide constant power speed range,
- Low energy losses in both the rotor and power electronics,
- Highly robust, both mechanically and electrically,
- Properly designed and controlled, the motor yields high efficiency across a very wide range of load conditions,
- The rotor structure is simple and easy to manufacture,
- Cooling is easy because, most of the heat is generated in stator,

- It only requires unidirectional current to achieve four quadrant operation, resulting less than two switching devices per phase,
- No shoot through problem, assuring high reliability,
- Can continue operation even a failure of one phase,
- Reduces number of switches which reduces cost.

## **Disadvantages of SRM**

- High acoustic noise,
- High torque ripple,
- Requires at least one current sensor sensing the DC link current, and one position transducer,
- The inductance characteristic of the stator winding is dependent on both the rotor position and current. For this reason, a linear model with constant circuit parameters is not possible.
- It requires a controllable converter which is expensive for constant speed applications,
- The cabling is more complex than induction motor drives,

Generally, SRM is chosen for the applications where a brushless drive is required with a wide speed range, and also if the cost saving is important.

### **Basic Theory of Operation**

SRM has a stroke based operation and in each step, the rotor poles tend to align the excited stator pole couple. Successively excited stator coils result with the rotor movement. The number of steps in each rotor revolution can be calculated as follows:

$$N_{step} = N_{phase} . N_{rotor} \tag{1}$$

In general, SRM phase number is half of the stator pole number so it is more convenient to express the number of strokes per revolution as follows:

$$N_{step} = \frac{N_{stator} \cdot N_{rotor}}{2} \tag{2}$$

In each stroke, the phase current produces a flux which tends the rotor pole to align to the excited stator pole (Figure 3). The magnetic attraction between the stator and the rotor poles is a function of the phase current and the rotor position. In general, *phase position* term is used instead of *rotor position* since both terms refer to the angle between the stator and the rotor poles.

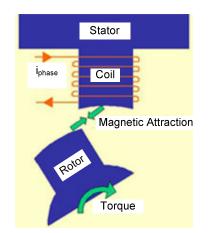


Figure 3 Rotor pole attracted by the excited phase.

There are  $N_s$  strokes in each rotor revolution so the angle difference between two successive aligned positions of the rotor can be defined as the step angle:

$$\theta_{step} = \frac{2 \cdot \pi}{N_{step}} \tag{3}$$

Substituting (2) into (3) gives the step angle as a function of the stator and the rotor pole numbers:

$$\theta_{step} = \frac{2 \cdot \pi}{\frac{N_{stator} \cdot N_{rotor}}{2}}$$
(4)

#### **1.3.** Historical review

The Davidson's electric motor, which is known as the first SRM, was presented in the late 1830s, only twenty years after the invention of the electromagnetism by Oersted. After 40 years, the invention of the induction motor by Tesla in 1880 shaded SRM until the early 1970s. Both the drawbacks of the motor and the technological deficiencies averted the pervasive usage of it over a century. As it is well known, the other plug and play motors, such as *direct current* or *induction machines*, did not need extra equipment for decades. Therefore they dominated the industrial and house applications over a century without a requirement of a drive.

The drawbacks of the motor appeared not only in practical applications, but also during theoretical modeling. Although the SRM construction and operating principle is so simple to understand, it couldn't be possible to find an efficient method for modeling it to make detailed performance and efficiency analysis for a long time. In [1], Stephenson and Corda presented a computationally efficient method for performance estimation of SRM by using measured or computed  $\lambda_{phase}$ –  $i_{phase}$  -  $\theta_{phase}$  data. In [3], the fundamental design considerations of the motor are presented with practical examples and it is shown that the motor has higher efficiency than the induction motor in same frame size.

Although the major technological counterchecks of SRM drive were overcome with the cheapening switching devices and microprocessors, a rough investigation of the motor operation yields two major problems: Acoustic noise and shaft torque ripple. In this study, the correlation between these two problems will be discussed in details.

# **1.4.** Objective of the Thesis

The main motivation and objective of the thesis is to determine the key factors of SRM acoustic noise and to develop a controller to minimize torque ripple and acoustic noise considering the drive efficiency.

# **1.5.** Outline of the Thesis

The outline of the thesis is given in Figure 4.

Chapter 1: Introduction
Chapter 2: SRM Simulator
Chapter 3: Torque Ripple Minimization of SRM Drives
Chapter 4: Effects of Advance and Conduction Angles on SRM
Chapter 5: Acoustic Noise in SRM Drives
Chapter 6: A Controller Design to Minimize Acoustic Noise in SRM Drives
Chapter 7: Acoustic Noise Measurements and Conclusions

Figure 4 Outline of the thesis

## **CHAPTER 2**

# **SRM SIMULATOR**

To develop a controller for any physical system, it is highly desirable to have a realistic simulator based on the mathematical model. By using a reliable simulator, the responses of the system in various situations and the effects of the control parameters can be understood well enough before the hardware implementation. In this chapter, first the previous studies modeling SRM are reviewed. Then, a suitable model is selected. Following this, solution of the model is presented. Finally the drive converter is added to the model to complete the simulation software. The reliability of the software is ascertained by the experiment and simulation results.

## 2.1. Previous Work

Most of the electric motor types are satisfactorily modeled by using the phase current as the state variable. Contrary to the conventional AC and DC machines, SRM is supposed to operate under heavy saturation in order to increase the torque production capability [1]. Therefore, modeling and simulation is more complex than the formers.

In [2] Stephenson and Corda presented a method to overcome magnetic nonlinearity problem. They used flux-linkage as the state variable of the motor instead of the phase current. In order to calculate the phase current from the flux-linkage

and position, quadratic interpolation is used with the data which is generated by inverting the flux-linkage curves. In [3], phase torque is calculated by numerical differentiation of the co-energy. Torrey and Lang presented a method to model the magnetization curves by exponential functions of current and position [4]. In [5], Pulle proposed a curve fitting method to avoid inverting the flux-linkage curves. In [6] Miller and McGilp presented a computationally efficient method to estimate the SRM performance from only the aligned and unaligned flux-linkage curves. In [7], Soares and Branco developed a simulator based on Matlab/Simulink environment with the idea of using both flux-linkage and static torque curves to estimate the machine performance. In their study, first a linear model is presented and then a non-linear SRM model is used. For non-linear modeling, the fluxlinkage and static torque curves obtained from finite-element analysis (FEA) is used. Lopez and Rajashekara also mentioned about an SRM simulator which uses non-linear data for both flux-linkage and static torque curves obtained from FEA [8]. Both [7] and [8] show that, with modern computers and technical computing software packages such as Matlab, give a great flexibility of dynamical modeling of SRM. In [7] and [8], built-in cubic-spline interpolation functions of Matlab are used to obtain the flux-linkage and torque from the non-linear  $\lambda_{phase} - i_{phase}$  - $\theta_{phase}$  and  $T_{phase} - i_{phase}$  -  $\theta_{phase}$  data. By this approach, the measured flux-linkage and static torque curves can be used as well as the FEA results for both fluxlinkage and torque calculations.

#### 2.2. Model of the SRM

If an electromechanical system is under investigation, the mathematical model is composed of three main components: Electrical, mechanical and thermal. To perform a full performance analysis of any electromechanical energy conversion system, the mathematical model must involve these sub-systems. Thermal analysis is beyond the scope of this study so only the electrical and mechanical systems are focused on. The complete solution of the mechanical and electrical states of the system is obtained by solving the relevant state equations simultaneously. In this part of the thesis, the electrical and mechanical components of the drive will be investigated.

## 2.3. Electrical System

The electrical system includes the phase current, phase voltage and the phase fluxlinkage. In this chapter, the input, output variables and the system parameters of the electrical system will be examined thoroughly.

An SRM is doubly salient machine (Figure 5). The magnetic circuit is saturated during operation and the saturation pattern is both current and rotor position dependent. Therefore, obtaining a linear equivalent circuit of an SRM is not possible.

Ideally speaking, all SRM phases are accepted to be identical so instead of dealing with the complete machine, it is more convenient to investigate the characteristics of a single phase, just like in other multi-phase systems.

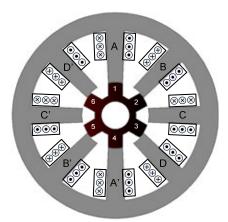


Figure 5 Cross-sectional doubly salient view of SRM.

First of all, the physical model must be given to have an initial point of the investigation. The electrical and mathematical model will be based on this model. As seen in Figure 6, SRM phase is an RL circuit with a non-linear inductor.

The voltage equation of an RL circuit including a non-linear inductor is as follows:

 $V_{phase} = i_{phase} \cdot R_{phase} + \frac{d\lambda_{phase}(\theta_{phase}, i_{phase})}{dt}$ 

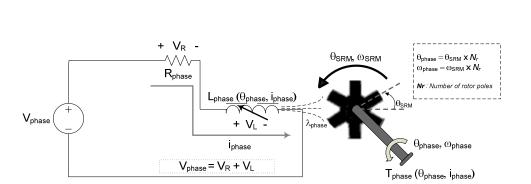


Figure 6 Single phase equivalent circuit of an SRM with a simplified two level drive

Re-organizing (5) gives the differential equation for the phase flux-linkage:

$$\frac{d\lambda_{phase}(\theta_{phase}, i_{phase})}{dt} = V_{phase} - i_{phase}.R_{phase}$$
(6)

(5)

For an m phase SRM, (6) can be formed to give the electrical state equations as follows:

$$\frac{d\lambda_j(\theta_j, i_j)}{dt} = V_j - i_j R_j, \quad j = 1, 2, \dots m$$
(7)

This equation reveals the relation between the electrical states of the motor which are composed of phase flux-linkage, current and voltage.

## 2.4. Mechanical System

The mechanical system variables of an SRM are *mechanical torque*, *angular speed* and *angular acceleration*. The differential equations defining the mechanical states are as follows:

$$\frac{d\theta_{mech}}{dt} = \omega_{mech},$$

$$\frac{d\omega_{mech}}{dt} = \frac{1}{J_{total}} \cdot \left(T_{elec} - T_{load} - T_{f\&w}\right)$$
(8)

The electrical torque is composed of the algebraic sum of the phase torques

$$T_{elec} = \sum_{j=1}^{m} T_j \left( \theta_j, i_j \right), \quad j = 1, 2, ...m$$
(9)

Substituting (9) into (8) gives the mechanical state equations:

$$\frac{d\theta_{mech}}{dt} = \omega_{mech},$$

$$\frac{d\omega_{mech}}{dt} = \frac{1}{J} \cdot \left( \left( \sum_{j=1}^{m} T_j \left( \theta_j, i_j \right) \right) - T_{load} - T_{f\&w} \right), \quad j=1,2,...m$$
(10)

Since SRM is operated under saturation, the relation between the torque and current is a non-linear function.

$$T_{phase}\left(\theta_{phase}, i_{phase}\right) = f\left(\theta_{phase}, i_{phase}\right)$$
(11)

In the literature, there are various approaches for representing the SRM torque function such as linearization, Fourier series expansion or neural networks. In this study measured static torque curves are used so no approximation is made for this function.

## 2.5. SRM State Equations

Combining (7) with (10) gives the mathematical model of an m phase SRM as follows:

$$\frac{d\lambda_{j}(\theta_{j}, i_{j})}{dt} = V_{j} - i_{j} \cdot R_{j}$$

$$\frac{d\theta_{mech}}{dt} = \omega_{mech},$$

$$\frac{d\omega_{mech}}{dt} = \frac{1}{J} \cdot \left( \left( \sum_{j=1}^{m} T_{j}(\theta_{j}, i_{j}) \right) - T_{load} - T_{f\&w} \right), \quad j=1,2,...m$$
(12)

Instantaneous SRM position, speed, current and torque are obtained by solving the state equations given in (12). The simulator used in this study is based on these state equations and the solution is obtained by Simulink with fourth order Runge-Kutta solver with a fixed step size of 5  $\mu$ sec (Figure 7).

🥠 Simu	lation Parame	ters: SRMo5			×
Solver	Workspace I/0	Diagnostics	Advanced	Real-Time \	/orkshop
	ation time time: 0.0	Stop tim	e: inf	_	
	Fixed-step	▼   ode4 (i	Runge-Kutta)		•
Fixed	step size: 5e-6	'	Mode: MultiT	asking 👱	]
Outpu	ut options				
Refe	ne oulpul	<u>×</u>	Refine la	ctor 1	
		OK	Cancel	Help	Apply

Figure 7 The differential equation solver settings of Matlab Simulink® used during SRM simulations.

## 2.6. Converter Operation

The most commonly used SRM drive converter topology is given in Figure 8. With this type of asymmetric H bridge inverter configuration,  $(-V_{DC})$ , 0 and  $(+V_{DC})$  is applicable.

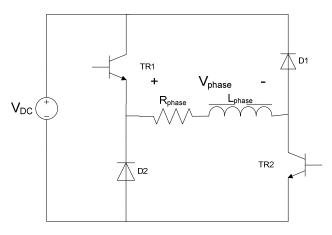


Figure 8 Three level inverter used for driving an SRM phase

In Figure 9, a classical inverter topology is given for a four phase SRM. As it is seen, identical circuitry is used for each SRM phase. That's why investigation of the single phase gives enough intuition about the multi-phase drive.

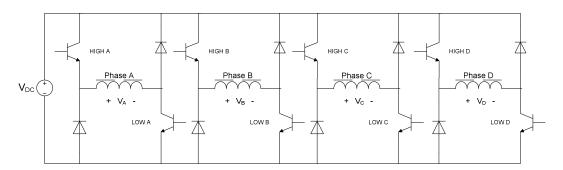


Figure 9 Complete inverter configuration for a four phase SRM.

In this type of inverter, there are three modes of operation for each phase independently from each other. These are:

1.	Energizing period	: Positive voltage input (Figure 10, Mode 1)
2.	Free-wheeling period	: Zero voltage input (Figure 10, Mode 2)
3.	De-energizing period	: Negative voltage input (Figure 10, Mode 3)

The asymmetric H bridge modes are summarized in (13) and Figure 10.

$$V_{phase} = \begin{cases} +V_{DC}, & TR_{1}, TR_{2} ON, D_{1}, D_{2} OFF & Mode 1 \\ 0, & TR_{1}, D_{1} ON, TR_{2}, D_{2} OFF, Mode 2 \\ -V_{DC}, & TR_{1}, TR_{2} OFF, D_{1}, D_{2}, ON, Mode 3 \\ OFF state, & TR_{1}, TR_{2}, D_{1} and D_{2} OFF, Mode 4 \end{cases}$$
(13)

The modes of converter operation and typical current waveform at low speed is as shown in Figure 10. The chopper action and the switching angles are also indicated in this figure.

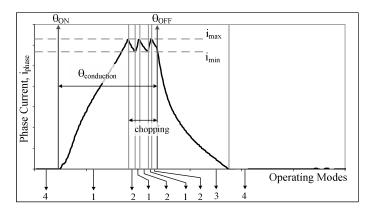


Figure 10 Operating modes of converter on phase current waveform

The phase voltage equations of the operation modes are given in (14), (15) and (16).

$$+V_{DC} = i_{phase} \cdot R_{phase} + \frac{d\lambda_{phase}(\theta_{phase}, i_{phase})}{dt}, \quad Mode \ 1$$
(14)

$$0 = i_{phase} \cdot R_{phase} + \frac{d\lambda_{phase}(\theta_{phase}, i_{phase})}{dt}, \quad Mode \ 2$$
(15)

$$-V_{DC} = i_{phase} \cdot R_{phase} + \frac{d\lambda_{phase}(\theta_{phase}, i_{phase})}{dt}, \quad Mode \ 3$$
(16)

If the phase voltage is chosen as the control variable, DC link voltage is no more used directly. Instead, a PWM duty cycle controlled variable phase voltage is applied to the motor phase:

$$V_{phase} = i_{phase} \cdot R_{phase} + \frac{d\lambda_{phase}(\theta_{phase}, i_{phase})}{dt}$$
(17)

For an m phase SRM, (17) can be formed to give the electrical state equations as follows:

$$\frac{d\lambda_j(\theta_j, i_j)}{dt} = V_j - i_j R_j, \quad j = 1, 2, \dots m$$
(18)

This equation reveals the relation between the electrical states of the motor which are composed of phase flux-linkage, current and voltage.

# 2.7. SRM Simulator

The simulator used in this study is based on the differential equations given in (12). To solve these differential equations, initial conditions of the state variables are required. The initial mechanical rotor position is taken such that phase A resides at its zero advance angle position.

$$\left[\boldsymbol{\theta}_{a}\right]_{t=0} = 0.25 \ p.u.(electrical) \tag{19}$$

The initial conditions of the phase A state variables are taken as follows:

$$\begin{bmatrix} \boldsymbol{\theta}_{a} \\ \boldsymbol{\omega}_{r} \\ \boldsymbol{\lambda}_{a} \end{bmatrix}_{t=0} = \begin{bmatrix} 0.25 \text{ p.u.} \\ 0 \text{ rpm} \\ 0 \text{ Wb-t} \end{bmatrix}$$
(20)

The solution procedure of the state space variables are given in Figure 11.

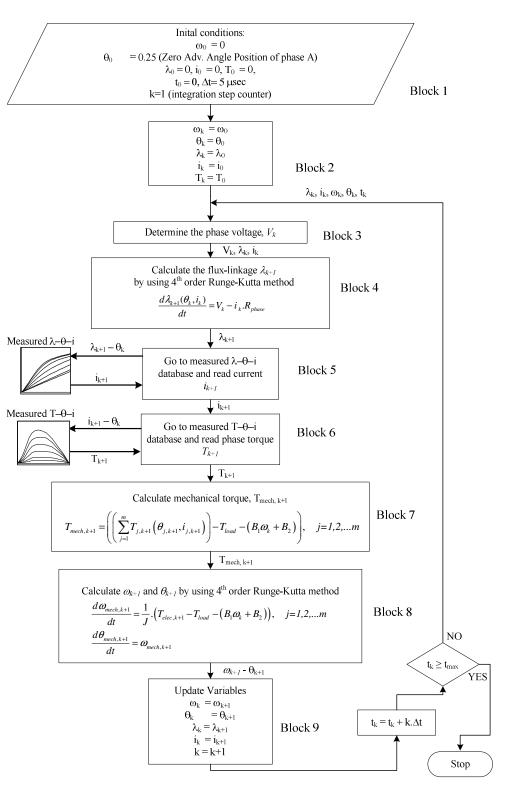


Figure 11 The solution procedure of the SRM state equations.

# Block 3

The phase voltage determination procedure according to the phase position is as given in Figure 12.

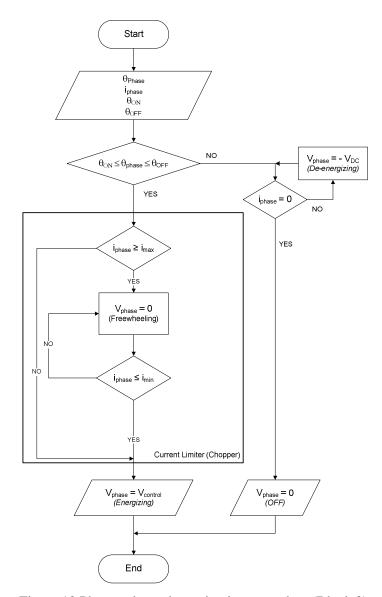


Figure 12 Phase voltage determination procedure (Block 3).

## **Block 4**

To calculate the flux-linkage, fourth order Runge-Kutta method is selected as the solver type in Matlab Simulink<sup>®</sup> with a step size of 5  $\mu$ sec. The solution procedure

is given in Figure 13. The differential equation solver settings of the Matlab Simulink<sup>®</sup> are shown in Figure 7.

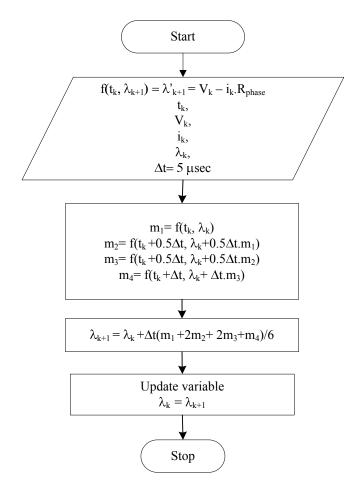


Figure 13 Calculation of flux-linkage by using fourth order Runge-Kutta method.

### Block 5

In this block the phase current of the test motor is obtained by using its measured  $\lambda$ - $\theta$ -i curves for the default values of the phase flux-linkage and position. First at position  $\theta_k$  the  $\lambda$ - $\theta$ -i curve family is interpolated and a single  $\lambda$ -i curve is obtained for  $\theta_k$  (Figure 14, Block 5.1). Then for the flux linkage value  $\lambda_k$  the corresponding current is found from the obtained  $\lambda$ -i curve at  $\theta_k$ . Details of the procedures followed are explained below.

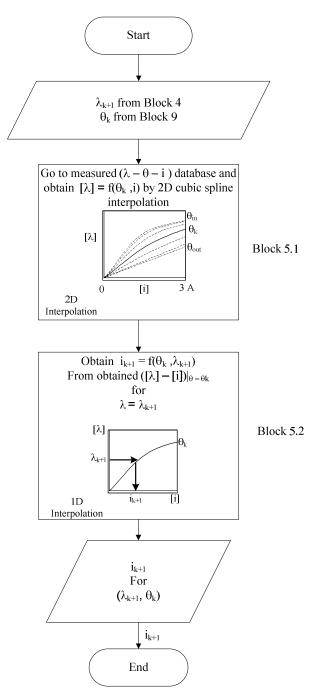


Figure 14 Phase current determination procedure from flux-linkage and position (Block 5).

Block 5.1

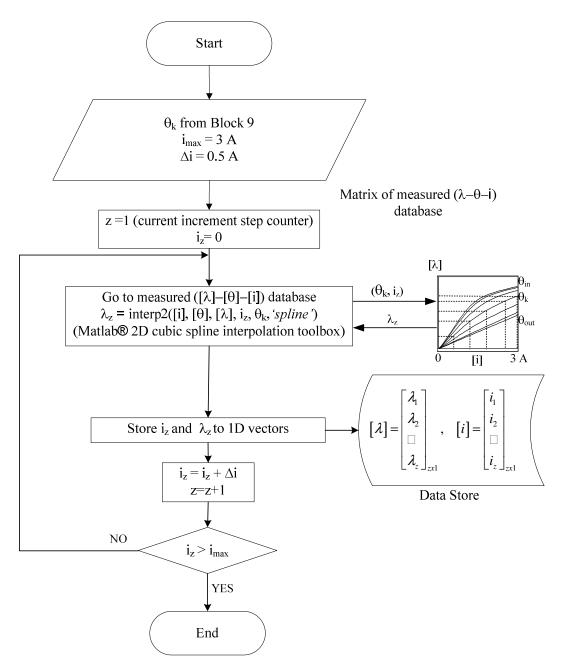


Figure 15 Obtaining one-dimensional flux linkage - current vector for an intermediate phase position (Block 5.1).

## Block 5.2

The procedure for obtaining the phase current from the flux-linkage is given in Figure 16.

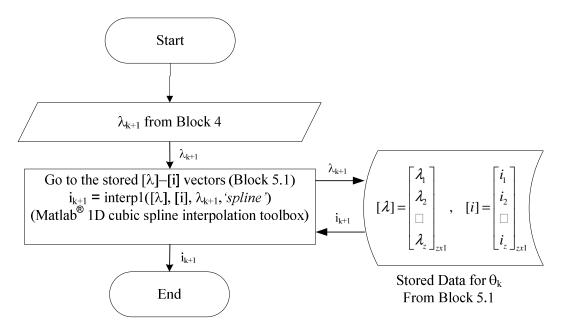


Figure 16 Obtaining phase current vector for the given phase position (Block 5.2).

## **Block 6**

As a result of the applied phase voltage and instantaneous the rotor position, the motor produces electrical torque. This produced torque accelerates the motor with an inversely proportional with the rotational inertia, J.

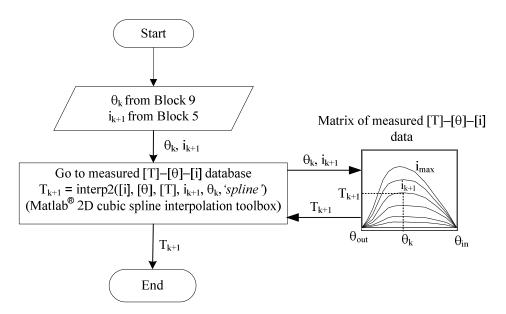


Figure 17 Phase torque calculation procedure for given position and current (Block 6).

The two dimensional interpolation settings of the Matlab Simulink<sup>®</sup> toolbox used for torque calculation is given in Figure 18.

ock Parameters: Look-Up Table (n-D)1	2
LookupNDInterp (mask) (link)	
Perform n-dimensional interpolated table lookup including index The table is a sampled representation of a function in N variable treakpoint est relate the input values to positions in the table. dimension corresponds to the top (or left) input port.	61.
Parameters	
Number of table dimensions: 2	
First input (row) breakpoint set:	
angle_vector	
Second (column) input breakpoint set:	
current_vector	
Index search method: Binary Search	-
Begin index searches using previous index results	
Use one (vector) input port instead of N ports	
Table data:	
torque_theta_current_matrix	
Interpolation method: Cubic Spline	•
Extrapolation method: Linear	-
Action for out of range input: None	

Figure 18 Two dimensional interpolation settings of Matlab Simulink<sup>®</sup> built in look-up table for torque calculation.

## 2.7.1. Static Torque Curve Measurements

In the simulations here measured static torque curves are used. The measured static torque curves of the test motor are given in Figure 19. In these experiments, the static torque curves are obtained for  $20^{0}$  electrical degrees of rotor position steps. The experimental setup and the step by step procedure used for obtaining static torque curves are given in Figure 20 and Figure 21. For each position, the rotor is fixed manually and the current swept from 0 to 3 A in 0.5 A steps. At each current value shaft torque is recorded manually.

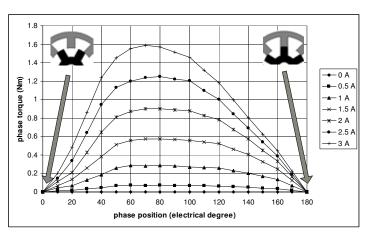


Figure 19 Measured static torque curves of the test motor.

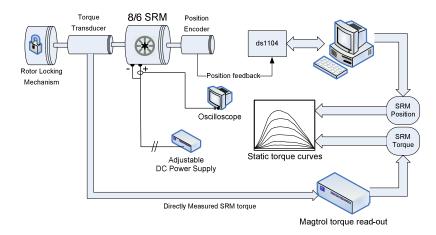


Figure 20 Experimental setup used for static torque measurements.

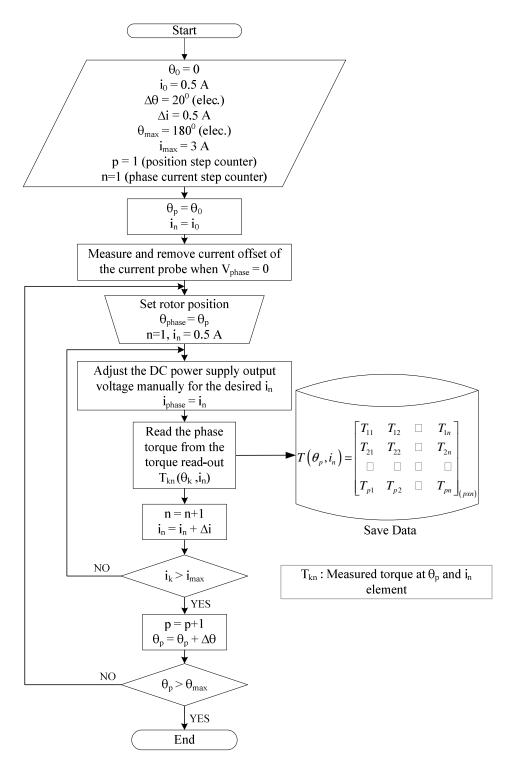


Figure 21 Static torque curve measurement procedure where  $T_{pn}$  represents the measured torque at  $\theta_p$  and  $i_n$  element.

After obtaining and storing the measured static torque curves in a matrix, Matlab Simulink<sup>®</sup> 2-D Look-up table is used for the estimation of the motor torque for any phase current and position using cubic-spline interpolation during simulations (Figure 18).

## 2.7.2. Flux Linkage Measurements

In this study, measured flux-linkage characteristics are used. The measurement is based on the method proposed by Cheok and Wang [40]. In this method, the instantaneous phase voltage and current are measured during phase excitation and the flux-linkage is calculated by the numerical integration of the phase voltage (21).

$$\lambda(t) = \lambda_0 + \int_0^t (V(t) - i(t).R).dt$$
(21)

Here,  $\lambda_0$  is the initial flux-linkage of the phase at t=0. The phase voltage and current data is numerically recorded by a digital oscilloscope which uses USB memory stick as the data storage element. The sampling period of the oscilloscope during the experiment is 50 µsec. The stored data is then exported to Matlab<sup>®</sup> workspace and the integration is performed using the improved Euler's formula:

$$\lambda_{k} = \lambda_{k-1} + \frac{\Delta T \left( V_{k} + V_{k-1} - Ri_{k} - Ri_{k-1} \right)}{2}, \quad \lambda_{0} = 0$$
(22)

Here, k is the integration step number and  $\lambda_k$  is the flux-linkage at the k<sup>th</sup> step. The integration step time ( $\Delta T$ ) is taken as 50 µsec which is same with the sampling period of the digital oscilloscope. The flux-linkage measurement procedure is given in Figure 22. The obtained flux-linkage curves are stored in a 2D matrix. The flux linkage data is stored with 0.2 A current steps by resampling the current data. During resampling, Matlab<sup>®</sup> cubic spline interpolation toolbox is used so if the current steps does not coincide with the sampled current values, the current

data is obtained by cubic spline interpolation. The position step size is  $30^{\circ}$  (electrical) as seen in Figure 23.

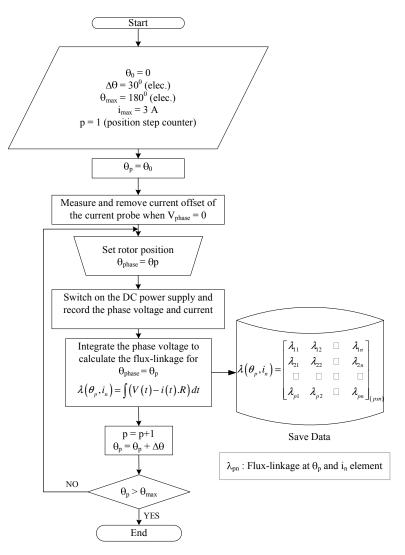


Figure 22 Flux-linkage characteristics measurement procedure.

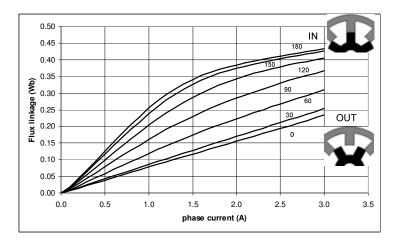


Figure 23 Measured flux-linkage versus phase current at different positions of the rotor  $(\Delta \theta = 30^{0} \text{ elec.}, \Delta i=0.2 \text{ A})$ 

The experimental setup for the flux-linkage measurement is given in Figure 24. The circuitry used for the phase excitation is shown in Figure 25. This circuit configuration is obtained by shorting the low-side IGBT collector-emitter terminals by a hard wire (Figure 8. TR2). After by-passing this IGBT, the high-side TR1 is switched ON by the controller (dSPACE<sup>®</sup> 1104) and this signal is used to trigger the digital oscilloscope.

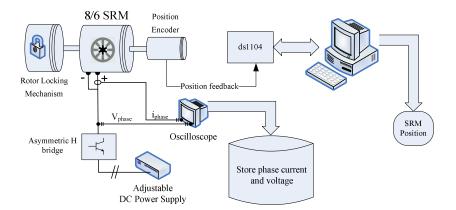


Figure 24 The experimental setup for flux-linkage measurements

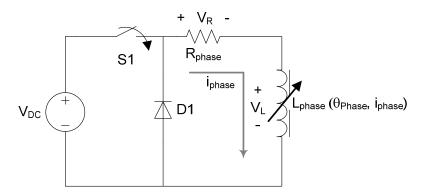


Figure 25 The circuitry used for flux-linkage measurements.

## 2.7.3. Determination of the Rotational Inertia and the Friction Coefficients

The rotational inertia value of the SRM is calculated as  $157 \times 10^{-5} \text{ kg.m}^2$  by using its physical dimensions and material properties. The other test equipment inertia values are obtained from the manufacturer datasheets. The details of the inertia calculations are given in APPENDIX B.

The friction coefficients of the system is affected from the drive alignment, mounting, operating conditions, etc so it cannot be calculated directly but it can be obtained by experiments.

In general, the friction losses of any system can be modeled as follows:

$$T_{f\&w} = B_n . \omega^n + B_{n-1} . \omega^{n-1} + K + B_1 . \omega + B_2$$
(23)

In this study, the last two term of (23) is taken into consideration and the higher order terms are ignored:

$$T_{f\&w} = B_1.\omega + B_2 \tag{24}$$

According to the Newton's second law of motion, the differential equation of any rotational mass is given as follows:

$$T_{elec} = J \cdot \frac{d\omega}{dt} + T_{load} + B_1 \cdot \omega + B_2$$
(25)

In order to solve (24) and (25) simultaneously,  $T_{elec}$  and  $T_{load}$  must be eliminated from the system. To do this, a free deceleration experiment may be used. If the mechanical excitation of the system is shut down while it is operating at constant speed, it will settle down in a finite time with the effect of the friction losses. During this free deceleration period the electrical and the load torque ( $T_{electrical}$  and  $T_{load}$ ) in (28) will disappear:

$$0 = J \cdot \frac{d\omega}{dt} + B_1 \cdot \omega + B_2 \tag{26}$$

In this study, the rotational system is accelerated up to 2000 rpm and then the excitation of the system is cut off during constant speed operation. The speed curve recorded during deceleration is used to obtain the solution of the differential equation given in (26). The experimental data used for the friction and windage loss determination is given in APPENDIX B. The friction and windage losses of the system is obtained as follows:

$$T_{f\&w} = 3.74.10^{-5}.n + 0.063 Nm \tag{27}$$

In this study, this equation is used for estimating the friction and windage losses of the system.

## 2.7.4. Simulator Block Diagram

The block diagram of the simulator is given in Figure 26.

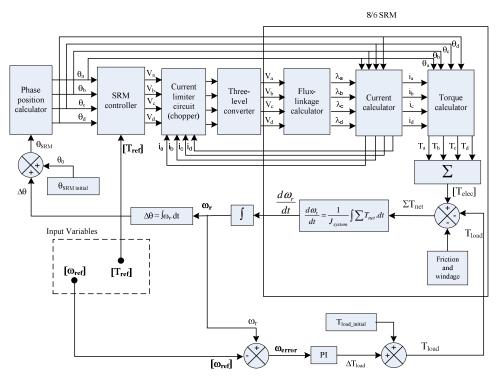


Figure 26 Simulator block diagram

#### 2.8. Angle Definitions

In this study, the mechanical zero position of the rotor is chosen as the same with the initial point of the positive torque region of phase A. The position encoder reset signal which is produced for once in each revolution, is manually adjusted such that the incremental encoder counter is reset at the beginning of the positive torque region of phase A. Since this position coincides with the IN position of the phase C, during the encoder adjustment, phase C is excited and the encoder counter is made to be zero by rotating the encoder while the coupling is loose at the motor side. Just at the encoder position where the reset signal is received, the mechanical coupling is fixed. During motor operation, the phase position is read from the encoder and the phase positions are calculated according to this reference point. In this section, the relation between the mechanical rotor and the electrical phase position will be defined as well as the p.u. angle.

#### **2.8.1.** Electrical Position

In SRM drives, electrical phase position is more convenient than the mechanical rotor position. No matter the position is given in radians or degrees, the relation between the "mechanical rotor position" and the "phase position" is linear and given as follows:

$$\theta_{\text{phase electrical}} = N_r \ x \ \theta_{\text{rotor mechanical}} \tag{28}$$

where *Nr* is the number of rotor poles. "Phase position" will be used instead of "electrical phase position" for the sake of simplicity.

$$\theta_{phase} = \theta_{phase \; electrical} \tag{29}$$

#### 2.8.2. Per Unit Angle

To avoid any misunderstanding while making some definitions about the SRM position, it is always preferable to use dimensionless "*p.u. electrical*" values instead of using the values with units. In an SRM drive, " $\pi$ " or "180<sup>0</sup>" can be used as the p.u. base instead of the full static torque curve period,  $2\pi$  (Figure 27).

Using pu electrical angle instead of electrical degree is more convenient for the generality of relations. For this reason, the simulation results will be given in terms of pu electrical angle. Assuming that the electrical position is given in degrees, the length of the positive torque region is used as the base of the p.u. system:

$$\theta_{p.u.} = \frac{\theta_{elec}}{180} \tag{30}$$

If the electrical position is given in radians, the transformation should be as follows:

$$\boldsymbol{\theta}_{p.u.} = \frac{\boldsymbol{\theta}_{elec}}{\boldsymbol{\pi}} \tag{31}$$

### 2.8.3. Advance Angle

Although the static torque curve begins at "0" electrical degrees, it is more convenient to take "45" electrical degrees as the "zero advance angle" point since the crossover point of the successive phase torque levels are assumed to be at this point for a four phase SRM (Figure 28). The left side of this boundary is named as "advance angle region".

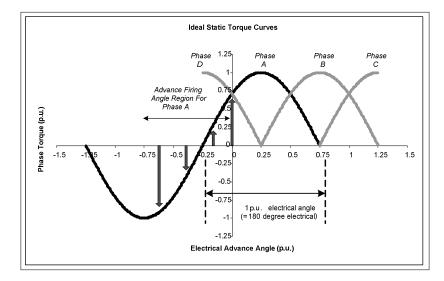


Figure 27 Origin of advance angle and advance angle region as p.u.

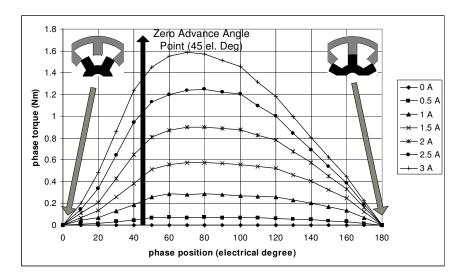


Figure 28 Zero advance angle definition: 45<sup>0</sup> electrical degrees.

# 2.8.4. Conduction Angle

While an SRM operates, one or more phases are energized over an angle which is swept by the rotor pole axis (Figure 30, Figure 29).

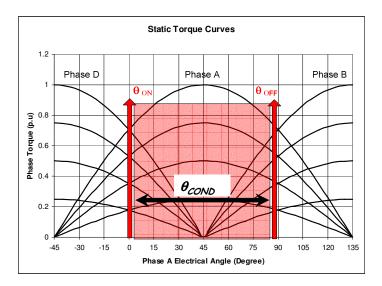


Figure 29 A typical conduction angle: half conduction period (90<sup>0</sup>) starting from "zero advance angle" point. (45<sup>0</sup> electrical degrees)

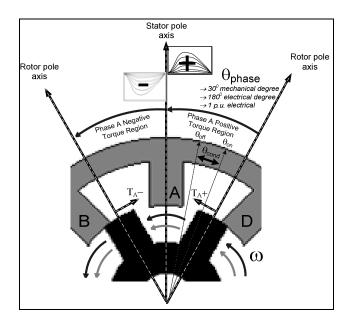


Figure 30 Physical representation of a typical conduction angle in positive torque region.

Typical phase torques and total shaft torque of an SRM at constant phase current with 0 advance and 0.5 p.u. conduction angles are given in Figure 31.

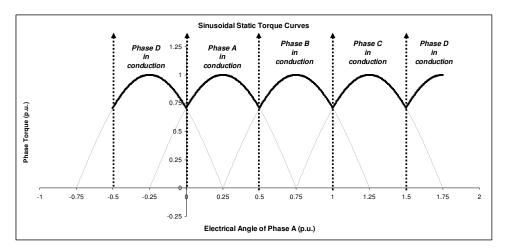


Figure 31 Typical phase torques and total shaft torque of an SRM.

 $(\theta_{adv} = 0, \, \theta_{cond} = 0.5 \text{ p.u.})$ 

## 2.9. Verification of the SRM Simulator Torque Predictions

The verification of the developed simulator is done by experiments on the test motor. For 0.5 and 0.75 p.u. conduction angles, the average torque characteristics are obtained via tests and the results are compared with the simulations.

During the experiments the motor is operated under constant advance and conduction angles with variable mechanical load. In the first part of the experiments, the conduction and advance angles are fixed at 0.5 p.u. and 0 p.u. successively. Under this one-phase-on mode operation, the load torque is adjusted manually from the analog input of the vector controlled induction machine drive. By doing this, the drive speed is changed while the switching angles are kept constant. The average torque and speed is read from Magtrol<sup>®</sup> 6400A torque read-out display. In each step of the experiment, the average torque and the drive speed is manually recorded. The simulations are made under the same conditions. The results of the one-phase-on mode operation is given in Table 1 and Figure 32.

Speed (rpm)	T ave (p.u.) Simulation	T ave (p.u.) Experiment	Error (%)
100	1.26	1.22	3%
740	1.05	1.08	3%
1000	0.89	0.92	3%
1600	0.59	0.62	5%
2020	0.35	0.33	5%
2470	0.24	0.26	6%
3100	0.20	0.22	9%

Table 1 Torque – speed curves obtained from simulations and experiments for 0.5 p.u. conduction and 0 p.u. advance angle.

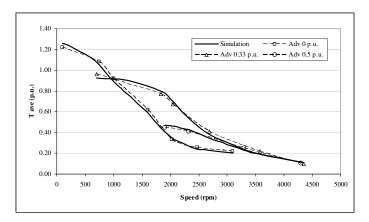


Figure 32 Pull-out torque curves for 0.5 p.u. conduction angle.

After obtaining the results for 0.5 p.u. conduction and 0 advance angles, the experiments are repeated for 0.75 p.u. conduction and 0.22 p.u. advance angles in the same way. First the advance and conduction angles are fixed and then the mechanical load is changed manually to change the drive speed. The average torque and speed again recorded manually from the Magtrol<sup>®</sup> 6400A torque read out. The results are presented in Table 2 and Figure 33.

Speed (rpm)	T ave (p.u.) Simulation	T ave (p.u.) Experiment	Error (%)
350	1.68	1.64	2%
1040	1.54	1.48	4%
1630	1.32	1.25	5%
2100	1.02	0.98	4%
2710	0.59	0.64	8%
3250	0.39	0.41	6%
4450	0.18	0.20	10%

Table 2 Torque – speed curves obtained from simulations and experiments for 0.75 p.u.conduction and 0.22 p.u. advance angle.

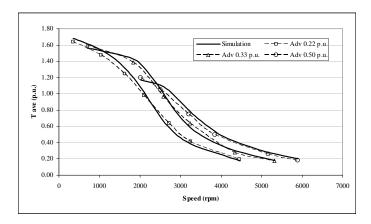


Figure 33 Pull-out torque curves for 0.75 p.u. conduction angle.

It is observed from these tables and average torque curves that the error between the experiments and simulation increases with the speed up to 10 %. This may be because of the unexpected changes in the friction and windage losses in higher speeds. Also the average torque decreases with the speed and the constant noise in measurement may increase the percentage error.

#### 2.10. Verification of the SRM Simulator Current Waveform Predictions

In order to evaluate the reliability of the simulator, instantaneous current waveforms are also considered in different load and speed levels. The test motor is operated in one-phase-on mode and the instantaneous current waveforms are saved to a USB memory stick by a digital oscilloscope. The recorded data is then exported to Matlab<sup>®</sup> workspace. As well as the experiments, the simulations are made under one-phase-on mode operation. The experimentally recorded data and the simulation results of the phase current are shown in Figure 34 - Figure 37.

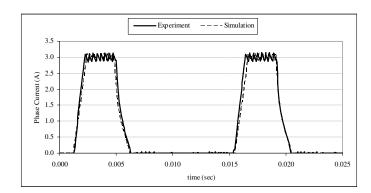


Figure 34 Simulation and experiment results for 1.1 p.u. load torque at 700 rpm.

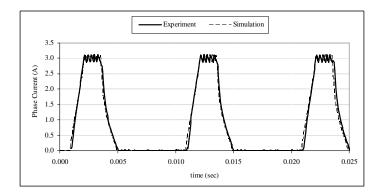


Figure 35 Simulation and experiment results for 0.92 p.u. load torque at 1000 rpm.

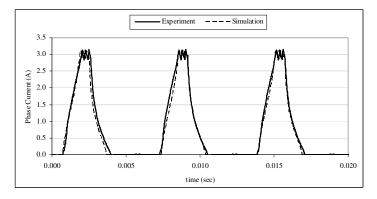


Figure 36 Simulation and experiment results for 0.68 p.u. load torque at 1500 rpm.

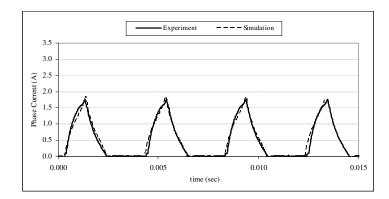


Figure 37 Simulation and experiment results for 0.25 p.u. load torque at 2500 rpm.

It is observed in the verification phase of the SRM simulator that the simulation results are close enough to the experimental results. It should be noted that, since the experiments and simulations are made in one-phase-on mode, the phase current is not affected so much from the mutual couplings between adjacent phases. In fact, in a highly saturated two-phase-on mode operation the phase currents may be distorted because of the common or short flux paths [42]. Also the flux-reversing effect in SRMs having even phase number causes unbalanced phase currents [43]. These current distorting and unbalancing effects can be included in the simulator by adding a suitable mutual flux model but here, the mutual coupling effect is ignored and the phases are assumed to be fully decoupled from each other.

In the next part of the study, the simulator will be the base of the controller design and the SRM performance will be predicted via simulations before the hardware implementation of proposed controller.

## **CHAPTER 3**

## **TORQUE RIPPLE MINIMIZATION OF SRM DRIVES**

In the first chapter of the thesis, it is mentioned that the primary disadvantages of SRMs are the acoustic noise and torque ripple. In the second chapter, regardless of the problem, SRM modeling methods and the drive operation are presented. In this section, a torque ripple minimization method will be proposed by combining the first and the second chapters. In the first section of this chapter, an introduction to the torque ripple problem is presented. Second, the methods given in literature are summarized. Third the non-linear nature of SRM torque is explained briefly. Fourth, a controller is proposed to minimize torque ripple. In the last section the simulation and the experimental results of the designed controller are given.

#### 3.1. Introduction

In DC commutator motors and AC sine-wave motors the average torque is ideally equal to the instantaneous torque at steady state so it is possible to control the instantaneous torque by controlling the average torque. But there are some other motors that do not have constant instantaneous torque such as square-wave fed AC motors, brushless DC motors or SRM. In an SRM drive, instantaneous shaft torque is a function of phase position as well as the phase current. Therefore, the control algorithm must be position dependent, which makes the system time varying. The position dependency of the motor torque makes the control system time-variant, which is not a preferred situation. Speed dependent systems like DC commutator or AC sine-wave motors are not time-varying systems because their mathematical models do not contain time (or position) dependent coefficient matrices at steady state. Besides, by using some mathematical transformations, time-varying systems can be treated as time invariant systems in some special cases.

Furthermore, contrary to the most of the other machines, SRM operates under heavy magnetic saturation to increase the torque production capability. The motor model must include this magnetic non-linearity for a realistic approach. Since the nonlinear time-variant systems are much harder to investigate than the linear timeinvariant systems, SRM modeling and control needs much more effort than any conventional machine.

The total SRM shaft torque is the algebraic sum of the individual phase torques. Although it is easier to design a controller for a decoupled one-phase-on mode drive, limitations of application such as high phase inductance and finite DC link voltage make this type of control impractical. Two-phase-on mode operation may be a better choice to prevent the shaft torque oscillations during commutation, as smoother phase current waveforms are achievable with a finite DC link voltage. This is an important issue both from the point of view of the converter rating and avoiding excessive forces causing audible noise.

In the next section, the major approaches mentioned in literature are presented to understand the state of the art and to have an intuition about the nature of the machine.

#### **3.2. Previous Work**

In literature, many techniques are proposed to control the instantaneous torque of SRM. The main distinguishing feature of these methods is the selected control parameter and those fall into three categories:

- Voltage controllers [8], [13], [14], [19],
- Current controllers [15], [16], [20], [17], [24],
- Flux controllers [18], [21], [22], [23], [25], [26].

In early publications, the phase voltage is generally used as the control parameter. This method has the disadvantage of the requirement of high gain high bandwidth amplifiers. Also complex variable transformations offered in order to calculate the required phase voltage to produce the desired phase torque. Recent publications prefer PWM voltage controllers instead of continuously changing variable voltage sources [9], [11], [11]. In this type of controllers, required phase voltage is calculated by phase torque error and average phase voltage is applied by setting the PWM duty cycle.

The phase current is frequently used as the control parameter but this method requires the pre-calculated phase current data for any torque reference at any speed.

Flux controllers is another alternative to control the motor torque but the required flux observers may suffer from the integration drift problems.

A very early study for instantaneous torque control of SRM is presented by Marija *et al.* [12]. They transformed the time-variant SRM model to a time-invariant system by using Floquet theory, which is a kind of reference frame transformation.

This technique leads to calculate the phase voltages to follow the desired phase torque reference. An important contribution of this study is to define the torque-sharing functions (TSF) to minimize torque ripple. During the past decade, defining the TSFs and making the phases to follow these references by current or voltage control generated many successful control techniques.

Taylor *et al.* designed a control system that performs a state dependent transformation between the phase voltages and the phase torque [13]. The aim of such a linearized control technique is not only to produce the main torque by the strongest phase, but also to get rid of the effects of torque disturbances produced by the incoming or outgoing phases by applying the appropriate phase voltages. During the phase transition, incoming and outgoing phase torques must be eliminated by the strongest phase. This method is basically one-phase-on mode and due to the finite DC link voltage, decoupling of the phases is possible only at low speed. At high-speed operation, outgoing and incoming phase currents cannot change abruptly so the implementation of the method is limited to low speed operation.

Another control method using feedback linearization is proposed in [14]. In this study, Taylor derived current references for the required torque using the measured torque-current-position curves. It is shown that, excellent current tracking is possible by using an amplifier having sufficiently high gain and high bandwidth. In this study, Taylor used a power amplifier with a bandwidth of 1.3 MHz and a gain of 10 V/mA. In order to reduce the order of the system, SRM state equations are separated as electrical and mechanical states. Since the electrical states of the system can be controlled much faster than the mechanical states, the mechanical states are considered as slow, while electrical states are considered as fast. By eliminating the fast electrical states from the system, a reduced order mechanical system is obtained. The decoupled control is applied to this slow system assuming

that the electrical states always obey the fast part of the controller. This is a current controlled one-phase-on mode operation and only the strongest phase produces the required torque. The main contribution of this paper to the literature is meeting the current tracking method in order to control the phase torques. There are mainly two limitations of this approach. First, high gain-high bandwidth amplifier is not practical for industrial applications. Second, in order to decouple the phase torques, only one phase must carry the load torque but this is not possible at high speed region because the phase currents cannot rise or fall in such a short time.

Conventional decoupling and linearizing methods select a commutation angle and assume that commutation occurs instantaneously at just this angle. If this were possible, the torque reference could be a step function so the total torque would be continuous and no torque dips would occur during commutation. To avoid this impossibility, a modified linearization and decoupling method is proposed by Schramm *et al.* [15]. The idea is to change the torque reference as a modest ramp function during commutation instead of step function. It is shown that, to select the beginning and the end points of commutation can minimize the peak and the average current for a desired torque reference. Current-angle curves for different torque levels are calculated from the static torque data. The best commutation width and commutation center points are found by an iterative method. This method needs much off-line calculation before implementation. Even for a specific motor, the commutation width and the commutation center points will not be constant for different torque levels. A lot of commutation data must be found by iterative analysis for all torque levels. Also abrupt changes on torque reference are not realistic so it would be better to select exponentially rising and falling torque references (i.e. torque sharing functions) instead of broken line segments. The contribution of this study is to control the phase currents (instead of voltages) in order to track the torque sharing functions but no method is given to define these torque contours.

A linearization and decoupling technique with a balanced commutator is introduced by Wallace *et al.* [16]. According to the proposed method, the phase with the largest torque-per-ampere ratio produces the most of the required torque. Commutation occurs at critical rotor position where two successive phases produce the same torque at the same current level. At critical rotor positions, each of the energized phases produces half the total desired torque so this currenttracking method is named as a balanced commutator. The main contribution of this paper is to propose a method to calculate the torque sharing functions. In this method each phase torque is controlled individually and total shaft torque is not considered. This method is valid for low speed operation.

Kavanagh, Murphy and Egan proposed a current controller including a self learning technique for the static torque curves [17]. The object of their study is to eliminate the static torque curve measurement stage of the controller design. The method is limited to the low speed operation like the other current controllers.

In [18], Filicori *et al.* derived flux profiles via optimization for constant torque operation. While doing this, they defined two different optimization criteria for two different speed regions: At low-speed, the inverter's current rating and at high speed the inverter voltage rating is chosen as the constraint.

In [19], a Variable Structure System (VSS) control algorithm is designed. The general characteristic of this control is to force the system states to slide on a given surface in the state space. Because of this sliding surface, the control method is also known as Sliding Mode Control (SMC). In this study, a basic type of SMC is applied in order to keep the motor speed constant. Basically, a speed error function taking the rotor acceleration into account is used as the switching function,  $\sigma_{\omega}$ .

$$\sigma_{\omega}\left(\omega, \frac{d\omega}{dt}\right) = \omega_{ref} - \omega_{actual} - \gamma \frac{d\omega}{dt}$$
(32)

By this selection, the phase voltage is calculated as follows

$$V_{phase} = \begin{cases} +V_{DC}, & \sigma_{\omega} < 0\\ -V_{DC}, & \sigma_{\omega} > 0 \end{cases}$$
(33)

By using these two equations, one can find the phase voltage to keep the speed at a desired level. In this study, fixed advance and control angles are used and angle control is not considered. Control verification is made only by simulations and no experimental result is given. In literature, this is the first study on VSS control of SRM. Since the angle control is not included, the method is limited by the base speed. With a finite DC link voltage, to control the motor speed or torque above the base speed is not possible without advance angle control.

In [20], Ehsani and Husain proposed a current controller with TSFs. In their method, each phase of SRM is supposed to follow the torque contours such that the sum of torques produced by each phase is constant and equals the desired torque  $T_{ref}$ . Similar to the method proposed by Marija *et al.* [12], torque-sharing functions are defined for each phase to give a constant shaft torque. The authors preferred sinusoidal contours in order to soften the phase torque reference. As a simplification of the problem, Ehsani and Husain ignored the magnetic saturation and the phase torque is assumed to be a function of phase current. After calculating the required phase currents, a PWM current controller is used to track the current reference. Since the method doesn't include the advance and conduction angles as control parameters, above the base speed the control becomes useless.

Defining arbitrary TSFs to minimize the SRM torque ripple is an optimization problem. Kjaer *et al.* proposed a control method which optimizes two objectives to define optimal TSFs [21]. The primary objective is to minimize the SRM torque ripple while the secondary is the inverter current or inverter voltage rating. In [21], it is shown that satisfying the inverter current or voltage rating constraint depends upon the selection of the commutation angle. If the commutation angle is selected

such that two phases produce equal levels of torque at equal levels of current, then this will be a low-ohmic-loss operation and minimizes the inverter current rating. If the commutation angle is selected such that two phases produce equal levels of torque at equal levels of flux, then this will be a low-voltage operation and considers the inverter voltage rating.

Since to control an SRM becomes harder at higher speeds than low speeds due to the back EMF, Mecrow *et al.* proposed a method to take this effect into account [22]. In this study, the authors proposed flux profiles instead of torque profiles. It is shown that, well-designed flux profiles are able to prevent shaft torque ripple. But similar to the torque profile defining methods, even for a particular SRM, flux profile is not unique to minimize the torque ripple. For a smooth torque, there is infinite number of flux profiles and most of them are not applicable with the available inverters. Driver capabilities must be included in order to eliminate the infeasible solutions. An inverter must deliver the required current at the operating speed. The main disadvantage of the method is the obligation of defining different flux waveforms for each different level of torque and speed. This requires a lot of computational time and high memory capacity. The method seems to be successful up to the base speed but the ambiguity of the commutation interval makes the flux profile selection very difficult.

The methods using predefined TSFs give good results at low speed but they have some disadvantages. Off-line calculated torque references are generally applied to each phase individually. At high speed, to control the phase torques individually may be impossible. In this situation, the motor torque must be considered instead of the phase torque. Russa *et al.* proposed a method to take the total torque into account [23]. Unlike the previous torque sharing methods, their controller considers the total shaft torque instead of the phase torques separately. Precalculated torque sharing functions are not used. Although the methods work at two-phase-on mode, only one phase is controlled by a hysteresis controller while the other one is in either freewheeling or reverse recovery mode. This one-phase controlled but two-phase-on mode reduces the computational load and increases the speed range. One of the overlapped phases is uncontrolled and its torque can be estimated from its position and current. The other overlapped phase is a controlled one and must produce a torque such that the total shaft torque must be equal to the desired level. Because there is no predefined torque or current contours, memory requirement is not as much as the torque sharing function methods.

Most of the methods use off-line data measured from the machine during static conditions. This may bring some problems because the dynamic conditions may cause some drift at motor parameters. Elbuluk *et al.* proposed a fuzzy control method, which is not strictly dependent to the pre-calculated or measured data [24]. This control method can adapt itself to parameter changes. A fuzzy controller uses the implicit relations between the input and output parameters, regardless of their analytical dependence. The controller uses the rotor position and torque error as the input and the phase currents as the output. In this method, Elbuluk *et al.* shared the torque production to the adjacent phases during commutation to obtain a ripple-free operation over a wide speed range. The conduction period is selected in order to increase the torque density. Negative torque production of the outgoing phase is tried to be avoided. This switch off angle is dependent of speed and torque level so an adaptive algorithm must be used to adjust this angle according to the operation conditions. The adaptive and model-free nature of this control with on-line torque estimation is the main contribution to the literature.

To avoid the negative effect of the ignored dynamics of the motor or the parameter drifts Russa *et al.* proposed a self-tuning algorithm that can take these variations into account during operation [25]. The controller uses a nonlinear model of the machine including magnetic saturation. The model parameters are updated online using recursive identification algorithm.

In [26], a variable structure flux-linkage controller is proposed to extend the controller capability above the base speed. But like the other TSF methods, the upper speed is limited. Both [22] and [26] show that defining flux-linkage references to increase the speed range of the ripple-free operation gives similar results as the current controllers.

The findings of the literature review can be summarized as follows:

- Current controllers are cumbersome since they need much off-line calculation and memory size. Besides, they can be utilized up to base speed.
- Flux controllers suffer from the integration drift problems. They are applicable up to base speed if flux references are used.
- Voltage controllers are impractical if smoothly changing variable voltage supply is needed. They can be applicable if a PWM voltage controller is employed,
- Whatever the control parameter is, to obtain a wide speed-range operation, turn on and conduction angles must be taken into account in addition to the phase voltage or current. Since at high speed region current rise time is limited, TSF methods are useless in high speed region.

Regardless of the control method, trying to overcome the torque ripple problem is a kind of objection to the nature of the machine. To change the personality of the machine, of course, will bring some concessions and deteriorations of the general machine performance. This aggravation may arise as worsening the drive efficiency, decreasing the speed range of the control or having a lower average torque than the motor capacity. But a careful investigation of the machine characteristics may reduce the amount of concession. The first stage of the controller design is the selection of the control parameters. After defining the control parameters, any control method can be used for implementation.

In literature, improving the magnetic design of the motor to reduce the torque ripple is also employed [27] but this approach is beyond the scope of this study so we will try to design a controller without offering any change on the magnetic circuit.

## 3.3. A Sliding Mode Controller to Minimize SRM Torque Ripple

Torque ripple is not a desired thing for a smooth and comfortable operation of any rotational mechanical load. It causes knocking and vibration on the motor shaft as well as the coupled load, which is not good for any industrial or domestic application. As mentioned before, total shaft torque of SRM is composed of the sum of the individual phase torques of the motor and this total torque tends to be wavy. If the individual phase torques is designed such that no torque spikes or dips occur on the motor shaft, then the load will not sense anything about what is happening inside the motor. To obtain a seamless torque, phase torques must contribute to each other during the phase transition.

#### **3.3.1.** Controller Design

In the approach here, the desired shaft torque is produced by two phases. The contribution of each phase to the total torque is designed such that the sum of the phase torques must be equal to the desired torque reference  $T_{ref}$ , at any rotor position. For an *m* phase SRM, in order to keep the total torque constant, arbitrary contour function  $T_{ref, i}(\theta_i)$  is defined as follows:

$$T_{ref} = \sum_{j=1}^{m} T_{ref,j} \left( \theta_j \right)$$
(34)

In this study,  $T_{ref, j}(\theta_j)$  is chosen as a Sigmoid (Figure 38). These phase torque reference may be called as 'Torque Sharing Function'. This function must be realistic so that the actual phase torque must be able to follow the contour defined by the torque sharing functions with a finite DC link voltage. Note that, highly inductive nature of SRM impedes the abrupt changes in phase current so the defined torque sharing function must require a moderate rate of change of current. Smoothly changing sigmoid torque reference seems to be traceable with a finite DC link voltage.

After defining the torque sharing function, for a given  $T_{ref}$ , the torque error of the active j<sup>th</sup> phase is calculated as follows;

$$\sigma_{j}(\theta_{j},i_{j}) = T_{j}(\theta_{j},i_{j}) - T_{ref,j}(\theta_{j})$$
(35)

Then a control strategy is used to minimize the individual phase torque error.

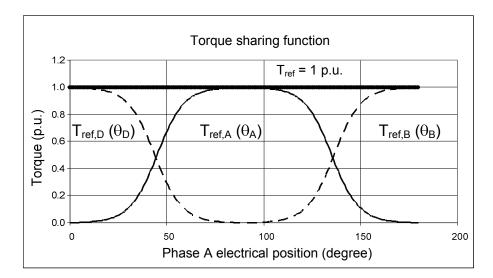


Figure 38 SRM reference torque and sigmoid phase torque references

#### **3.3.2.** Controller Implementation

The basic idea of the sliding mode control is to define a relationship with the switching function with the state equations. In this section, first SRM state equations will be re-organized. Second, the switching function will be taken into account and last, the control voltage equation will be derived.

## 3.3.3. SRM Model

In Chapter 2 SRM state equations are obtained as the phase flux-linkage is a state variable. For a sliding mode controller for instantaneous torque control, the torque error should be related with the state equations. In order to reveal the relation between the switching function and the state equations, the current state equations must be re-organized.

$$\pm V_{DC} = i_{phase} \cdot R_{phase}$$

$$+ \left( \frac{\partial \lambda_{phase}(\theta_{phase}, i_{phase})}{\partial \theta} \cdot \frac{d\theta}{dt} \right) + \left( \frac{\partial \lambda_{phase}(\theta_{phase}, i_{phase})}{\partial i} \cdot \frac{di_{phase}}{dt} \right)$$

$$\frac{di_{phase}}{dt} = \frac{1}{\left( \frac{\lambda_{phase}(\theta_{phase}, i_{phase})}{i_{phase}} \right)}$$

$$\cdot \left( \pm V_{DC} - i_{phase} \cdot R_{phase} - \left( \frac{d\lambda_{phase}(\theta_{phase}, i_{phase})}{d\theta_{mech}} \cdot \frac{d\theta_{mech}}{dt} \right) \right)$$
(36)
(37)

Note that  $\theta_{phase}$  is the mechanical phase angle and its rate of change is equal to mechanical rotor speed:

$$\frac{d\theta_{mech}}{dt} = \omega_{mech} \tag{38}$$

Note that the relation between the mechanical and electrical angle is a function of rotor pole number and given by:

$$\boldsymbol{\theta}_{elec} = N_r.\boldsymbol{\theta}_{mech} \tag{39}$$

Remembering that Nr stands for the rotor pole number, this equation yields

$$\frac{d\theta_{mech}}{dt} = \frac{1}{N_r} \cdot \frac{d\theta_{mech}}{dt}$$
(40)

$$\boldsymbol{\omega}_{mech} = \frac{1}{N_r} \cdot \boldsymbol{\omega}_{elec} \tag{41}$$

The derivative of the flux-linkage with respect to the phase current is defined as the incremental inductance and numerically obtained from the measured data.

$$l_{phase}\left(\theta_{phase}, i_{phase}\right) = \left(\frac{\partial \lambda_{phase}(\theta_{phase}, i_{phase})}{\partial i_{phase}}\right)$$
(42)

So (37) can be written as follows:

$$\frac{di_{phase}}{dt} = \frac{1}{l_{phase} \left(\theta_{phase}, i_{phase}\right)} \\
\cdot \left(\pm V_{DC} - i_{phase} \cdot R_{phase} - \omega_{mech} \cdot \left(\frac{d\lambda_{phase} (\theta_{phase}, i_{phase})}{d\theta_{mech}}\right)\right)$$
(43)

(43) is the state equation of the phase current and will be used at the design stage of the controller. Note that, if the phase voltage is chosen as the control variable, DC link voltage is no more used directly. Instead, a duty cycle controlled variable phase voltage is applied to the motor phase. So there must be little modification in (43) as follows:

$$\frac{di_{phase}}{dt} = \frac{1}{l_{phase} \left(\theta_{phase}, i_{phase}\right)} \\
\cdot \left( \pm V_{phase} - i_{phase} \cdot R_{phase} - \omega_{mech} \cdot \left(\frac{d\lambda_{phase} (\theta_{phase}, i_{phase})}{d\theta_{mech}}\right) \right)$$
(44)

Any controller to be designed must determine the phase voltage in order to have the motor phase produce the required torque.

$$V_{DC} \rightarrow V_{phase} \rightarrow V_j, \quad j = 1, 2, K m$$
 (45)

Here m is the total phase number and  $V_j$  is the phase voltage applied to the j<sup>th</sup> phase. Hence the state equations of an *m* phase SRM are given as follows [3]:

$$\frac{d\theta_{mech}}{dt} = \omega_{mech},$$

$$\frac{d\omega_{mech}}{dt} = \frac{1}{J} \cdot \left( \left( \sum_{j=1}^{m} T_j \left( \theta_j, i_j \right) \right) - T_{load} \left( \theta_{load}, \omega_{load, mech} \right) \right)$$

$$\frac{di_j}{dt} = \frac{1}{l_j \left( \theta_j, i_j \right)} \left( V_j - R_j \cdot i_j - \omega_{mech} \cdot \frac{\partial \lambda_j \left( \theta_{j, mech}, i_j \right)}{\partial \theta_{j, mech}} \right), \quad j = 1, 2, ...m$$
(46)

where  $l_i(\theta_i, i_i)$  is the incremental inductance and given by

$$l_{j}\left(\boldsymbol{\theta}_{j}, i_{j}\right) = \frac{\partial \lambda_{j}\left(\boldsymbol{\theta}_{j}, i_{j}\right)}{\partial \boldsymbol{\theta}_{j}} \tag{47}$$

Here the following terms are calculated from the measured data by using numerical differentiation techniques.

$$\frac{\partial \lambda_j \left( \theta_j, i_j \right)}{\partial i_j}, \quad \frac{\partial \lambda_j \left( \theta_{j, mech}, i_j \right)}{\partial \theta_{j, mech}} \tag{48}$$

## 3.3.4. Sliding Mode Control (SMC)

SMC forces the system states to slide on a desired surface in the state space. This surface is called as the *sliding surface*. If the states slide on the desired surface that means that the system is under control. To keep the system in the sliding regime, a proper equation must be defined for the sliding surface as a function of the system states,  $\sigma(x)=0$ . If the numerical value of  $\sigma(x)$  is equal to zero, than the system is on the sliding surface, otherwise, not. The numerical value of  $\sigma(x)$  is calculated by entering the actual values of the states. When  $\sigma(x)$  is greater than zero, this means that a control signal must be applied to decrease the value of  $\sigma(x)$ . The opposite occurs when  $\sigma(x)$  is less than zero. This is a kind of closed-loop state feedback system to control the value of the switching function  $\sigma(x)$  [19].

If the value of  $\sigma(x)$  is different from zero, the variation in the SMC brings it back to zero. The existence condition of the sliding regime is a

$$\frac{1}{2}\frac{d}{dt}\left\|\boldsymbol{\sigma}\begin{pmatrix}\mathbf{r}\\\boldsymbol{x}\end{pmatrix}\right\|^2 < 0 \tag{49}$$

Remember that the norm function is defined as follows:

$$\left\|\boldsymbol{\sigma}\begin{pmatrix}\mathbf{r}\\\boldsymbol{x}\end{pmatrix}\right\| = \sqrt{\boldsymbol{\sigma}^2\left(x_1\right) + \boldsymbol{\sigma}^2\left(x_2\right) + \mathbf{K} + \boldsymbol{\sigma}^2\left(x_n\right)}$$
(50)

Taking the derivative of (49) gives:

$$\left\|\sigma\!\left(x\right)\right\| \cdot \frac{d\left\|\sigma\!\left(x\right)\right\|}{dt} < 0 \tag{51}$$

This inequality is transformed to equality if the right hand side is always negative.

$$\left\|\boldsymbol{\sigma}\begin{pmatrix}\mathbf{r}\\\boldsymbol{x}\end{pmatrix}\right\| \cdot \frac{d\left\|\boldsymbol{\sigma}\begin{pmatrix}\mathbf{r}\\\boldsymbol{x}\end{pmatrix}\right\|}{dt} = -\left\|f\left(\boldsymbol{\sigma}\begin{pmatrix}\mathbf{r}\\\boldsymbol{x}\end{pmatrix}\right)\right\|$$
(52)

For the sake of simplicity, following expression is obtained:

$$\| \overset{\mathbf{u}}{\boldsymbol{\sigma}} \| \cdot \| \overset{\mathbf{u}}{\boldsymbol{\sigma}} \| = - \| f \begin{pmatrix} \mathbf{u} \\ \boldsymbol{\sigma} \end{pmatrix} \|$$
<sup>(53)</sup>

To have a more flexible control system, a coefficient ( $\alpha$ ) may be added to (53).

$$\left\| \stackrel{\mathbf{u}}{\sigma} \right\| \cdot \left\| \stackrel{\mathbf{u}}{\sigma} \right\| = - \left\| \alpha \cdot f\left( \stackrel{\mathbf{u}}{\sigma} \right) \right\|$$
<sup>(54)</sup>

Now the question is what should be  $f(\sigma)$  in order to have a smoothly changing sliding surface.  $f(\sigma)$  can be called as *Sliding Mode Function* (SMF) and defines the rate of change of error.

$$f\left( \stackrel{\mathbf{u}}{\sigma} \right)$$
: Sliding mode function

Different alternatives for SMF is shown in (55). Note that,  $\alpha$  is a scalar parameter which can be used for accounting the relationship between the system parameters and the rate of change of error. Figure 39 is a visual interpretation of (53).

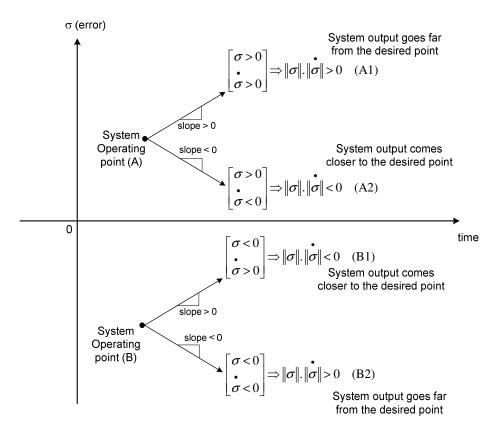


Figure 39 Visual interpretation of sliding mode equations

It is deduced from Figure 39 that (A2) and (B3) conditions are good for the system stability. Actually, (53) forces the system to be in these modes of operation. The selection of the sliding mode function changes only the slope of the error. In (55), some alternatives are given for this selection.

$$\|\boldsymbol{\sigma}\| = \begin{cases} -\|\boldsymbol{\alpha}.sign(\boldsymbol{\sigma})\|, & f(\boldsymbol{\sigma}) = \boldsymbol{\alpha}.\boldsymbol{\sigma}.sign(\boldsymbol{\sigma}) \\ -\|\boldsymbol{\alpha}.sat(\boldsymbol{\sigma})\|, & f(\boldsymbol{\sigma}) = \boldsymbol{\alpha}.\boldsymbol{\sigma}.sat(\boldsymbol{\sigma}) \\ -\|\boldsymbol{\alpha}.sigmoid(\boldsymbol{\sigma})\|, & f(\boldsymbol{\sigma}) = \boldsymbol{\alpha}.\boldsymbol{\sigma}.sigmoid(\boldsymbol{\sigma}) \end{cases}$$
(55)

The relations between the switching function and the sliding mode function mentioned in (55) are given in Figure 40, Figure 41 and Figure 42.

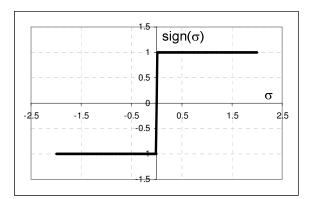


Figure 40 Signum function of  $\sigma$ 

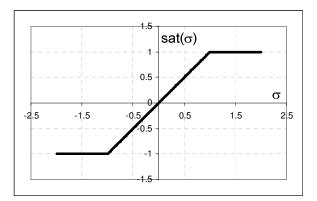


Figure 41 Saturation function of  $\sigma$ 

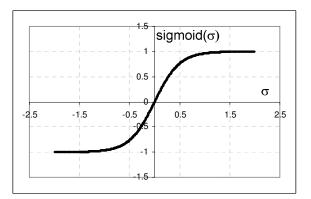


Figure 42 Sigmoid function of  $\sigma$ 

Here, if the first function is selected as the SMF, the rate of change of error is kept constant regardless of the error. If the second and third functions in (55) are used, the rate of change of error becomes dependent of the norm of the error. It is deduced from this functions that selection of saturation or sigmoid functions makes the rate of change of error smoother. This may improve the controller performance since this approaches make the rate of change smaller near the sliding surface to prevent the chattering problem.

### 3.3.5. SMC Design

The aim of a sliding mode SRM torque controller is to keep the shaft torque at a constant reference value. To set the phase torque at the reference value, we need to develop a control signal to minimize the torque error. Torque error is the difference between the total shaft torque and the torque reference. This error value can be considered as a switching function. This *switching function* is defined as follows:

$$\sigma_{j}(\theta_{j}, i_{j}) = \left(T_{e}(\theta_{j}, i_{j}) - T_{ref, j}(\theta_{j})\right)$$
(56)

The existence condition of the sliding regime is

$$\frac{1}{2}\frac{d}{dt}\left\|T_{e}\left(\theta_{j},i_{j}\right)-T_{ref,j}\left(\theta_{j}\right)\right\|^{2}<0$$
(57)

This inequality is transformed to equality by setting the right hand side to a negative value as mentioned in (52).

$$\frac{1}{2}\frac{d}{dt}\left\|T_{e}\left(\theta_{j},i_{j}\right)-T_{ref,j}\left(\theta_{j}\right)\right\|^{2}=-\left\|\alpha.f\left(T_{e}\left(\theta_{j},i_{j}\right)-T_{ref,j}\left(\theta_{j}\right)\right)\right\|$$
(58)

$$\begin{aligned} \left\| T_{e}(\theta_{j},i_{j}) - T_{ref,j}(\theta_{j}) \right\| \cdot \left( \frac{d}{dt} \left\| T_{e}(\theta_{j},i_{j}) - T_{ref,j}(\theta_{j}) \right\| \right) \\ &= - \left\| \alpha.f(T_{e}(\theta_{j},i_{j}) - T_{ref,j}(\theta_{j})) \right\| \end{aligned}$$
(59)

Remember that for a scalar variable, the norm function is equal to absolute value

$$\|\sigma\| = |\sigma| \tag{60}$$

Note the basic properties of the absolute function

$$|\sigma| = \sigma.sign(\sigma) \tag{61}$$

The derivative of the absolute value of a function is given by:

.

$$|\sigma| = \sigma.sign(\sigma)$$
<sup>(62)</sup>

By using these last two relations,

$$\|\boldsymbol{\sigma}\| \cdot \|\boldsymbol{\sigma}\| = \boldsymbol{\sigma}.sign(\boldsymbol{\sigma}).\boldsymbol{\sigma}.sign(\boldsymbol{\sigma})$$
<sup>(63)</sup>

$$\|\boldsymbol{\sigma}\| \cdot \|\boldsymbol{\sigma}\| = \boldsymbol{\sigma} \cdot \boldsymbol{\sigma} \cdot sign(\boldsymbol{\sigma}) \cdot sign(\boldsymbol{\sigma})$$
<sup>(64)</sup>

$$sign^{2}(\sigma) = 1$$

$$\|\sigma\| \cdot \|\sigma\| = \sigma \cdot \sigma$$
(65)

(59) can be simplified by using (65) as follows:

$$\left( T_e \left( \theta_j, i_j \right) - T_{ref, j} \left( \theta_j \right) \right) \cdot \left[ \frac{d}{dt} \left( T_e \left( \theta_j, i_j \right) - T_{ref, j} \left( \theta_j \right) \right) \right]$$

$$= - \left| \alpha \cdot f \left( T_e \left( \theta_j, i_j \right) - T_{ref, j} \left( \theta_j \right) \right) \right|$$

$$(66)$$

$$T_e = T_e\left(\theta_j, i_j\right) \tag{67}$$

$$T_{ref} = T_{ref} \left( \theta_j \right) \tag{68}$$

$$\left(\frac{d}{dt}T_e(\theta_j, i_j)\right) = \left(\frac{\partial T_e(\theta_j, i_j)}{\partial \theta_j}\frac{d\theta_j}{dt}\right) + \left(\frac{\partial T_e(\theta_j, i_j)}{\partial i_j}\frac{di_j}{dt}\right)$$
(69)

$$\left(\frac{d}{dt}T_{ref,j}\left(\theta_{j}\right)\right) = \left(\frac{\partial T_{ref,j}\left(\theta_{j}\right)}{\partial\theta_{j}} \cdot \frac{d\theta_{j}}{dt}\right)$$
(70)

If the phase angle is taken in mechanical instead of electrical position, rotational speed can be used as the derivative of  $\theta_i$ 

$$\frac{d\theta_{j,mech}}{dt} = \omega_{mech} \tag{71}$$

Remember that

$$\boldsymbol{\theta}_{elec} = N_r \boldsymbol{.} \boldsymbol{\theta}_{mech} \tag{72}$$

$$\boldsymbol{\omega}_{elec} = N_r.\boldsymbol{\omega}_{mech} \tag{73}$$

Substitution of (69) and (70) into (66) yields;

$$\left(T_{e}\left(\theta_{j},i_{j}\right)-T_{ref,j}\left(\theta_{j}\right)\right)$$

$$\left[\left(\omega_{mech}\cdot\frac{\partial T_{e}(\theta_{j,mech},i_{j})}{\partial\theta_{j,mech}}\right)+\left(\frac{\partial T_{e}(\theta_{j},i_{j})}{\partial i_{j}}\cdot\frac{di_{j}}{dt}\right)-\left(\omega_{mech}\cdot\frac{\partial T_{ref,j}\left(\theta_{j,mech}\right)}{\partial\theta_{j,mech}}\right)\right]$$

$$=-\left|\alpha.f\left(T_{e}\left(\theta_{j},i_{j}\right)-T_{ref,j}\left(\theta_{j}\right)\right)\right|$$

$$(74)$$

In (74), the state equation of the phase current is obtained. Substituting (46) into this equation gives

$$\left(T_{e}\left(\theta_{j},i_{j}\right)-T_{ref,j}\left(\theta_{j}\right)\right)$$

$$\left[\left(\omega_{mech}\cdot\frac{\partial T_{e}\left(\theta_{j,mech},i_{j}\right)}{\partial \theta_{j,mech}}\right) + \left(\frac{\partial T_{e}\left(\theta_{j},i_{j}\right)}{\partial i_{j}}\cdot\left(\frac{1}{l_{j}\left(\theta_{j},i_{j}\right)}\left(V_{j}-R_{j}i_{j}-\frac{\partial\lambda_{j}\left(\theta_{j,mech},i_{j}\right)}{\partial\theta_{j,mech}}.\omega_{mech}\right)\right)\right)\right) \quad (75)$$

$$-\left(\omega_{mech}\cdot\frac{\partial T_{ref,j}\left(\theta_{j,mech}\right)}{\partial\theta_{j,mech}}\right)\right]$$

$$=-\left|\alpha.f\left(T_{e}\left(\theta_{j},i_{j}\right)-T_{ref,j}\left(\theta_{j}\right)\right)\right|$$

Where the following equations are calculated numerically by using the measured data.

$$\frac{\partial T_e\left(\theta_{j,mech}, i_j\right)}{\partial \theta_{j,mech}}, \frac{\partial T_e\left(\theta_j, i_j\right)}{\partial i_j}, \frac{\partial \lambda_j\left(\theta_j, i_j\right)}{\partial \theta_{j,mech}}, \frac{\partial \lambda_j\left(\theta_j, i_j\right)}{\partial i_j}$$
(76)

Control voltage  $V_j$  can be solved as a function of the state variables from this equation as follows

$$V_{j}(\theta_{j},i_{j},\omega_{mech}) = \left[ \left( \frac{-\left| \alpha f\left(T_{e}(\theta_{j},i_{j}) - T_{nef,j}(\theta_{j})\right)\right|}{\left(T_{e}(\theta_{j},i_{j}) - T_{nef,j}(\theta_{j})\right)} - \omega_{mech} \cdot \frac{\partial T_{e}(\theta_{j,mech},i_{j})}{\partial \theta_{j,mech}} + \omega_{mech} \cdot \frac{\partial T_{nef,j}(\theta_{j,mech})}{\partial \theta_{j,mech}} \right)$$

$$\cdot \frac{1}{\frac{\partial T_{e}(\theta_{j},i_{j})}{\partial i_{j}}} \cdot \frac{1}{l_{j}(\theta_{j},i_{j})} \right] + \left( \omega_{mech} \cdot \frac{\partial \lambda_{j}(\theta_{j,mech},i_{j})}{\partial \theta_{j,mech}} \right) + \left(R_{j}i_{j}\right)$$

$$(77)$$

Substituting (55) into (77) gives

$$V_{j}(\theta_{j}, i_{j}, \omega_{mech}) = \left[ \left( -\left| \alpha sigmoid(T_{e}(\theta_{j}, i_{j}) - T_{ref, j}(\theta_{j})) \right| - \omega_{mech} \cdot \frac{\partial T_{e}(\theta_{j, mech}, i_{j})}{\partial \theta_{j, mech}} + \omega_{mech} \cdot \frac{\partial T_{ref, j}(\theta_{j, mech})}{\partial \theta_{j, mech}} \right) \right]$$

$$\cdot \frac{1}{\frac{\partial T_{e}(\theta_{j}, i_{j})}{\partial i_{j}}} \cdot \frac{1}{l_{j}(\theta_{j}, i_{j})} \right] + \left( \omega_{mech} \cdot \frac{\partial \lambda_{j}(\theta_{j, mech}, i_{j})}{\partial \theta_{j, mech}} \right) + \left( R_{j} i_{j} \right)$$

$$(78)$$

This is the control voltage for SMC to keep the system in the sliding regime. In other words, if this voltage is applied to the phase, the phase torque error will be forced to be zero. Note that, the first term of this equation is the *Sliding Mode Function (SMF)*, which is defined in (55). The controller block diagram is given in Figure 43.

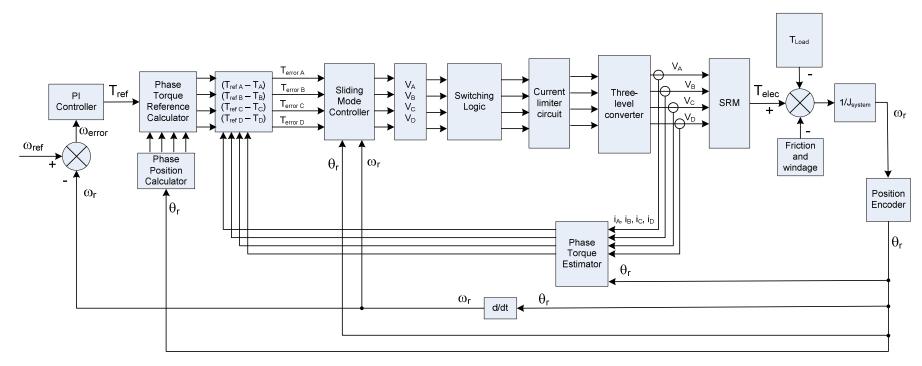


Figure 43 Sliding mode controller block diagram.

#### 3.3.6. Simulation Results

For the simulation of SRM and controller, Matlab Simulink<sup>®</sup> model is used to implement the control algorithm. For the SRM model used in simulations, measured static torque-current-position and flux linkage-current-position curves are used as given in Chapter 2.

An integration step of 1  $\mu$ s is used for the simulations. The control is also applied every 1  $\mu$ s. DC link voltage is assumed to vary continuously between ±300 V. To be able to implement this control, phase currents and the rotor angle information is required. In simulations, phase currents are obtained from the flux-linkageposition-current and the rotor angle is obtained from the integration of the assumed constant speed for the studied case.

The sigmoid function given in (55) and Figure 42 is used as sliding mode function to avoid abrupt changes in the control signal.

The simulation results for this case for a reference torque of 1 Nm at 785 rpm with 1  $\mu$ sec integration step size and a same period of control cycle are given in Figure 44. In Figure 45, the required phase voltage is given for a smooth torque operation. Figure 46 displays the phase currents of the motor during the control process. It can be observed that the top of the current waveforms is virtually flat. Therefore, the power supply rating is not required to be unnecessarily high. Furthermore, the dynamic response of the power supply does not need to be fast. Note that, these smooth current shapes also assure that the radial forces on the rotor does not have pulsed shapes. Therefore it is possible to conclude that any acoustic noise due to such forces is also eliminated for all practical purposes.

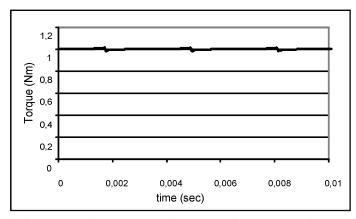


Figure 44 Simulation results for a total shaft torque of 1 Nm at 785 rpm. (Simulation step time 1  $\mu sec)$ 

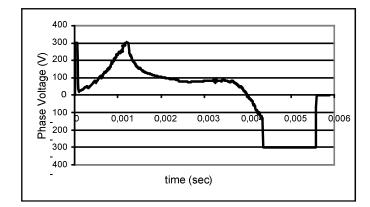


Figure 45: Phase voltage waveform for the simulation at 1 Nm 785 rpm using sigmoid function

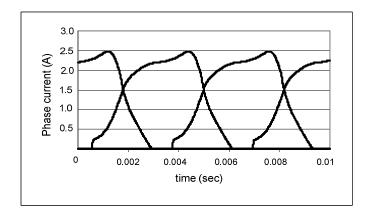


Figure 46 Simulated phase currents for 1 Nm at 785 rpm. (Simulation step time: 1 µsec)

#### 3.3.7. More realistic simulation results

Once the choice of the control structure is decided, a more realistic simulation of the controller and the motor is made. In this case, the DC link voltage is taken to be constant at 300 V, the integration step is taken as 1  $\mu$ s, as before. The calculated reference signal is assumed to be produced by a 20 kHz PWM modulator acting on the dc link voltage. It is assumed that the time the microprocessor would take to do the required calculations shall be in the order of 200  $\mu$ s. The phase current values are again solved from related equations. The position information is calculated from the constant operating speed. The simulator acquires current and position data to calculate the next reference voltage. However, this reference level is fed to the controller after 200  $\mu$ s. Until this period is completed, the simulation is continued with the previous reference voltage level. The choice of  $\alpha$  depends on the system dynamics and the controlled parameters, so during simulations some trial errors must be made to determine the range of this constant.

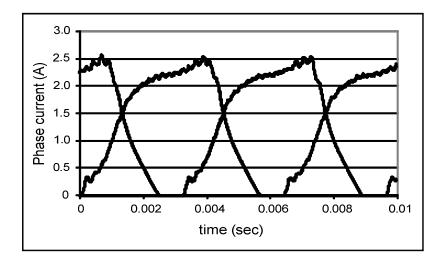


Figure 47 Phase currents with 20 kHz PWM for 1 Nm at 785 rpm

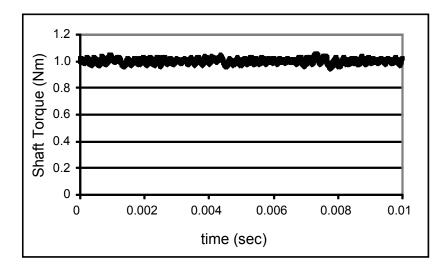


Figure 48 Total shaft torque with 20 kHz PWM for 1 Nm at 785 rpm

The results of this type of simulation are given in Figure 47 and Figure 48 for 1 Nm at 785 rpm. It can be observed from Figure 48 that, the shaft torque fluctuation is larger (about 4%) in this case as compared to the result in Figure 44. This is an expected finding since there is now a PWM controlled signal is applied to phase instead of a smoothly changing unrealistic voltage supply. Note that, in this case the calculated PWM signal is not applied to the phase immediately as before. Instead, a control cycle delay occurs since the defined control can be applied just in the next cycle. This is more realistic and this time there is a delay on the control action. The phase current waveforms for the conditions mentioned above are given in Figure 47. The current magnitude and shape is quite similar to the results found in earlier simulations. However an increase in torque ripple is obvious in this case from comparison of Figure 44 and Figure 48.

## 3.3.8. Hardware Implementation

With this understanding of the problem the developed control scheme is implemented on a dSPACE DS1104 controller board. The phase voltage control is

achieved by the same processor, controlling 4 PWM outputs at 20 kHz with the reference voltages provided by the control strategy.

The switching required by the controller is used to drive the transistors of an SR motor driver. Hence the phase voltages could be set as computed by the controller. The DC link voltage of the SRM drive is obtained by rectifying a three-phase 50 Hz AC supply and it is set to 300 V. The driver is used to drive a 150 V, four-phase, 8/6 SRM with a rated current of 3 A.

The controller algorithm is developed on Matlab Simulink and then implemented on a dSPACE DS1104 controller board. For the controller implementation, measured *static torque-current-position* and *flux linkage-current-position* curves are used as described in Chapter 2.

The motor is coupled to a vector controlled induction machine, which operates as a controlled mechanical load. A rotating torque transducer is placed in between the two shafts to measure the torque produced by the test motor, as shown in Figure 49.

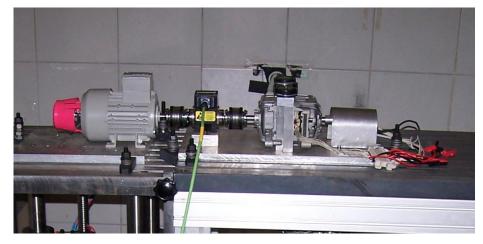


Figure 49 Test setup used for the torque measurements.

#### 3.3.9. Experimental Results

Current, voltage and torque measurements are made at several speeds both in the one phase on mode and with sliding mode control.

Figure 50 displays the recorded current and voltage waveform that appear on one of the phases of the motor, while the motor is producing 0.92 Nm, at a shaft speed of 785 rpm with a 1 Nm reference. The difference between the reference value and the produced torque is due to friction and windage loss of the motor and possibly also due to controller error. The phase voltage is modulated at 20 kHz and the control cycle is 200 µsec just as in the simulations. The measurements are given in Figure 50 may be compared with the simulation result given in Figure 47. When the current waveforms in these figures are compared, it can be observed that the shape of the waveform and its peak value are very similar. It is not possible to compare the measured phase voltage waveform with the simulation result directly, as the measured waveform displays the PWM signal rather that the instantaneous value of the phase voltage is applied can be observed. This comparison indicates that the simulation results are realistic.

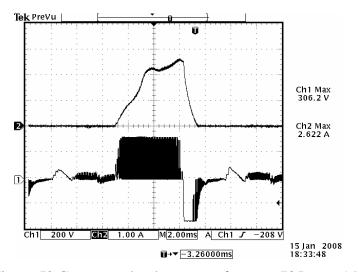


Figure 50 Current and voltage waveforms at 785 rpm, 1 Nm Trace 1: Phase voltage controlled by PWM (200 Volts/div) Trace 2: Phase current (1 A/div)

Figure 51 displays the shaft torque and phase currents of the test motor, while producing 1.22 Nm at 100 rpm. In Figure 52, the motor shaft torque and phase currents while the motor is running at 100 rpm and producing 1.26 Nm are given with a reference torque level of 1.35 Nm.

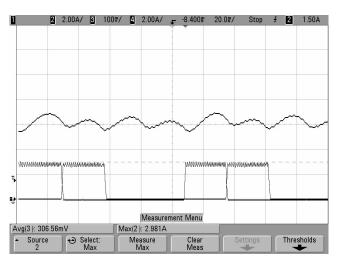


Figure 51 The test motor producing 0.92 Nm, at 100 rpm, without control.

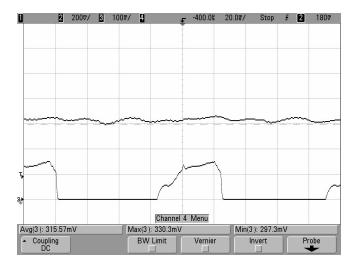


Figure 52 The test motor producing 0.92 Nm, at 100 rpm, under sliding mode control

Inspection of these figures clearly displays how effective the sliding mode control is on smoothing the shaft torque. Note also the reduction in peak phase current in the controlled mode in comparison with the uncontrolled case.

Motor shaft torque is also recorded while the motor is running at 785 rpm and producing 0.92 Nm, with torque reference of 1 Nm. Figure 53 displays the recorded shaft torque and current while no control is applied. Figure 54 displays the same variables under sliding-mode controlled operation. It is again possible to observe that the sliding-mode controlled case needs smaller average phase current to produce the same torque as in the uncontrolled case. However, the torque ripple in this case is smaller in the one phase on mode operation as compared to the torque ripple at 100 rpm. This is an expected result since the low pass filtering effect of the inertia becomes significant at this higher speed. Because of this mechanical filtering, smaller recorded ripple on the shaft torque does not mean that the electrical torque on the SRM shaft has smaller ripple. The mechanical system still experiences the ripple on the electrical torque and this may be a source of vibration. Therefore, a controller minimizing electrical torque ripple is still desirable at higher shaft speeds.

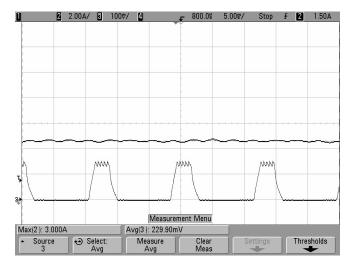


Figure 53 The test motor with one-phase-on mode producing 0.92 Nm, at 785 rpm, without control

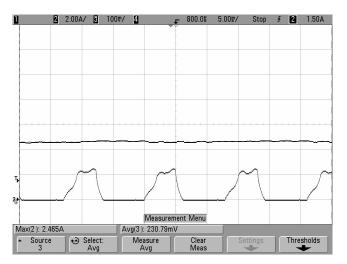


Figure 54 The test motor producing 0.92 Nm, at 785 rpm, under sliding mode control

At this stage, to identify the key factors of the problem, advance angle is taken as - 0.25 p.u., the conduction angle is kept at unity and only the phase voltage is taken as control variable. For a high grade controller, the advance and conduction angles must be taken into account. Note that, up to know, in both controlled and uncontrolled operation, the switching angles are kept constant. In uncontrolled one phase on mode, the motor is operated in one-phase-on mode where the conduction

angle is 0.5 p.u. and the advance angle is 0 p.u. Under sliding mode control, the conduction angle is 1.0 p.u. and the advance angle is -0.25 p.u. If the advance and conduction angles are not included in the controller, the average shaft torque cannot be controlled with the increasing speed. In Figure 55, the uncontrolled SRM torque with the constant switching angles is given.

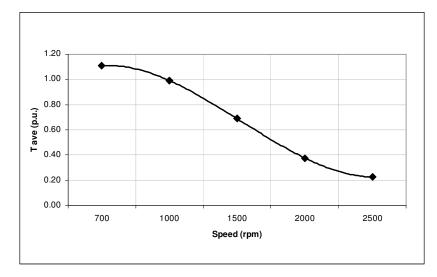


Figure 55 SRM average torque under one phase on mode with 0 p.u. advance and 0.5 p.u. conduction angle (Experiment).

## 3.3.10. Acoustic Noise Measurements

To observe effect of the adopted control strategy on reducing the acoustic noise emitted by the drive; a set of measurements are done in an anechoic chamber. In these measurements the load side is enclosed in a properly padded box so as to reduce the effect of any noise emitted by the load side motor drive.

First to have an idea of the noise level generated by the mechanical system and the load, the load (induction) motor is used to drive the system under no load condition (the load is just the friction and windage of the test system). At 2000

rpm two tests are done without the noise suppression box and with the noise suppression box. The noise level is measured as 61.7dbA and 59.6 dbA respectively for the two cases.

The same experiment is repeated with the test motor (SRM) driving the load at 2000 rpm in the uncontrolled mode. The noise level is measured as 76.4 dbA when the load side noise suppression box removed and 74.8 dbA with the box in place. These tests give an idea of the background noise level and also illustrate the difference between the noise levels of an induction motor drive and an SR motor drive. It must be noted however that the comparison is not totally fair, as the SR motor has no frame.

Further experiments are carried out on the SR motor under load without sliding mode control (1-phase on mode) and with sliding mode control for the same load and speed. Table 3 and Figure 56 summarize the findings. It can be observed that with the sliding mode control, considerable noise reduction is achieved at all speeds. At higher speeds greater reduction in noise level is observable. The reduction in audible noise is grater than 7db at 2000rpm.

Speed (rpm)	Load (p.u.)	Uncontrolled Noise (dBA)	Controlled Noise (dBA)	Amount of Noise Reduction (dBA)
700	1.10	75.13	73.30	1.83
1000	0.92	74.78	73.35	1.43
1500	0.68	81.02	77.26	3.76
2000	0.37	83.88	76.53	7.35
2500	0.25	84.40	78.60	5.80

Table 3 Recorded noise levels of SRM drive at different speeds.

Figure 57 displays the reduction in torque ripple due to sliding mode control implementation. It can be observed that in fact torque ripple reduction is greater at lower speeds than the higher speed end. Furthermore the torque ripple is twice as large for the higher speeds. This is contradictory to the observation above that noise reduction is larger at higher speeds. At this point it is worthwhile to inspect the phase current waveforms at low (1000 rpm or less) and higher speeds (greater than 2000 rpm).

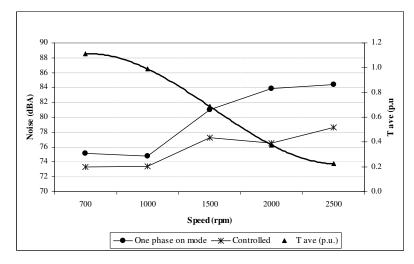


Figure 56 Noise levels under uncontrolled (one phase on) and controlled modes with the corresponding load levels.

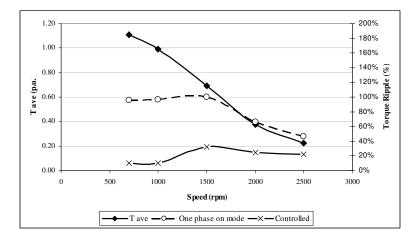


Figure 57 Torque ripple with and without (one phase on mode) sliding mode control

Figure 58 and Figure 59 display the recorded current waveforms in one-phase-on mode and under sliding mode control, during the noise measurements at 1000 rpm and 2000 rpm respectively. These figures illustrate that;

i) The peak value of the phase current is smaller for both control schemes at higher speed,

ii) Under sliding mode control, phase current is smaller than one phase on mode case, both at higher and lower speed cases,

iii) However the ratio of the one-phase on mode current peak to the sliding mode controlled peak current is greater at 2000 rpm (higher speed).

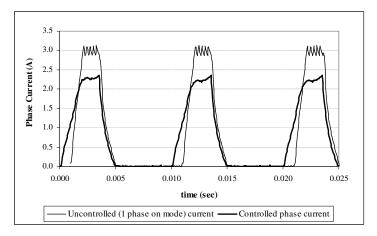


Figure 58 One phase on mode and controlled phase currents for 0.87 Nm at 1000 rpm.

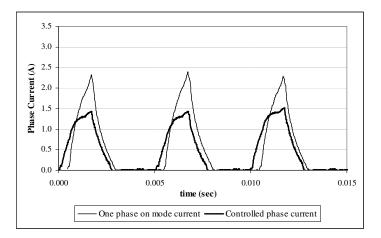


Figure 59 One phase on mode and controlled phase currents for 0.37 Nm at 2000 rpm.

This suggests that the magnitude of the current near the aligned position is also significant in acoustic noise and this may be one of the important factors contributing to larger noise reduction at higher speeds despite the fact that torque ripple is greater than lower speed operation.

Higher phase currents may mean that the normal forces acting on the frame are larger. In other words; although lower noise level is possible, when the SR motor is operated with sliding mode control, it is not clear whether the reduction in the audible noise is due to reduced shaft ripple or reduced normal forces acting on the frame.

From Figure 56 it can be also observed that the shaft torque quickly falls with speed. This points out that a more sophisticated control approach must be sought so that torque is available in a wider speed range.

#### 3.4. Conclusions

In this chapter, it is shown that sliding mode control can be used to obtain smooth electromechanical torque from SR motors, provided that SMC function is well chosen. It is observed that with this type of control, the current waveforms are not fast changing and do not have peaky waveforms, contributing to the reduction of noise. Both the simulations and experiments show that a 4 phase, 150 V SRM shaft torque could be controlled to follow the reference level set. It is also shown that, the torque ripple is much smaller when the control strategy developed here is applied.

In the application here, PWM modulated phase voltages are used for control purpose. Despite this (i.e. the voltages applied are formed of pulses), considerable reduction in audio noise level is perceived. Acoustic noise produced by the SR

drive is measured in an anechoic chamber. It is observed that the acoustic noise of the SR drive is reduced when sliding mode control strategy is utilized. The reduction in noise is about 2 dB at low speeds and is more than 7 dB at higher speeds. When the torque ripple of the SR drive is examined over the speed range, it is observed that torque ripple is larger at higher speeds where larger noise reduction is obtained. When the current waveforms of the drive at different speeds are examined it is observed that at higher speeds the reduction in peak current is greater at higher speeds under sliding mode control as compared to the uncontrolled case. From these observations it may be concluded that the magnitude of the current may be an important factor in reducing acoustic noise and it is not possible to conclude that the noise reduction achieved is solely due to torque ripple reduction.

The only control variable in this application is the phase voltage. As a consequent of this, although torque ripple and acoustic noise are reduced, motor torque quickly falls and a limited speed range is achievable. The control strategy can be further developed to include advance angle control and conduction angle control to extend the speed range and meanwhile operate the motor with reduced acoustic noise and high efficient for a given torque reference.

# **CHAPTER 4**

# EFFECTS OF ADVANCE AND CONDUCTION ANGLES ON SRM CONTROL

In previous chapter, a control algorithm to minimize torque ripple was developed taking the advance and conduction angles constant as 0.25 and 1 p.u. In this approach to minimize torque ripple, In this approach to minimize the torque ripple only the phase voltage is used as the control parameter. Although a good low speed performance is obtained, the operating speed range is limited in this approach. Before designing a more sophisticated SRM controller including the switching angles, the effects of the control parameters must be perceived well enough via simulations. In these simulations, the DC link is taken constant. It is well known that advance and conduction angles are important parameters for widening the operated range of an SRM for fixed DC bus voltage.

In this chapter, the effects of the advance and conduction angles on the average torque and torque ripple will be analyzed via simulations. The purpose is to identify the conditions in which torque ripple can be minimized as well as the efficiency and to observe how the operating speed range can be widened. During simulations, for different levels of conduction angle, turn-on angle will be advanced for observing the average torque and torque ripple variation with respect to advance angle. At the end of the chapter, an algorithm will be proposed for the selection of the appropriate switching angles to produce the load torque with minimum torque ripple. After gathering the required data from the simulations, the

effects of the torque ripple minimization algorithm on acoustic noise will be ascertained by noise measurements in an anechoic room.

# 4.1. Constant Speed Variable Advance and Conduction Angles Simulations

In this stage of the research, a detailed investigation is carried out to understand the effects of the switching angles on SRM torque ripple and torque per ampere while producing the average torque. The simulations are made between 2000 and 12000 rpm. The lower limit of simulations is selected as 2000 rpm to represent the SR drive behavior at low speeds where the power supply is capable of driving the rated current of the motor over the control parameter range. The upper speed is chosen as 12000 rpm where the voltage magnitude of the power supply is no longer enough to drive the requested current level at a given operating condition. For each speed, simulation results are presented at three conduction angles: 0.50, 0.75 and 1.00 p.u. The advance angle is kept as variable during the investigation.

Figure 60 displays the well known general behavior of an SR drive at 2000 and 12000 rpm. From this figure it can be observed that at a given speed there is a value of advance angle at which the average torque can be maximized. However, these curves provide no indication of the torque ripple on the shaft. The variation of the average torque at other speeds (3000 to 6000 rpm) are given in Figure 61 to Figure 64. In this study, the nominal average torque of the test motor is taken as 1.0 Nm which is the base value for the p.u. transformations:

$$T_{ave,base} = 1.0 \ Nm \tag{79}$$

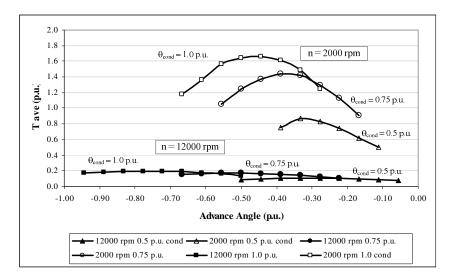


Figure 60 Average torque curves for different conduction angles at 2000 and 12000 rpm. (Uppermost three curves at 2000 rpm, lowermost three curves at 12000 rpm.)

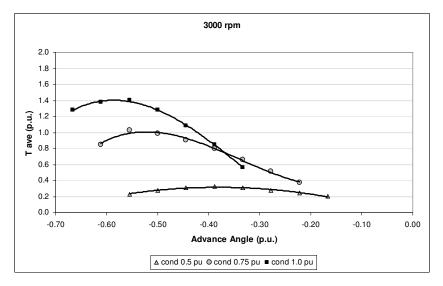


Figure 61 Average torque versus advance angle with different conduction angles at 3000 rpm.

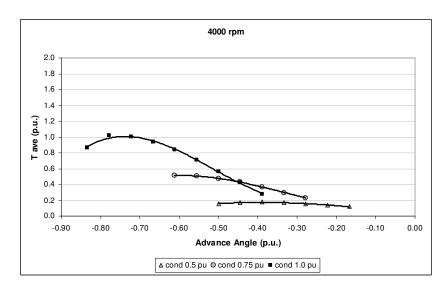


Figure 62 Average torque versus advance angle with different conduction angles at 4000 rpm.

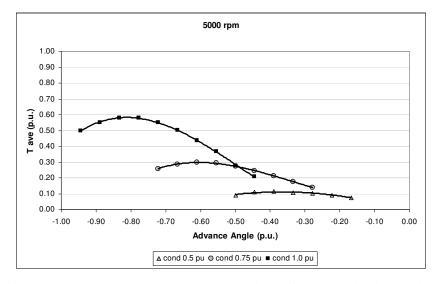


Figure 63 Average torque versus advance angle with different conduction angles at 5000 rpm.

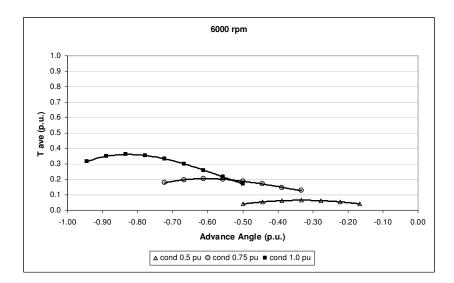


Figure 64 Average torque versus advance angle with different conduction angles at 6000 rpm.

In Figure 65, the average torque and the torque ripple variation is observed at 2000 rpm for 0.5 p.u. conduction angle. It is seen that, the machine torque reaches a maximum level for a specific advance angle value while the torque ripple increases with advancing the turn-on angle. In Figure 66, the variation of the average torque and the torque ripple is given for 0.75 p.u. conduction angle. The average torque variation is similar to the 0.5 p.u. conduction as it has a maximum level. In Figure 67, the results for the unity conduction angle is given. It is observed from these simulations that, for each conduction angle there is a maximum average torque and minimum torque ripple level.

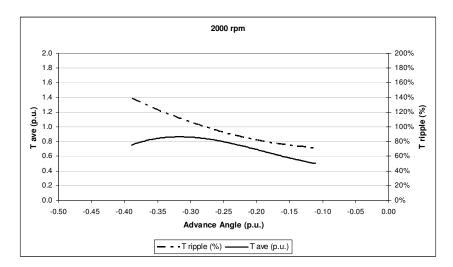


Figure 65 Average torque and torque ripple variation versus advance angle with 0.5 p.u. conduction angle at 2000 rpm.

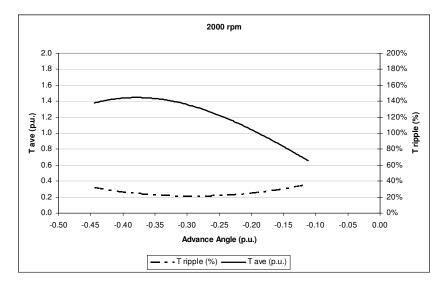


Figure 66 Average torque and torque ripple variation versus advance angle with 0.75 p.u. conduction angle at 2000 rpm.

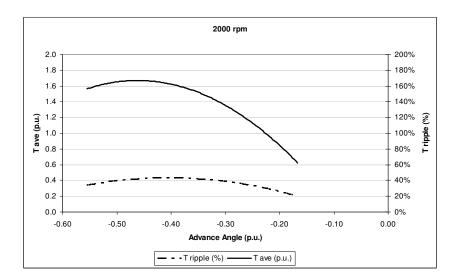


Figure 67 Average torque and torque ripple variation versus advance angle with 1.00 p.u. conduction angle at 2000 rpm.

It is deduced from the simulation results given in Figure 69 to Figure 74 that by using the average torque and torque ripple variation characteristics, the minimum torque ripple point can be obtained for any load torque at a given speed. The minimum torque ripple point determination algorithm is summarized in Figure 68 at 2000 rpm. In this figure, it is seen that there are different conduction and advance angle pairs driving the same load torque at the same speed. As a case study, 0.7 p.u. load torque at 2000 rpm is investigated in Figure 68. Under this loading conditions, the torque ripple varies between 140 % and 35 % for different advance and conduction angles. The motor can produce an average torque of 0.7 p.u. at 2000 rpm at a torque ripple of 140 % if the advance angle is about -0.43 p.u. at 0.50 p.u. conduction. With the same conduction angle the same average torque is produced at -0.22 p.u. advance angle with 85 % torque ripple. If however, the conduction angle is kept at 0.75 p.u. instead of 0.5, the same average torque is produced at -0.15 p.u. advance angle with 35 % torque ripple. By using these characteristics, the controller can determine the most convenient switching angles for the minimum torque ripple operation.

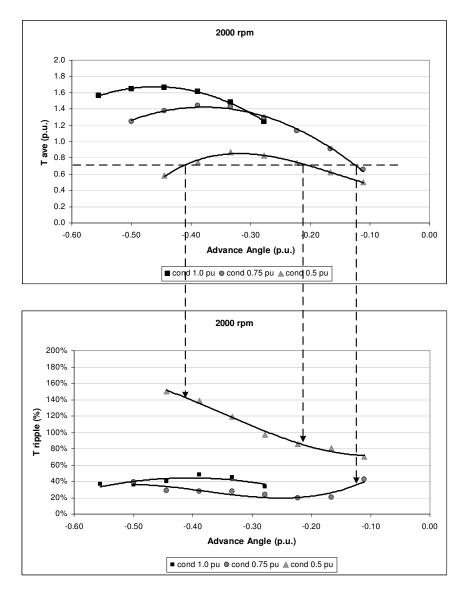


Figure 68 The advance and conduction angle determination algorithm considering minimum torque ripple for 0.7 p.u. load torque at 2000 rpm.

When the results for 12000 rpm are studied it can be observed that the maximum average torque at this speed ( $\approx 0.2$  Nm) may be produced at 85 % torque ripple or at about 20 % torque ripple depending on the choice of the advance angle at unity conduction. It can also be observed that for both speeds, it is possible to obtain the desired shaft torque at low ripple for a range of the advance angle values rather than at a single value. At 2000 rpm, the desired shaft torque can be produced in the

-0.42 to -0.13 p.u. region while at 12000 rpm, the maximum torque can be produced between -0.74 to -0.50 p.u. advance angles.

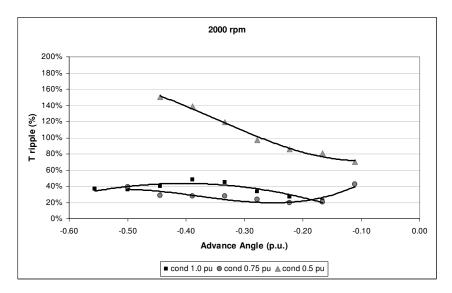


Figure 69 Torque ripple versus advance angle with different conduction angles at 2000 rpm.

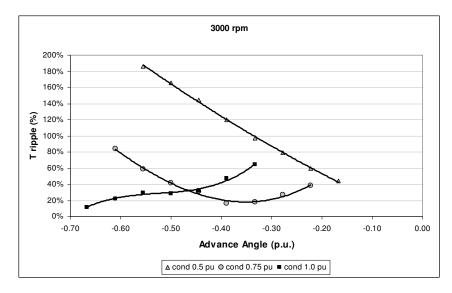


Figure 70 Torque ripple versus advance angle with different conduction angles at 3000 rpm.

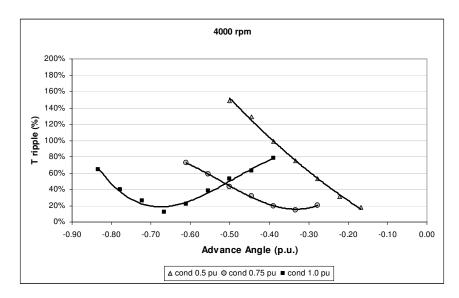


Figure 71 Torque ripple versus advance angle with different conduction angles at 4000 rpm.

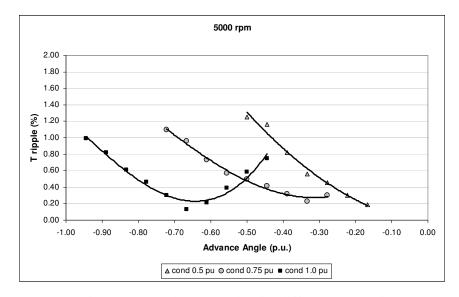


Figure 72 Torque ripple versus advance angle with different conduction angles at 5000 rpm.

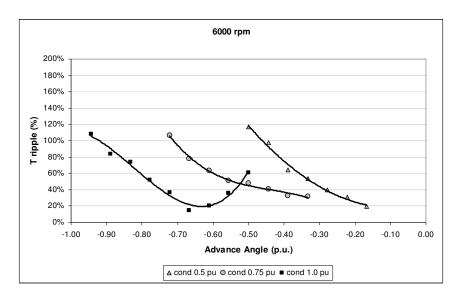


Figure 73 Torque ripple versus advance angle with different conduction angles at 6000 rpm.

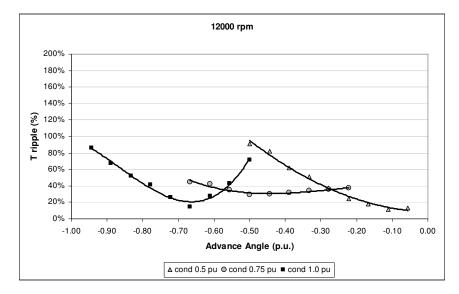


Figure 74 Torque ripple versus advance angle with different conduction angles at 12000 rpm.

The overall operating the motor at the lowest possible torque ripple condition can be traced from Figure 75 to Figure 77.

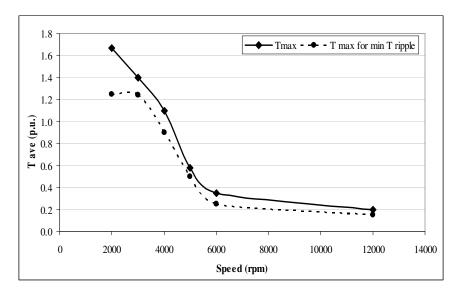


Figure 75 Maximum average torque and the average torque for minimum torque ripple for unity conduction angle.

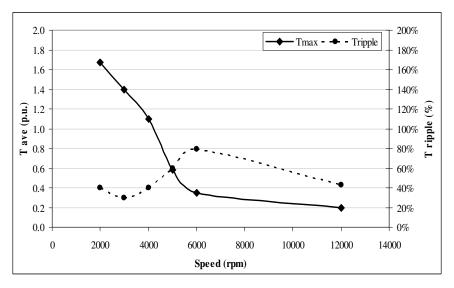


Figure 76 Maximum average torque and corresponding torque ripple for unity conduction angle.

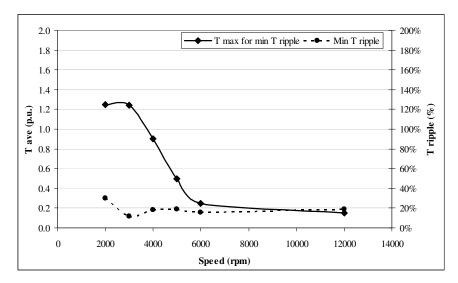


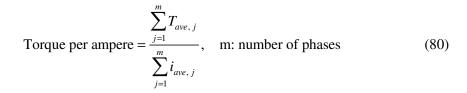
Figure 77 Minimum torque ripple and corresponding average torque for unity conduction angle.

In Figure 75, the maximum average torque and the average torque for the minimum torque ripple are given. As it is seen, the torque ripple can be reduced with the sacrifice of the maximum torque output. The average torque and the torque ripple curves are given in Figure 76 and Figure 77 for the maximum torque and minimum ripple conditions. These results show that the driving the SRM with the convenient switching angles may drastically reduce the torque ripple. In Table 4 the average torque and torque ripple values are shown for maximum torque and minimum torque ripple operations.

Speed (rpm)	T ave (p.u.) (max. torque)	T ripple (max. torque)	T ave (p.u.) (min. T <sub>ripple</sub> )	T ripple (min. T <sub>ripple</sub> )	Ripple Reduction (%)	T ave Reduction (%)
2000	1.67	40%	1.25	30%	10%	25%
3000	1.40	30%	1.24	12%	18%	11%
4000	1.10	40%	0.90	18%	22%	18%
5000	0.58	60%	0.50	19%	41%	14%
6000	0.35	79%	0.25	16%	63%	29%
12000	0.20	43%	0.15	19%	24%	25%

Table 4 Average torque and torque ripple variation under maximum torque and minimum torque ripple operations.

The other important issue is the efficiency of the drive. Figure 78 displays average torque per ampere value which is a good measure of high efficiency operation for the test motor at 2000 and 12000 rpm. For an m phase SRM, the torque per ampere value is defined as follows:



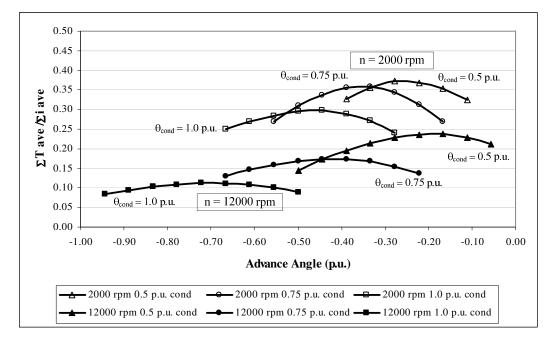


Figure 78 Simulation for torque per ampere variation versus advance angle at different conduction angles.

Figure 78 indicates that the efficiency of the SR motor at a desired torque output level greatly depends on how the control parameters are chosen. At 2000 rpm the torque per ampere ratio can take values between 0.25 and 0.38 while at 12.000 rpm this value changes roughly between 0.08 and 0.24. A closer investigation reveals that for operating an SR motor at low torque ripple with good efficiency is likely to result in lower average torque output from the shaft.

It is seen in Figure 79, Figure 80 and Figure 81 average torque and torque per ampere curves are given for 2000 rpm. In these figures it is observed that for all conduction angles there is an advance angle where the torque per ampere value reaches its maximum level. In this study this maximum torque per ampere characteristics are used for the efficiency maximization of the SRM ignoring the core and copper losses.

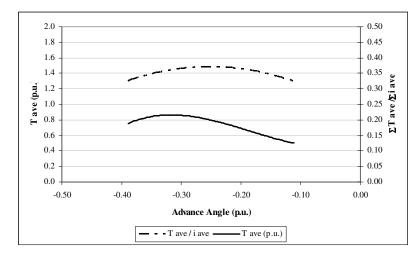


Figure 79 Average torque and average torque per ampere ( $\Sigma T$  ave /  $\Sigma i$  ave) curves for 0.5 p.u. conduction angle at 2000 rpm.

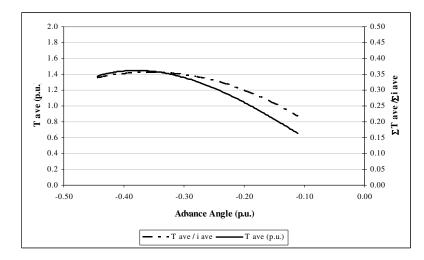


Figure 80 Average torque and average torque per ampere ( $\Sigma T$  ave /  $\Sigma i$  ave) curves for 0.75 p.u. conduction angle at 2000 rpm.

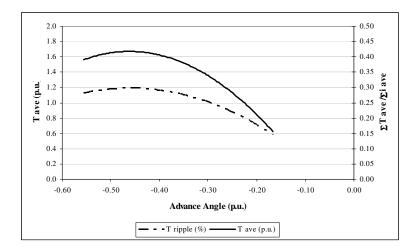


Figure 81 Average torque and average torque per ampere ( $\Sigma T$  ave /  $\Sigma i$  ave) curves for 1.00 p.u. conduction angle at 2000 rpm.

The variation of the torque per ampere and the average torque at 2000 rpm is given together in Figure 82. It is observed from this figure that it is possible to produce an average torque of 0.7 p.u. at a torque per ampere of 0.30 if the advance angle is about -0.42 p.u. at 0.50 p.u. conduction. With the same conduction, the torque per ampere value increases to 0.37 at -0.21 p.u. advance angle. If however, the conduction angle is kept as 0.75 p.u. instead of 0.5, the torque per ampere value decreases to 0.23 for the same average torque at -0.12 p.u. advance angle.

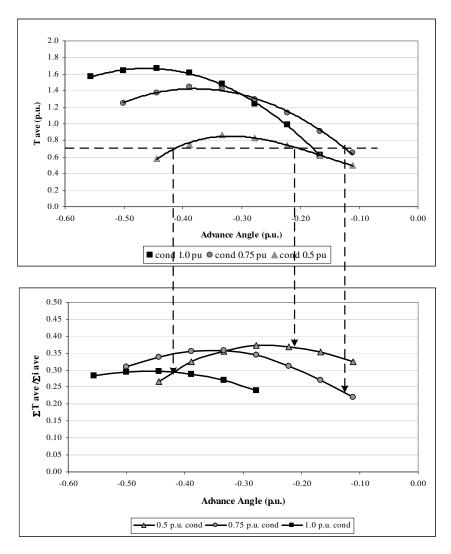


Figure 82 The advance and conduction angle determination algorithm considering maximum torque per ampere for 0.7 p.u. load torque at 2000 rpm.

In this chapter the effects of advance and conduction angles on SRM performance are investigated. This study is conducted on simulation software. The investigation covers speeds up to 12000 rpm. Only steady state operating conditions are concerned.

The results presented here reveal that while driving an SRM at a desired torque reference value, the torque ripple can be drastically reduced over the considered

speed range by proper choice of conduction and advance angles. In return, it is observed depending on the torque ripple level desired, it is necessary to derate the motor.

The study of the torque per ampere against the advance and conduction angles revealed that SR motor efficiency is greatly affected by the choice of value of the control variables. It is also observed that it is possible to operate an SRM at a required shaft torque value with minimum torque ripple and with high efficiency. However it may be necessary to derate the motor to operate it under this condition.

At this stage of the study, the relation between the torque ripple and the acoustic noise of SRM must be investigated. As a result of this investigation, if a strong correlation between the torque ripple and the acoustic noise is perceived, a controller will be designed in order to have an SR drive operation with minimum torque ripple. If the acoustic noise is not strongly related to torque ripple, the relation between the radial component of the force and the acoustic noise will be analyzed.

# 4.2. The Effect of Torque Ripple on SRM Acoustic Noise

In order to observe the effect of the torque ripple on SRM noise, the noise and torque ripple variation must be considered together. In this stage of investigation, for constant load and speed, the torque ripple and acoustic noise emission is observed. The torque ripple is obtained via simulations while the variation of the machine noise is recorded experimentally in an anechoic room.

The experimental setup and the speed controller block diagram is given in Figure 84. As it is seen, a vector controlled induction machine is used as the mechanical load. The analog voltage input of the vector controlled drive used to adjust the load

torque. The mechanical output torque of the drive is observed from the analog output of the torque transducer. By doing this, the torque production error of the induction machine drive is eliminated. The speed control of the system is achieved by SRM drive. The advance angle and the reference speed are the inputs of the SRM drive while the torque reference is accepted by the induction machine drive. With this system, the SRM is loaded with the required load torque and the conduction angle is determined by the controller. During the experiments, the induction machine drive is adjusted to produce 0.25, 0.5, 0.75 and 1.0 p.u load torque by the closed loop controller presented in Figure 84. In each load level, the advance angle is manually changed and the controller determined the required conduction angle to rotate the load at the given reference speed. In each load level, the operating conduction and advance angles are recorded as well as the machine acoustic noise. After the experiments, the torque ripple is obtained via simulations for the same conditions with the experiments. The simulator block diagram is given in Figure 83. The input variables of this simulator is obtained from the experiments. With this combination of simulation and experiments, the acoustic noise and the torque ripple variation is obtained in order to see whether a correlation exists between them or not.

The results of the proposed experiments and simulations are given in Figure 85 - Figure 88.

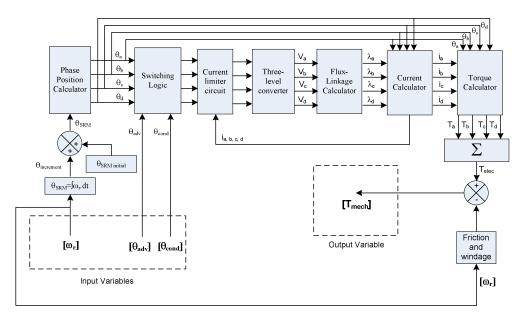


Figure 83 The simulator block diagram used for the parametric sweep of switching angles.

The torque ripple and the measured acoustic noise levels for different load levels at 2000 rpm is given in Figure 85 - Figure 88. In these figures, the turn on angle is advanced step by step and the required conduction angle is determined by the controller shown in Figure 84. This experiment is done in order to see if there is a relationship between the acoustic noise and the torque ripple or not. At the end of the chapter, in the light of the experiments, a conclusion will be made about the effect of the torque ripple on the acoustic noise.

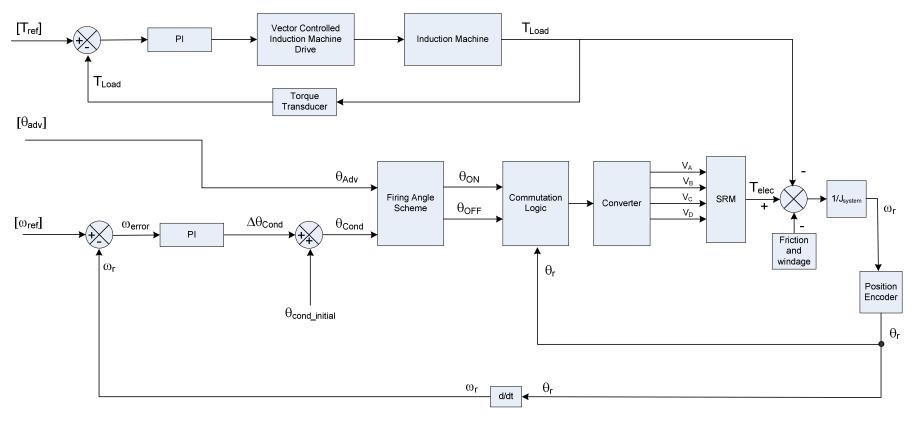


Figure 84 The experimental setup and the controller block diagram for the advance angle sweep.

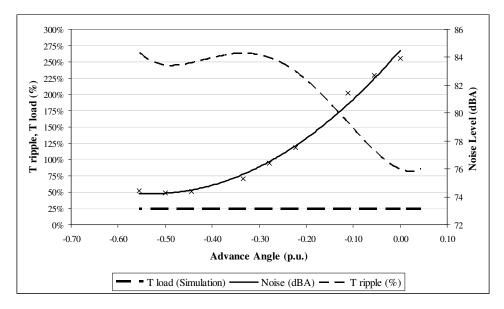


Figure 85 The torque ripple and machine noise variation under 0.25 p.u. load at 2000 rpm.

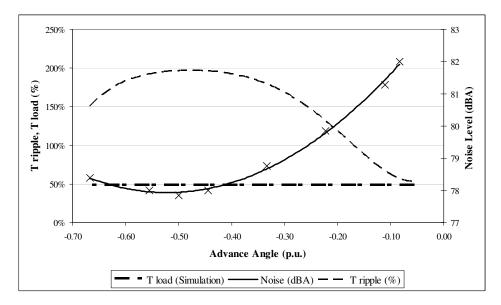


Figure 86 The torque ripple and machine noise variation under 0.5 p.u. load at 2000 rpm.

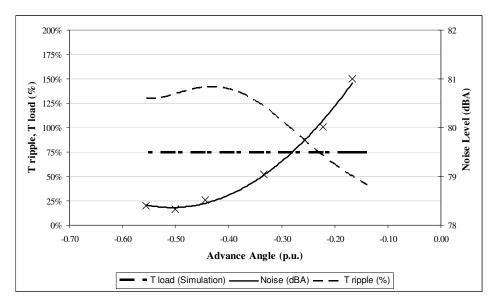


Figure 87 The torque ripple and machine noise variation under 0.75 p.u. load at 2000 rpm.

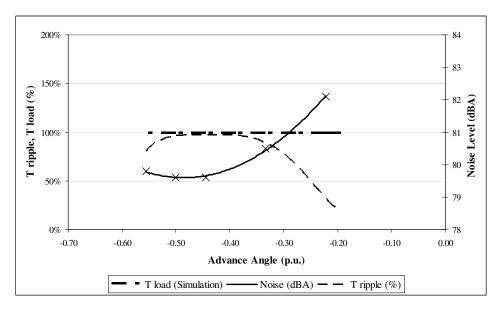


Figure 88 The torque ripple and machine noise variation under 1.00 p.u. load at 2000 rpm.

# 4.3. Conclusion

In Figure 85 to Figure 88, the simulated torque ripple and measured machine noise are presented. It is notable that, the tangential shaft vibrations are not seem to be the main source of acoustic noise as seen in these figures. In different load levels, the radiated acoustic noise decreases with the increasing advance angle at constant speed while the torque ripple increases. This is an important result since sometimes SRM torque ripple is addressed as the source of acoustic noise. In the next chapter, as the other possible noise source of SRM the radial forces are taken into consideration.

From these simulations, it is also deduced that at advancing the turn-on angle increases the average torque up to a maximum value. At each speed, the advance angle where the machine produces its maximum average torque is different. The controller which is supposed to operate reliably at high speed should consider this maximum torque point in order to avoid misjudgment beyond this advance angle point.

# **CHAPTER 5**

# **ACOUSTIC NOISE IN SRM DRIVES**

In this section, the acoustic noise components of an SRM drive will be analyzed. First, a brief literature review is presented to understand the noise production mechanism and the solution proposals are indicated. At the end of the chapter, after having a perception about the production of the airborne sound of the motor, a solution method will be offered.

# 5.1. Previous Work

The acoustic noise sources in an SRM drive are first investigated experimentally by Cameron, Lang and Umans [28]. They made 10 experiments in order to understand the main noise components of SRM. As a result, it is claimed that, the most salient noise source is the radial deformation of the stator due to the radial forces. If the frequency of the phase excitation coincides with the resonance frequency of the stator, the worst case occurs and the acoustic noise reaches to its maximum value. In [28], it is also stated that the radial vibration of the stator can be reduced by changing the PWM duty cycle to control the current harmonics. At the end of the analysis, two control methods are proposed. The first one is the current shaping method to eliminate the offending harmonics. Second, the turn-on and turn-off angles were randomly selected by  $\pm 1$  mechanical degree in order to spread the spectrum of the acoustic noise. It is supposed to reduce the radial vibration coupling to the mechanical resonance of the stator by dithering the switching angles. As a conclusion, dithering the turn-on and turn-off angles method is claimed to be more successful in reducing acoustic noise emission. In [28], the load level is not mentioned so the load dependency of the proposed method is not disclosed.

In [29], Wu and Pollock made stationary and rotary tests in order to identify the noise sources. As a result of the experiments, they concluded that the main source of vibration is the phase turn-off process where the rate of change of radial force is maximum. After having an intuition about the noise production mechanism, they proposed a two stage commutation method. This method is composed of two steps with an intermediate zero voltage loop between the positive and negative phase voltages. The duration of the zero voltage loop is equal to the half resonance cycle of the stator. This zero voltage loop initiates the first stator oscillation. After a half resonance cycle, negative voltage is applied to the phase, which is aimed to initiate the second acceleration contrary to the first one. Experimental validation of the method presented in [29] shows that the method is effective in reducing stator vibrations. The contribution of this paper is to introduce the literature with the active noise cancellation technique, which is composed of producing two oscillations 180<sup>0</sup> out of phase to cancel each other.

In [30], Pollock and Wu proposed some methods in addition to the two-stage commutation method given in [29]. First, the characteristics of the radial force is mentioned as the main reason of the deformation of the stator. It is told that the radial force reaches its maximum value at the commutation point because this force is proportional to the square of the air gap flux. When the phase commutation occurs, the phase voltage applied to the phase is reversed and the smoothly increased force between the stator and the rotor is released abruptly like a spring and a hammer effect is observed. These are *voltage smoothing* and *three*-

*stage commutation* methods and the results show that they are not as effective as the two-stage commutation method. In voltage smoothing method, PWM duty cycle is being changed gradually from unity to zero during the commutation period. No zero voltage is applied during commutation. The three-stage commutation method, which is similar to the two-stage method, aims to cancel the first oscillation with the second one but produced by negative voltage instead of zero voltage. The three-stage commutation method can be summarized as follows:

- i.  $+V_{DC}$  during conduction period,
- ii.  $-V_{DC}$  for only a half resonance cycle, ( $1^{st}$  stage)
- iii.  $+V_{DC}$  for a ratio of the resonance cycle,  $(2^{nd} stage)$
- i.  $-V_{DC}$  until the current decays to zero. ( $\beta^{rd}$  stage)

Although the simulation and experimental results of this method are not better than the two-stage commutation method, this approach suitable for two-level converters.

The two-stage commutation method gives good results at high speed but below base speed, just before the commutation, the phase is exposed to the chopping voltage instead of the full DC link voltage. During chopping action, the average value of the phase voltage varies with the motor speed. In [31], Michaelides and Pollock take this chopping period into account and present an active noise cancellation method to be valid for low speed region. This method considers the phase voltage as the key parameter of the noise emission and tries to apply equal average voltages in opposite signs during commutation. It is observed from experiments that this speed dependent active noise cancellation technique is effective at low speed and may be regarded as the extension of the two-stage commutation method for low speed region. It is deduced from the experimental studies presented in [28], [29], [30] and [31] that the vibration mode resonance frequencies are very important in acoustic noise emission. To calculate these mode frequencies by structural FEA gives good results but this approach needs much effort. In [32], Colby, Mottier and Miller developed an analytical method for the prediction of the dominant Eigen mode without using structural FEA. These results are compared with the results obtained by FEA and satisfactory agreement is observed. These analytical methods are efficacious for rapid analysis of the sound models and for preliminary design studies to evaluate the effect of the dimensions on acoustic noise.

In [33], acoustic noise mitigation and the torque ripple minimization problem are dealt with together at low speed. A current shaping method is proposed such that both of these performance criteria are taken into account. In this study, Fahimi et al. show that the radial force reaches to its maximum value at aligned (IN) position and minimum value at unaligned (OUT) position as it is stated in the previous studies (Figure 89).

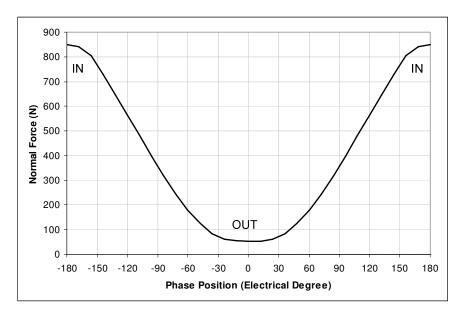


Figure 89: Radial component of the force as a function of rotor position.

The proposed algorithm in this paper is based on minimization of the radial force as well as the shaft torque ripple. Because the problem is multi objective, none of the problems is solved completely, but only a compromise is made between the criteria. A current shaping algorithm is proposed to minimize the rate of change of this radial force so the method is valid for up to base speed.

In [34], Rasmussen et al. presented an acoustic noise model combining the radial force with the generated sound pressure. They proposed a complete dynamical model where the parameters can be calculated based on the geometry of the motor. The consistency between the simulation results with the experimental sound measurements seems to be accurate enough. The vibrational and acoustical model is verified in both time and frequency domains.

In [35], a rough analytical calculation made and it is shown that the radial force is always multiple times that of the tangential force. In fact, in all electrical machines, the radial force magnitude is much more than the tangential force but here, the stroke based operation of the SRM deteriorates the squeezing and instant releasing effect of the radial forces on the stator.

In [36], Kasper et al. analyzed the noise development in SRMs with a special focus on the influence of the radial force. First, they made a review of the existing current shaping and zero-voltage freewheeling methods from the point of the harmonic spectrum view. Second, they proposed a triangle-width strategy considering both the electrical excitation frequency and the eigenfrequencies of the stator. In the end, the early single pulse strategy is proposed. In their method the phase is turned on far from the alignment position in order to flatten the radial forces. They implemented the early single pulse strategy in a multi-purpose drive and it is observed that the airborne noise was reduced by 4.5 dBA compared with a standard hysteresis current control. In this method, both the current rating of the drive and the torque ripple increases. Note that, since the selection of the phase commutation angle is not flexible at full load, the motor must be de-rated. This is an expected result as previously indicated in [29].

By investigating the literature a general view of the subject matter is obtained and the state of the art is understood. In this chapter, the physical phenomena involves the noise reduction is investigated.

# 5.2. Acoustic Noise Sources in SRM Drives

Noise sources in an SRM drive are given in Figure 90. More or less, all of these items exist in any electrical machine drive but the type of the motor changes the weighting of the component in the total acoustic noise level.

Since the mechanical coupling, load and foundation noises are beyond the scope of this study, only the noise emitted from the motor frame will be focused on. In Figure 90, these are summarized under motor item. Note that, since the scope of this study is to control the magnetic behavior of the SRM instead of the structural machine design, only the control of the magnetic noise sources will be dealt with. These noises are born due to the Maxwell force between the stator and the rotor during phase excitation. In this section, the noise developing mechanisms due to the stator and the rotor vibrations are analyzed.

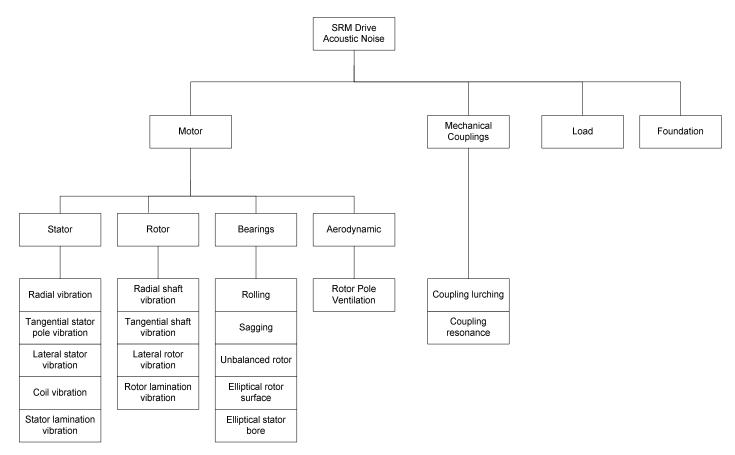


Figure 90 Acoustic noise sources in an SRM drive.

# 5.2.1. Magnetic Noise Sources

In this section, ignoring the bearing and the aerodynamic noises, structure born noises emitted from the stator and the rotor will be analyzed.

Both the step by step operating principle of the drive and the doubly salient nature make SRM intrinsically a noisy machine. As in any other electrical machine, during the electromechanical energy conversion cycle, three types of forces are produced:

- Radial forces (Figure 91 a),
- Tangential forces (Figure 91 b),
- Lateral forces (Figure 91 c).

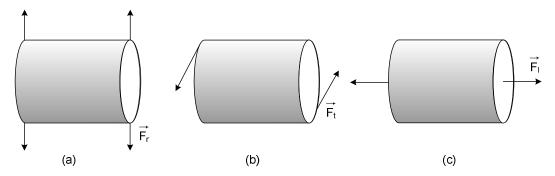


Figure 91 Radial, tangential and lateral forces.

In Figure 92, ignoring the lateral forces, the rotor pulling force  $(F_{r,t})$  and its components  $F_r$ ,  $F_t$  are shown. Note that, both radial and tangential forces are produced with the same phase current so it is not possible to control these forces independently.

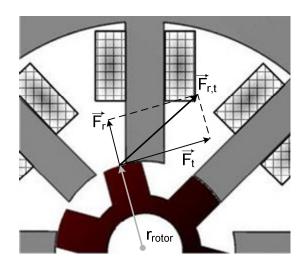


Figure 92 Radial and tangential forces acting on the rotor during excitation.

The noise production mechanism of SRM is different in rotor and stator sides. The rotor side is exposed to the shaft torque ripple due to the pulsating tangential force  $F_t$ , which is the reason of the rotational vibration. On the other hand, the stator side behaves like a ring plate in radial direction due to the pulsating radial force  $F_r$ .

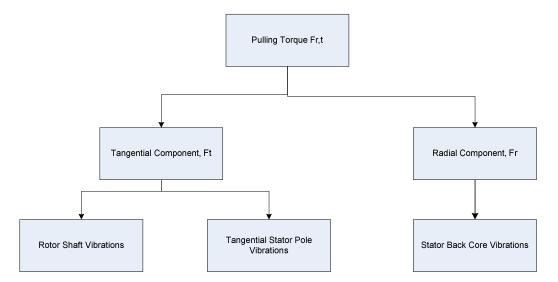


Figure 93 The effects of radial and tangential forces on both stator and rotor sides.

# 5.2.2. Stator Reaction

The components of the pulling force acting on the stator are shown in Figure 94.

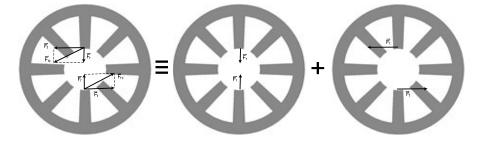


Figure 94 Superposition of the radial (a) and tangential forces (b) acting on the stator.

The effects of these components can be analyzed by superposition and the deformation of the stator due to these forces can be approximated like in Figure 95 and Figure 96.

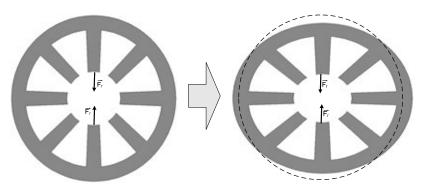


Figure 95 Effect of the radial component of the pulling torque.

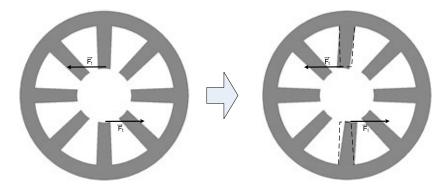


Figure 96 Effect of the tangential component of the pulling torque.

As a result, the radial component of the pulling force  $F_r$  tries to make the stator oval, while the tangential component  $F_t$  initiates the vibrations on the stator poles. The stator reaction is investigated in the next section.

# 5.2.2.1 Effect of the radial force component on the stator yoke

During the fluxing period, which is generally resides in the positive torque region before the aligned position, the phase is applied with the positive DC link voltage so the flux in the stator and the rotor core tends to increase.

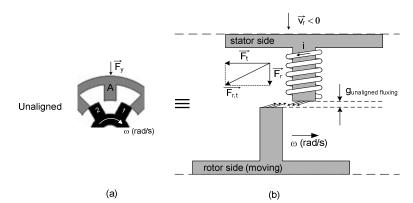


Figure 97 Fluxing period of an SRM phase (a) and its force producing mechanism (b)

As a result of this flux-linkage, the stator and rotor teeth is exposed to force  $F_{r,t}$  which has two components (Figure 92 and Figure 97 b):

- Radial Force  $(F_r)$
- Tangential Force (F<sub>t</sub>)

Note that the rotor and stator forces are opposite to each other as seen in Figure 92 and Figure 97 (b).

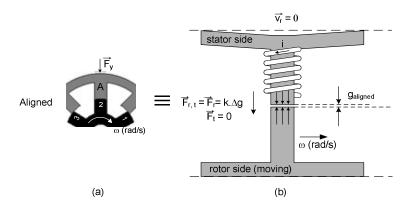


Figure 98 The end of the fluxing period of an SRM phase (a) and its force producing mechanism (b)

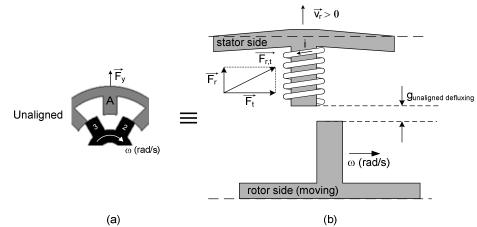


Figure 99 Defluxing period of an SRM phase (a) and its radial movement due to the radial force release (b).

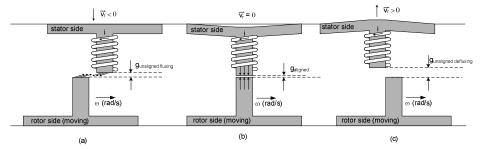


Figure 100 Stator bending mechanism of SRM phase during fluxing (a, b) and defluxing period.

The most critical stage of SRM stator noise is the transition from (b) to (c) in Figure 100. Transition from (a) to (b) is a developing period but from (b) to (c) is abrupt. This may be thought as a spring which is being compressed slowly and released abruptly. Without solving differential equations, it can be deduced that the releasing instant initiates more vibration than the compression period.

In literature, the radial vibration of the stator is indicated as the major noise source of SRM [28], [29], [30] and [34]. Especially the experimental study results presented in the milestone paper on SRM noise [28] indicates the strong correlation between the stator vibration and the acoustic noise.

# 5.2.2.2 Effect of the tangential force component on the stator pole

The stator pole acts like a cantilevered beam subjected to a force at the free end as seen in Figure 101. The tangential force acting on the stator can be considered as the bending load for the stator pole. While the phase is unexcited, no bending force is applied to the stator pole. Under excitation, magnitude of the tangential force changes with the rotor position. The relation between the phase tangential force and the phase torque is as follows:

$$T_e = 2x F_t \cdot r_{rotor} \tag{81}$$

The tangential force and the phase torque are interdependent each other by a constant. The relation given in (81) also shows that the tangential force increases with the load torque. In the aligned position, both of the phase torque and the tangential force are zero (Figure 102). This is an important finding since at this point, phase current has no effect on the phase torque but the radial force component has its maximum value under constant excitation level.

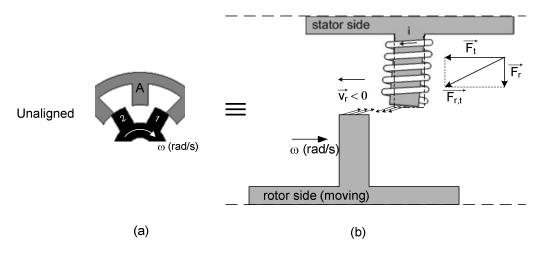


Figure 101 Fluxing period of an SRM phase (a) and its tangential force (Ft) producing mechanism (b)

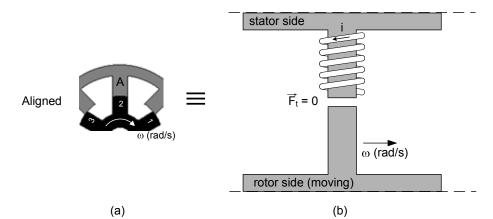


Figure 102 Aligned position of the rotor. At this position tangential force (Ft) is zero but stator pole continues to vibrate.

After the phase commutation, although the phase excitation is over, the triggered vibration may continue according to the amount of stator pole displacement Figure 103. The stator pole tangential displacement is inversely proportional to the stator pole base stiffness. The movement of the stator pole during and after the phase excitation is summarized in Figure 104.

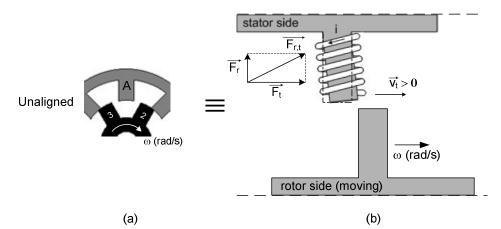


Figure 103 Unaligned position of the rotor. The stator pole continues to vibrate.

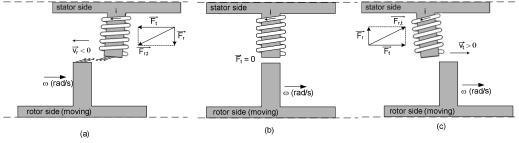


Figure 104 Stator pole bending mechanism of SRM phase during fluxing (a, b) and defluxing period (c).

Here, as it is shown that the electrical torque is proportional to the tangential force  $F_r$ . The frequency of this pulsating force is equal to the frequency of the shaft torque ripple.

In literature, no major indications are observed about the acoustic noise effect of the tangential vibration of the stator pole so only the radial vibration of the stator will be investigated in this study.

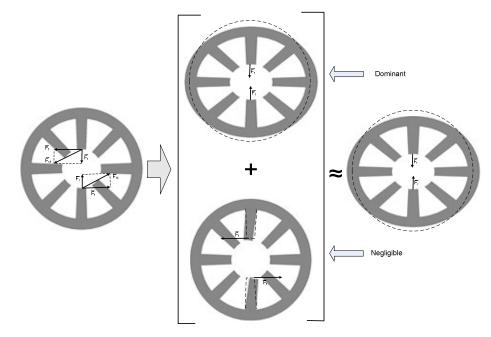


Figure 105 The resultant approximate shape of the SRM stator facing a pulling force.

#### 5.2.3. Rotor Reaction

According to the Newton's third law, for every *action force* there is an equal (in size) and opposite (in direction) *reaction force*. Since the deformation of the stator comes from the magnetic attraction of the rotor, the same forces act on the rotor side with equal in size but in reverse direction.

As it is seen in Figure 106, the rotor is pulled symmetrically in radial direction but it cannot be stretched along this force since it is stiffer than the stator so the radial force does not have a major vibration effect on the rotor side. Remember from the previous section that, the *shear load* acting on the stator yoke and the *bending moment* acting on the stator pole make it deflected towards the rotor tooth.

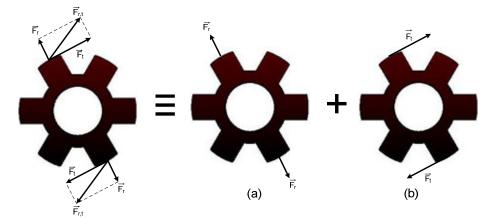


Figure 106 Superposition of the radial (a) and tangential (b) forces acting on the rotor.

Note that, the electrical torque is proportional with the tangential force (Figure 92):  $T_e = 2 x F_t r_{rotor}$ (82)

Although the electrical torque is a figure of the mechanical output of the motor, the radial force has no meaning from the point of the motor mechanical output view.

$$P_{mech} = T_{mech}.\omega$$

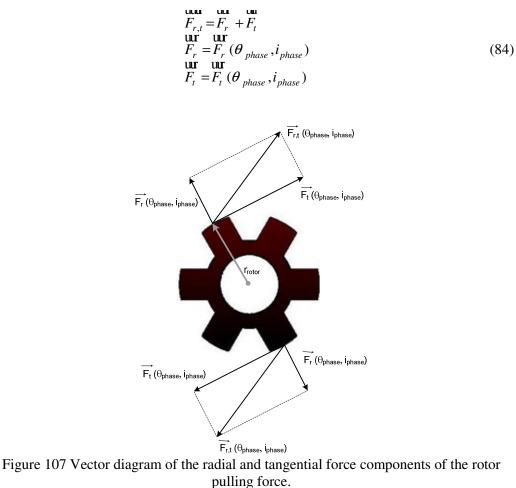
$$T_{mech} = T_{elec} - T_{f\&w}$$
(83)

Although the rotor is exposed to the same forces with the stator, due to its stiffness and ruggedness, it is assumed in literature that no significant deformation or vibration occurs on it. On the contrary, generally it is claimed that either the tangential or the radial forces have no sound producing effect on the rotor [28], [34]. In this study, the noise contribution of the rotor is neglected as in previous researches and it is left for a future study.

#### 5.2.4. Frequency of the tangential and radial forces:

In Figure 107, the radial and tangential components of the pulling force  $F_{r,t}$  of an SRM is shown.

Here, since the tangential and radial forces are both the functions of the phase position and current, the mathematical expression of Figure 107 is basically as follows:



From (84) it is deduced that the frequency of the radial and the tangential force pulsation are the same. Once the torque ripple frequency is obtained as a function of the mechanical motor speed, the tangential force frequency is also obtained since they are both the functions of the phase position and current.

Generally the speed of a rotational system is expressed in rpm. In an SRM, the number of steps is equal to the number of torque pulsations per revolution.

Since each phase must be excited for once during a single electrical cycle, the electrical step size of an SRM is as follows:

$$\theta_{step\,elec} = \frac{2.\pi}{N_{phase}} \tag{85}$$

Besides, each rotor pole comes across every motor phase for once in each mechanical revolution, the *electrical angle* is  $N_r$  times the *mechanical angle*:

$$\boldsymbol{\theta}_{elec} = N_r \cdot \boldsymbol{\theta}_{mech} \tag{86}$$

Substituting (86) into (85) gives the mechanical step size of an SRM as a function of the rotor pole and the motor phase number:

$$\theta_{step mech} = \frac{2.\pi}{N_{phase}.N_r}$$
(87)

The number of phases is generally half the stator pole number since the phase coils are connected in series in couple (Figure 108):

$$N_{phase} = \frac{Ns}{2} \tag{88}$$

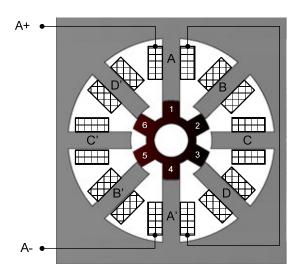


Figure 108 A four phase SRM cross-section with eight stator poles and six rotor poles.  $(N_s/N_r = 8/6)$ 

The number of steps in each revolution is equal to *pulse per revolution* (ppr):

$$ppr = \frac{2.\pi}{\theta_{mech\ step}} \tag{89}$$

Substituting (87) and (88) into (89) yields:

$$ppr = \frac{N_s \cdot N_r}{2} \tag{90}$$

Hence, the torque pulse per minute is:

$$ppm = n_r \cdot ppr$$

$$ppm = n_r \cdot \frac{N_s \cdot N_r}{2}$$
(91)

The torque pulsation or ripple frequency is:

$$f_{torque\,ripple} = n_r \cdot \frac{Ns.Nr}{2} \cdot \frac{1}{60} \tag{92}$$

As mentioned before, torque ripple frequency is equal to both the radial and tangential force frequency in Hz:

$$f_{Fr} = n_r . \frac{Ns.Nr}{2} . \frac{1}{60}$$
(93)

$$f_{Ft} = n_r . \frac{Ns.Nr}{2} . \frac{1}{60}$$
(94)

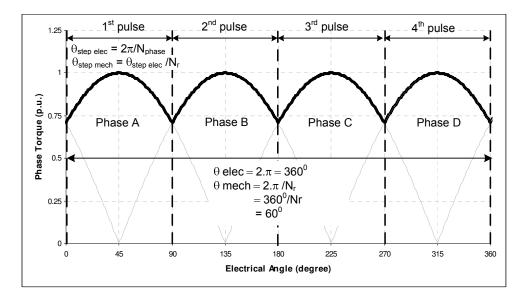


Figure 109 Torque pulses of a four phase SRM during unity electrical cycle. ( $N_s/N_r = 8/6$ )

In Figure 109, the torque pulses are shown during unity electrical cycle for a four phase SRM. As seen in this figure, the number of the torque pulses per electrical cycle is equal to the phase number which is generally the same with the stator pole pair number. Since the mechanical unit cycle is composed of  $N_r$  times the electrical cycle, there are ( $N_{phase} \times N_r$ ) torque pulses per revolution in an SRM. This result is the same with the obtained in (90).

#### 5.2.5. Acoustic Noise Stemming From Radial Forces

In this section, the source of the radial emitted acoustic noise will be analyzed. First, a simple magnetic model will be presented in order to understand the noise production mechanism on the stator side. Next, a mathematical model will be proposed for the displacement, velocity and acceleration of the stator. Depending on this model, the effect of the radial forces will be considered and a solution will be suggested. As it is stated before, the radial and tangential forces have little vibration effect on the rotor, only stator side will be investigated.

#### 5.2.5.1 Acoustic Noise Model of the Stator

In order to explain how radial emitted acoustic noise of electromagnetic origin can be predicted, the stator-rotor structure of SRM will be used in Figure 110.

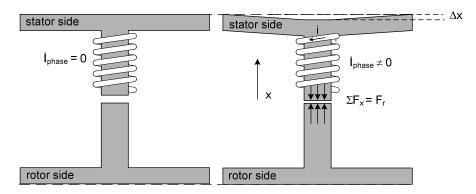


Figure 110 Structure for modeling acoustic noise of electromagnetic origin

The magnetic structure is a coil resides on the stator pole and a stiff rotor pole. The stator yoke is assumed the unique deflecting part of the system so mathematical model will include only the deflection, velocity and acceleration of this part.

As it is well known from mechanics, the deflection of the stator yoke depends on the radial force, Fr, and the elasticity modulus of the stator yoke in x direction.

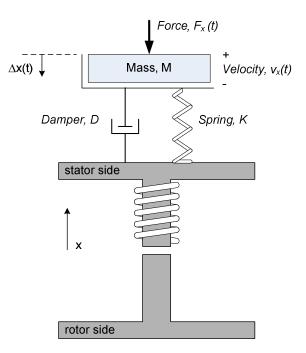


Figure 111 Single phase vibrational model for the SRM stator yoke

The mathematical model for the single phase stator vibration is as follows:

$$\frac{d^2 x}{dt^2} = \frac{1}{M} \cdot \left(F_x - D \cdot v_x - K \cdot x\right)$$

$$\frac{dx}{dt} = v_x$$
(95)

Here, M is the equivalent mass, K is the spring constant and D is the damping coefficient of the stator yoke. Since the force acting on the stator pole is in radial direction in an SRM,  $F_r$  will be used instead of  $F_x$  for convenience. The radial force is the source term of the differential equations given in (95) and it is a function of the phase position and current.

$$F_{x} = F_{r} \left( \theta_{phase}, i_{phase} \right) \tag{96}$$

Substituting (96) into (95) yields

$$\frac{d^{2}x}{dt^{2}} = \frac{1}{M} \cdot \left(F_{r}\left(\theta_{phase}, i_{phase}\right) - D \cdot v_{x} - K \cdot x\right)$$

$$\frac{dx}{dt} = v_{x}$$
(97)

These state equations will be used for modeling the vibrational behavior of the stator yoke. The block diagram of (97) is given in Figure 112.

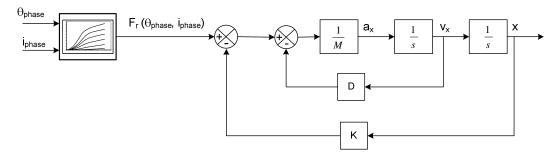


Figure 112 Block diagram of the displacement model for an SRM stator yoke.

In Figure 112,  $a_x$  is the acceleration,  $v_x$  is the velocity and x is the radial displacement. Note that, the sound pressure is directly related with the stator radial velocity,  $v_x$ .(Figure 113 and (98)).

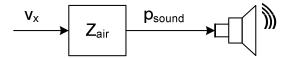


Figure 113 The relation between the sound pressure and stator yoke radial velocity

$$p_{sound} = Z_{air} . v_x \tag{98}$$

Here,  $Z_{air}$  is the *characteristic acoustic impedance* of the air and equal to 413.2 kg.m<sup>-2</sup>.s<sup>-1</sup> at room temperature.

# 5.2.5.2 Radial Force Data

The radial and the tangential forces have the same independent parameters. They are both functions of the phase position and current.

$$F_r = F_r \left( \theta_{phase}, i_{phase} \right) \tag{99}$$

$$F_t = F_t \left( \theta_{phase}, i_{phase} \right) \tag{100}$$

Besides, phase torque  $(T_{phase})$  is a function of the tangential force, *Ft*:

$$T_{phase}\left(\theta_{phase}, i_{phase}\right) = 2.r_{rotor}.F_t\left(\theta_{phase}, i_{phase}\right)$$
(101)

Here,  $r_{rotor}$  is the rotor outside diameter which relates the tangential force with the phase torque. From (99) and (100) it is obvious that both functions have the same parameters and any control method acting on tangential force  $F_t$  also changes the radial force,  $F_r$ . Any suggested control method should be considered from the point of these forces view.

Contrary to the static torque curves, the radial force data cannot be measured directly. Instead, there are some indirect methods to obtain the attraction between the stator and the rotor. In this study, the radial force data of the test motor is calculated by using finite element analysis (FEA). The results are given in Figure 114.

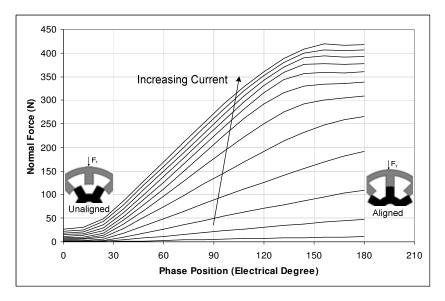


Figure 114 Calculated radial force data by using FEA as the parameter of phase position.

It is sure that, the general characteristics of these curves are common for all SRMs. From the point of the peak radial force minimization problem, the characteristics of these forces are much more important than their actual magnitudes. For this reason, a p.u. transformation is made by choosing 430 N as the base value which is the largest force level of the calculated data (Figure 114). By using this dimensionless data, the problem becomes independent of the absolute value of the radial forces (Figure 115).

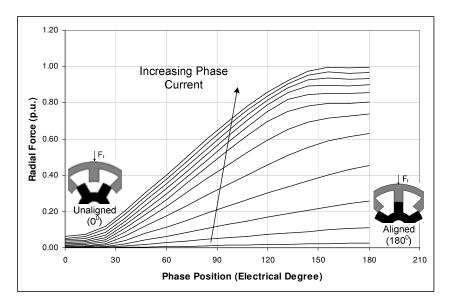


Figure 115 Radial force characteristics in p.u.

As it is seen in Figure 115, the radial force is a function of the phase position and current. In the next section a model is presented which establishes the relation between the radial force and acoustic noise.

# 5.2.5.3 Model Parameters

The mathematical model given in (97) involves some geometry and material dependent parameters. Here, a rough investigation is made in order to show the general properties of these differential equation coefficients.

# **Spring Constant, K:**

For a vibrating ring, the spring constant K is calculated as follows:

$$K = \frac{E.I}{2(0.5R_{outer} + 0.5R_{inner})^{3}} \left( \frac{1}{\frac{\theta - \sin\theta \cos\theta}{4\sin^{2}\theta} + \frac{\cos\theta}{2.\sin\theta} - \frac{1}{2\theta}} + \frac{1}{\frac{\sin\theta - \theta \cos\theta}{4\sin^{2}\theta} - \frac{1}{2.\sin\theta} + \frac{1}{2\theta}} \right)$$
(102)

E is the elasticity modulus and the moment of inertia I is calculated by (103).

$$I = \frac{\left(R_{outer} - R_{inner}\right)^3 L_{stack} \cdot \sigma_{stack}}{12\left(1 - \nu^2\right)}$$
(103)

 $L_{stack}$  is the stator stack length and  $\sigma_{stack}$  is the stacking factor.  $R_{outer}$  and  $R_{inner}$  are the dimensions of the stator.  $\theta$  is a function of mode frequency number and v is the *Poisson's ratio*.

$$\theta = \frac{\pi}{n} \tag{104}$$

#### **Equivalent Mass, M:**

If the dominating mode frequency  $f_n$  is known, the equivalent mass is calculated as follows:

$$M = \frac{K}{\omega_n^2} \tag{105}$$

The dominating resonance frequency is given by

$$\boldsymbol{\omega}_n = 2.\boldsymbol{\pi}.\boldsymbol{f}_n \tag{106}$$

And  $f_n$  is calculated by Rayleigh formula given in (107).

$$f_n = \frac{n(n^2 - 1)}{2\pi\sqrt{1 - n^2}} \sqrt{\frac{E.I}{\mu.(0.5(R_{outer} - R_{inner}))^4}}, \quad n > 1$$
(107)

$$\mu = \frac{\pi . \left(R_{outer}^2 - R_{inner}^2\right) . L_{stack} . \sigma_{stack} . \rho_{stator}}{\left(R_{outer} + R_{inner}\right) . \pi}$$

Here, n is the number of resonance mode and  $\rho_{stator}$  is the stator iron density.

#### **Damping Constant, D:**

The damping constant D is a function of equivalent mass and spring constant.

$$D = 2\zeta M \sqrt{\frac{K}{M}}$$
(108)

where  $\zeta$  is the damping factor of the stator yoke.

## 5.2.6. Solution Suggestion

The validation of the model given in Figure 112 is not an easy task and decoupling the mechanical system of the test bed from the test motor is not possible. The geometry dependency of the state equation coefficients M, K and D makes the analysis more difficult (97). The calculation of these mechanical lumped parameters by numerical field solutions such as finite element analysis for a given geometry is beyond the scope of this study.

The model given in (97) is not used here but the findings are important. The contribution of this model is to disclose the effect of the radial force  $F_r$  on *acceleration, velocity* and *displacement* of the stator yoke which are the parameters contributing to the radial emitted acoustic noise as given in (98). So the target here will be to operate the motor so as to minimize the radial forces and hence the acoustic noise rather than being concerned with its absolute value. It is clearly observed from (95) that, the *displacement, velocity* and *acceleration* of the stator yoke is supplied by the radial force  $F_r$ . (109).

$$\|a_{x}\| \alpha \|F_{r}(\theta_{phase}, i_{phase})\|$$

$$\|v_{x}\| \alpha \|F_{r}(\theta_{phase}, i_{phase})\|$$

$$\|x\| \alpha \|F_{r}(\theta_{phase}, i_{phase})\|$$

$$(109)$$

Combining (98) with (109) reveals the relation between the radial force and the sound pressure:

$$\left\| p_{sound} \right\| \boldsymbol{\alpha} \left\| F_r \left( \boldsymbol{\theta}_{phase}, i_{phase} \right) \right\|$$
(110)

According to (110), it is supposed that to minimize the peak value of the radial force will also minimize the acoustic noise:

$$\left\|F_{r,peak}\left(\theta_{phase}, i_{phase}\right)\right\| = \left\|p_{sound}\left(\theta_{phase}, i_{phase}\right)\right\|$$
(111)

If the radial force magnitude is kept as small as possible, the radial stator yoke velocity is also supposed to be small.

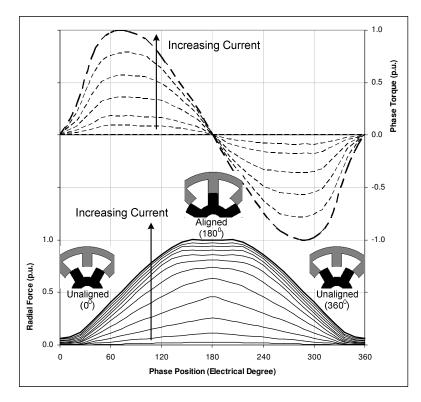


Figure 116 Phase torque and radial force data in p.u.

It must be noted that, any control acting on the phase torque obviously affects the radial forces as seen in (99) and (100). A high grade average torque controller must take the peak radial force into account to achieve a silent operation. In Figure 116, the relation between the phase torque and the radial force is presented. In unaligned position,  $(0^0 \text{ or } 360^0)$  both the radial force and the phase torque have their minimum value. But in aligned position (180<sup>0</sup>), the radial force reaches its maximum level while the phase torque is zero. This is an important point because the aligned phase current has no effect on the shaft torque but makes a great contribution to the radial force which triggers the stator vibration. In Figure 117, the problem components and the solution offer is summarized.

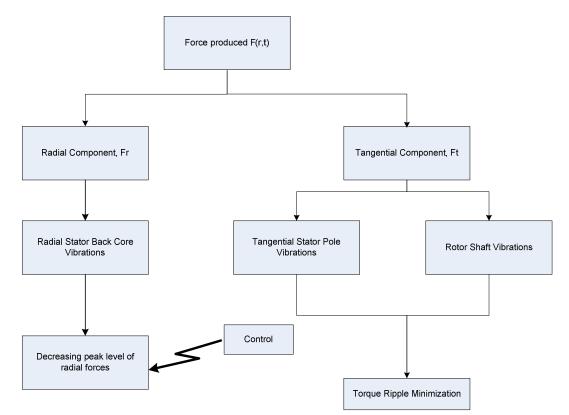


Figure 117 The problems arose with the rotor pulling torque and the suggested solution.

In the next chapter, a controller design based on this understanding of the problem is presented.

In this chapter, the effects of the radial and the tangential force components between the stator and the rotor is investigated and an intuition is obtained about the acoustic noise development mechanism in an SR motor. In the next chapter the controller design to minimize the radial force will be presented.

# **CHAPTER 6**

# A CONTROLLER DESIGN TO MINIMIZE ACOUSTIC NOISE IN SRM DRIVES

In this chapter, based on the investigation of acoustic noise production mechanism of an SR motor presented in the previous chapter, a controller is developed. First the effect of the commutation angles on radial force will be analyzed via simulations. The object of this study is to see the variation of the peak radial force with the advance and conduction angles. According to the results obtained from this study, a controller will be proposed to drive the load torque at a given reference speed with the minimum peak level of the radial forces.

# 6.1.1. The Effects of Control Parameters on Radial Forces

In order to understand the effect of the advance and conduction angles on the peak radial force, first a parametric sweep is done via simulations. In these simulations the conduction angle is kept constant as a parameter and the advance angle is kept as a variable. Through constant conduction variable advance angle simulations, the variation of the peak radial force levels are observed. The instantaneous radial force is calculated by using the radial force data given in Figure 115.

In figures Figure 118 to Figure 120, the peak radial force variation with respect to advance angle are given for different conduction angles at 2000 rpm. Although the peak radial force level differs in different conduction periods, the general

characteristics of the curves are common. Peak radial force gets smaller as the advance angle increases. It is also observed that the peak radial force mitigation is greater at small conduction angles.

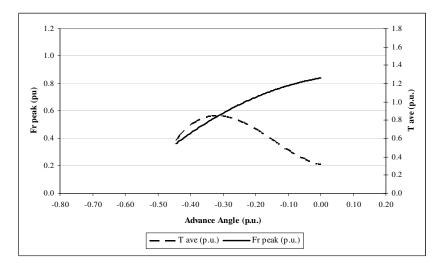


Figure 118 Radial force and average torque variation with respect to advance angle for 0.5 p.u. conduction angle at 2000 rpm.

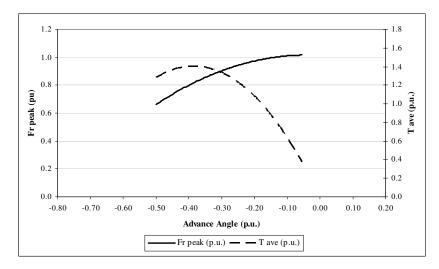


Figure 119 Radial force and average torque variation with respect to advance angle for 0.75 p.u. conduction angle at 2000 rpm.

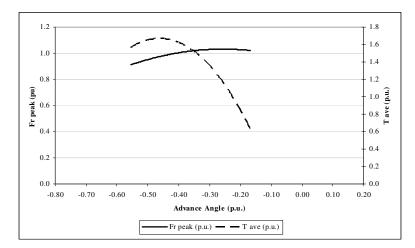


Figure 120 Radial force and average torque variation with respect to advance angle for 1.0 p.u. conduction angle at 2000 rpm.

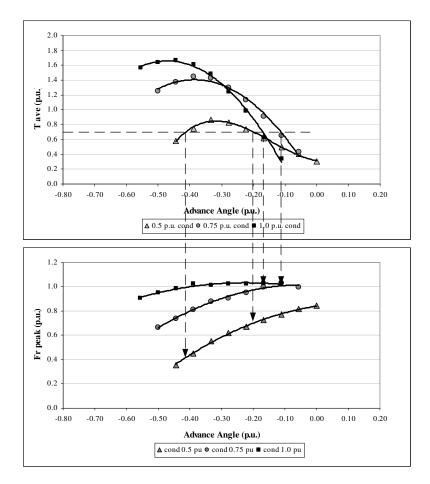


Figure 121 The advance and conduction angle determination algorithm considering peak radial force level for 0.7 p.u. load torque at 2000 rpm.

In Figure 121 the average torque and the peak radial force levels are given for different conduction angles at 2000 rpm. When this figure is closely investigated, it can be deduced that, it is possible to produce an average torque of 0.7 p.u. at a peak radial force of 1.0 p.u. if the advance angle is about -0.10 p.u. at unity conduction. If however, the conduction angle is kept as 0.5 p.u. instead of unity, the same average torque is produced at -0.18 p.u. advance angle with 0.7 p.u. peak radial force. It is noteworthy that, keeping the conduction angle at 0.5 p.u at -0.40 p.u. advance angle, the reduction in the peak radial force is drastic and it decreases to 0.40 p.u.

The results presented here revealed that while driving an SRM at a desired torque reference value, the peak radial force can be drastically reduced by proper choice of conduction and advance angles. In return, it is observed that, depending on the peak radial force level desired, it may be necessary to derate the motor.

As a second step of the controller design, variable conduction-variable advance angle simulations are made. By doing this, possible combinations of the advance and conduction angles are investigated to give a constant mechanical output. As a starting point, simulations are made at 2000 rpm for four load torque levels: 0.25, 0.5, 0.75 and 1.0 p.u. In Figure 122 to Figure 125, the peak radial force variation with respect to advance angle under constant mechanical output is presented.

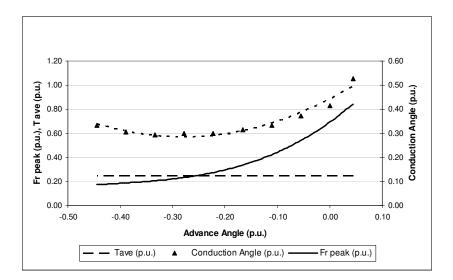


Figure 122 The peak radial force variation for 0.25 p.u. load torque at 2000 rpm (Simulation).

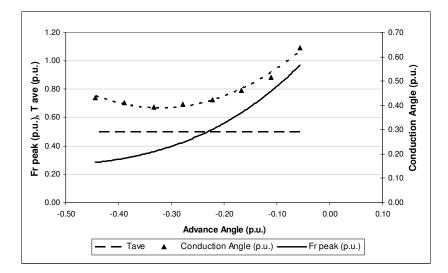


Figure 123 The peak radial force variation for 0.5 p.u. load torque at 2000 rpm (Simulation).

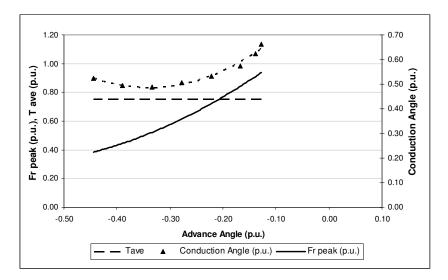


Figure 124 The peak radial force variation for 0.75 p.u. load torque at 2000 rpm (Simulation).

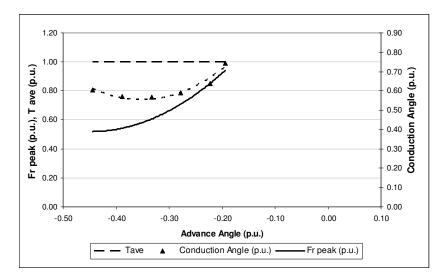


Figure 125 The peak radial force variation for 1.0 p.u. load torque at 2000 rpm (Simulation).

From Figure 122 to Figure 125, it is seen that the minimum level of the peak radial force increases with the increasing load. This indicates that the motor must be derated for a silent operation as mentioned before. The simulation results for different load levels at 2000 rpm presented here can be re-organized as in Figure

126 to give an intuition about the general characteristics of the radial forces at constant load constant speed operation.

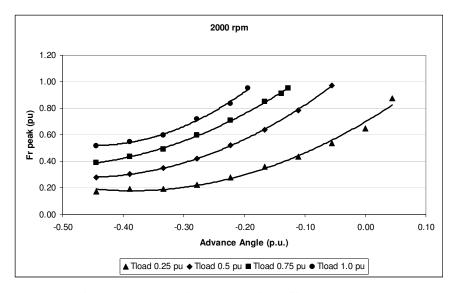


Figure 126 The peak radial force levels for different loads at 2000 rpm

The constant load simulations given for 2000 rpm are repeated for other speeds in order to see the characteristics at different speeds. In Figure 127 - Figure 130 the results are given. The simulations are made from 1200 to 2500 rpm as to observe the peak radial force characteristics below and above the test motor base speed which is 1500 rpm. In this analysis, the load torque is taken as a parameter and it is observed that under unity load, the peak radial force reduction is minimum. This result is an expected result as the number of the advance and conduction angle combinations are limited under full load.

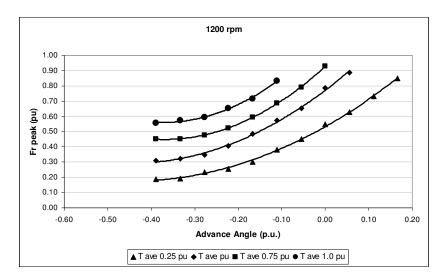


Figure 127 The peak radial force levels for different loads at 1200 rpm.

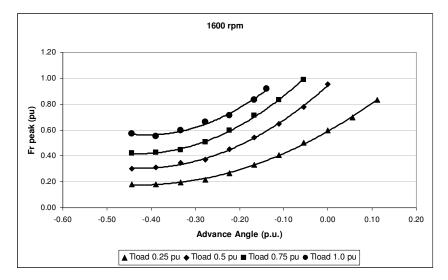


Figure 128 The peak radial force levels for different loads at 1600 rpm

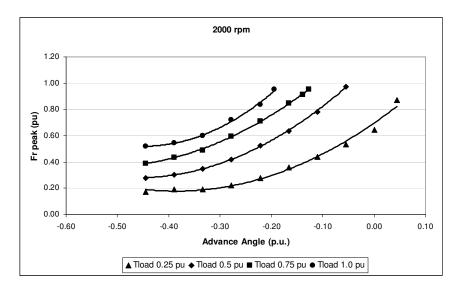


Figure 129 The peak radial force levels for different loads at 2000 rpm

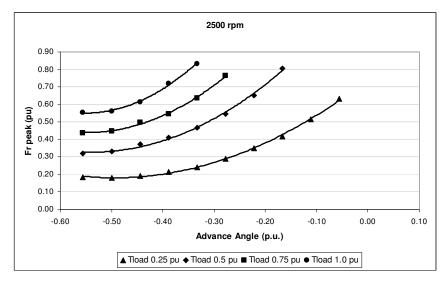


Figure 130 The peak radial force levels for different loads at 2500 rpm.

In the design stage of the controller, the results obtained from the foregoing simulations will be used to train a neural network which is capable of selecting the convenient conduction and advance angles to minimize the acoustic noise. It must be stated that, the combination of the conduction and advance angles to give the same mechanical output is not unique. For a silent operation, they should be selected such that the peak radial force is kept in a minimum level while supplying the average torque demand.

In this section, the radial force characteristics are obtained via simulations. The findings of this theoretical and simulation study will be used to design a controller. The sound mitigation performance of the proposed controller will be verified experimentally by sound measurements.

## 6.1.2. Efficiency

Whatever the main problem is, in any electrical machine drive, the proposed method should consider the drive efficiency as well. In this study, the efficiency problem is investigated by taking the torque per ampere characteristics of the motor into account as given in Chapter 4. In [37] and [38], the effects of the advance and conduction angles on the mechanical output of SRM is presented. In these studies, Bizkevelci, Ertan and Leblebicioğlu proposed a method for producing the desired load torque with minimum torque ripple or maximum torque per ampere. In this study, the motor torque per ampere characteristics will be used to increase the drive efficiency. The torque per ampere characteristics obtained via simulations in Chapter 4 is used to train a neural network which tends to operate the motor at its maximum torque per ampere points. Since the core and copper losses are not taken into account in this study, the maximum torque per ampere points may not be the most efficient points but it is supposed that the motor efficiency will increase by choosing the switching angles for maximizing the torque per ampere value.

#### 6.1.3. Experimental Results

This part of the study will clarify the relationship between the acoustic noise and the peak radial force. First, the motor is driven with different advance angles at constant load. During this parametric sweep experiments, the motor acoustic noise and efficiency are measured.

The drive efficiency is obtained by the measured quantities. The input power of the SRM drive is measured from the DC link by a power analyzer. The mechanical torque and speed of the motor is read from the torque transducer. The efficiency of the drive is calculated as follows:

$$\eta \% = \frac{\frac{1}{T} \int_{0}^{T} v_{DClink}(t) . i_{DClink}(t) . dt}{T_{mech} . \omega_{mech}} x100\%$$
(112)

In Figure 131, the noise and peak radial force variation is given for 0.5 p.u. load torque. In this case, the peak radial force and as a consequent acoustic noise is dramatically reduced.

The efficiency levels obtained from the experiments are also shown together with the acoustic noise in Figure 132. In Figure 133 the peak radial force and efficiency measurements are given. Figure 134 displays the variation of torque ripple and acoustic noise. In this figure, it is observed that the acoustic noise seems to be independent of shaft torque ripple. In Figure 135, the simulated torque ripple and the measured efficiency are shown together.

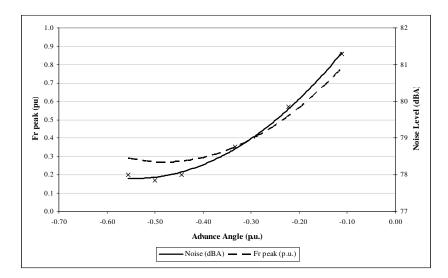


Figure 131 The measured noise level in dBA and simulated radial force versus advance angle (0.5 p.u. load torque@2000 rpm)

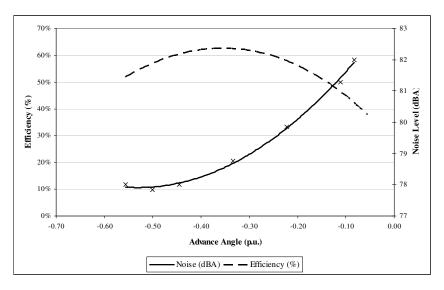


Figure 132 Measured noise level and measured efficiency for 0.5 p.u. load at 2000 rpm.

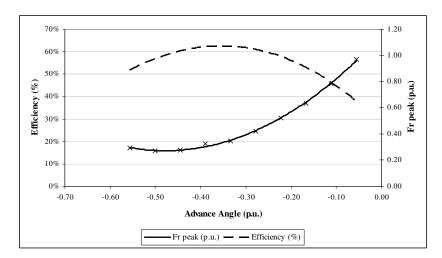


Figure 133 Measured efficiency and simulated peak radial force for 0.5 p.u. load at 2000 rpm.

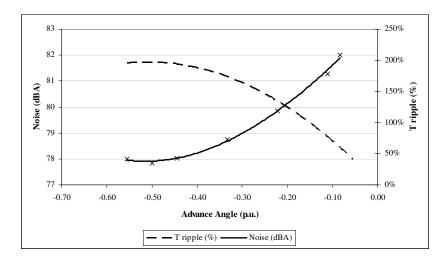


Figure 134 Measured noise level and simulated torque ripple for 0.5 p.u. load at 2000 rpm.

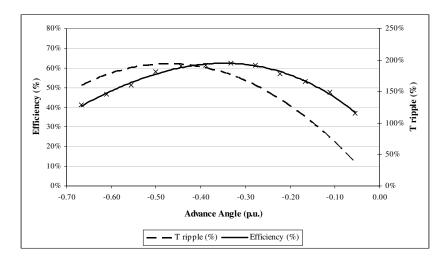


Figure 135 Measured efficiency and simulated torque ripple for 0.5 p.u. load at 2000 rpm.

In these experiments, it is observed that there is a correlation between the acoustic noise and the peak radial force level. During the design stage of the controller, the other factors effecting the acoustic noise such as stator mode resonances or other mechanical parameters are not considered and only the peak radial force minimization is dealt with.

In this stage, the relationship between the torque ripple and the acoustic noise is also ascertained. The shaft torque ripple is figured out via simulations and the results are plotted on the same graphs with the measured noise levels (Figure 134). At first glance, the shaft resonances and the sound emitted from the rotor seems to be insignificant. It must be noted that, the noise contribution of the rotor side may be more complex than it is observed in these figures. As a future study, the effect of the rotor and shaft vibrations on the total SRM noise should be analyzed in details but here, the first intuition is that, the major source of sound in an SRM is the stator back yoke vibrations. Henceforth, in this research, the radial forces will be regarded as the major source of SRM noise.

Investigation of the simulation and experimental results given in Figure 131 to Figure 135 gives important results to design a controller. The findings are summarized as follows:

- The motor must operate with the minimum peak radial force level for minimum acoustic noise (Figure 131),
- The silent and efficient operating points are different from each other (Figure 132),
- There is no direct coupling between the shaft torque ripple and the acoustic noise emission (Figure 134).

In Figure 136 to Figure 138, the simulated peak radial forces and the measured acoustic noise levels are given for 0.25, 0.75 and 1.0 p.u. load torque. These figures are also consistent with the obtained results from the 0.5 p.u. load simulation and experiments.

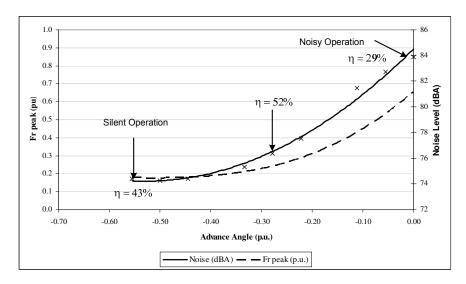


Figure 136 The measured noise and efficiency levels with the simulated radial forces. (0.25 p.u. load torque@2000 rpm)

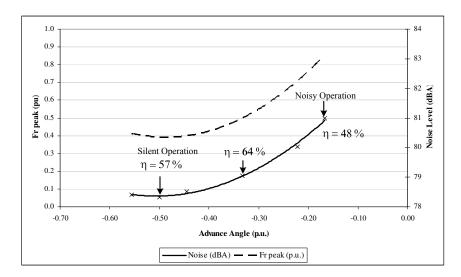


Figure 137 The measured noise and efficiency levels with the simulated radial forces. (0.75 p.u. load torque@2000 rpm)

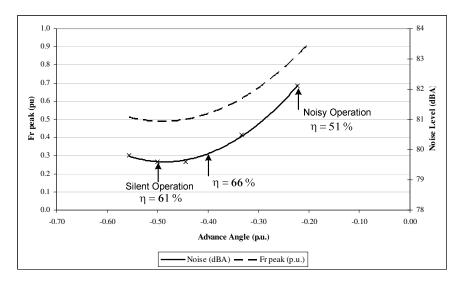


Figure 138 The measured noise and efficiency levels with the simulated radial forces. (1.00 p.u. load torque@2000 rpm)

Here, the problem and the possible way of solution is clarified. The causal links between the sound and its sources are established as basic as possible. In the next section, a controller based on this perception of the problem is presented.

#### 6.1.4. Controller Block Diagram

The primary task of an SRM controller is to define the convenient advance and conduction angles to drive the load torque at a desired speed. In a classical controller, initial conditions are defined for these two control parameters and the controller sets these parameters to fulfill the load demand. If the motor mechanical output satisfies the load requirements, the controller keeps its output unchanged. On the other hand, the simulation and experimental results presented in Figure 131 - Figure 134 show that, there are multiple operating points for the same load. A classical controller generally tends to be entrapped by the first equilibrium point which is the minimum advance angle for the given load. As it is perceived from the simulation and noise measurements, the minimum advance angle is not a good choice from the point of the acoustic noise mitigation view. A high grade controller which is capable of accomplishing a secondary object such as reducing acoustic noise or increasing efficiency should not be seized by the first solution point. The basic controllers increases or decreases the advance and conduction angles between pre-defined limits in order to supply the torque demand. With this type of controllers, the drive tends to operate with the minimum advance angle since it's the first solution point. As seen in simulation results section, minimum advance angle operation falls into the high peak radial force region so this type of operation is not suitable for multi-objective control algorithms.

In previous section, the advance and conduction angle data is generated via simulations and these findings are planned to be used in the proposed multi-objective controller. First, the obtained data will be included in the controller and then the performance and the obedience of the system to the controller will be tested through experiments.

To be able to include the simulation results in the controller, a feed-forward neural network based controller is preferred. In this type of control, a neural network is trained with the available data and then the network is used to set the control parameters to drive the load torque at a given reference speed. In the next section, a brief introduction to neurocontrollers is presented.

## 6.1.5. An Introduction to Feedforward Neural Networks

Artificial neural networks use a complicated interconnection of computing nodes for approximating the non-linear input-output relations. The main advantage of this type of controller is to use the previous experiences instead of the explicit mathematical transfer functions. Highly non-linear structure of SRM gives an inspiration about using a neuro-controller. The neuro-controller learns the system response by memorizing this previously collected data which can be regarded as an implicit transfer function of the system. The required system response can be obtained by either simulations or experiments. In our study, since a bunch of simulations have already done, simulation results are used to train the controller. Basically speaking, a neuro-controller knows the required inputs for the desired outputs by recitation and tunes the control parameters according to the output demand.

A short inspection of neuro-controller shows that feedforward neural networks (FF networks) are suitable for SRM control. They are most widely used models in many practical applications and also known as "multi-layer perceptrons."

A feedforward neural network is an artificial neural network where connections between the units do not form a directed cycle. In this network, the information moves in only one direction, forward, from the input nodes, through the hidden nodes (if any) and to the output nodes. There are no cycles or loops in the network. Figure 139 illustrates a one-hidden-layer FF network with n inputs and m outputs. The network is divided into *layers*. The *input layer* consists of just the inputs to the network. Then follows a hidden layer, which consists of any number of *neurons*, or *hidden units* placed in parallel. Each neuron performs a weighted summation of the inputs, which then passes a nonlinear activation function, also called the *neuron function*.

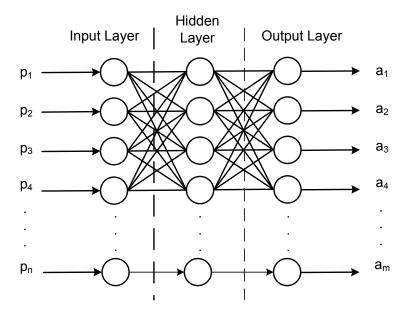


Figure 139 A multi-layer feedforward neural network with n input and m output.

#### 6.1.5.1 Neuron Model

A neuron with a single scalar input with a scalar bias b appears in Figure 140. Here, the scalar input p is transmitted through a connection that multiplies its strength by the scalar weight w. The bias is simply added to the product wp as shown by the summing junction or as shifting the function f to the left by an amount b.

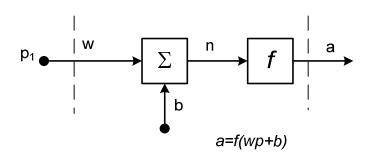


Figure 140 A simple neuron with bias.

The transfer function net input n is the sum of the weighted input wp and the bias b. The sum is the argument of the transfer function, f which is typically a *step* or a *sigmoid* function. It takes the argument n and produces the output a (Figure 141). Note that, w and b are both adjustable scalar parameters of the neuron. The main idea of neural networks is that such parameters can be adjusted so that the network exhibits some desired behavior. Thus, the network is trainable to do a particular job by adjusting the weight or bias parameters .

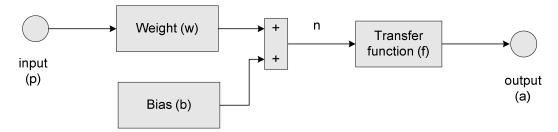


Figure 141 Input-output relation of a single layer.

The weight (w) and bias (b) vectors are obtained by training the network but the transfer function f should be selected by the user. In a multi-layer neural network, the layers are cascaded and the output of the first layer is the input of the second layer (Figure 139). Each layer transfer functions are selected independently so a neural network may involve different types of transfer functions. Here, a brief introduction is presented for the possible transfer functions.

#### 6.1.5.2 Transfer Functions

There are many alternatives for the transfer function f. The most common transfer functions are listed below. It must be noted that, regardless of the function type, all transfer functions may be symmetric or asymmetric. If the function is symmetric, the output swings between [-1, +1]. In an asymmetric function, the output can only take values in [0, +1] region.

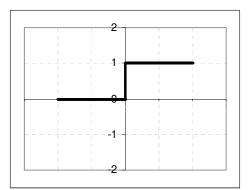


Figure 142 Hard-limit transfer function

The hard-limit transfer function shown Figure 142 limits the output of the neuron to either 0, if the net input argument n is less than 0; or 1, if n is greater than or equal to 0. This allows a neuron to make a decision or classification. It can say yes or no. This kind of neuron is often trained with the perceptron learning rule.

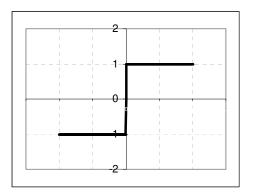


Figure 143 Symmetric hard-limit transfer function

The symmetric hard limit transfer function forces a neuron to output a 1 if its net input reaches a threshold. Otherwise it outputs -1. Like the regular hard limit function, this allows a neuron to make a decision or classification. It can say yes or no.

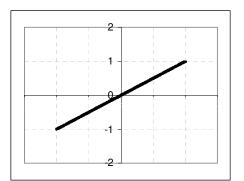


Figure 144 Pure linear transfer function

Pure linear transfers the input to output with no change or saturation limit.

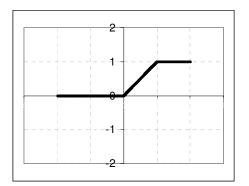


Figure 145 Linear saturation transfer function

Satlin has a linear transfer function between [0 1]. Outside this region, the output is saturated to the upper or lower limits.

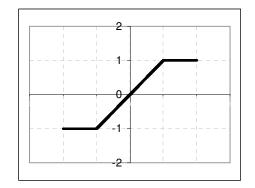


Figure 146 Symmetric linear saturation transfer function

Symmetric linear saturation function has a linear transfer function between [-1 1]. Outside this region, the output is saturated to the upper or lower limits.

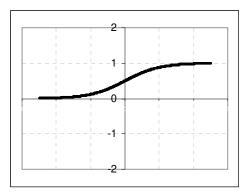


Figure 147 Log-sigmoid transfer function

The log-sigmoid transfer function shown below takes the input, which may have any value between plus and minus infinity, and squashes the output into the range 0 to 1.

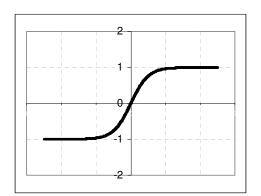


Figure 148 Tan-sigmoid transfer function

The tan-sigmoid transfer function shown below takes the input, which may have any value between plus and minus infinity, and squashes the output into the range -1 to 1.

#### 6.1.6. Proposed Neuro-controller

The controller used in this study must be capable of determining advance and conduction angles for a given load torque and speed. The problem requires a dual input - dual-output neural network.

The proposed angle controller block diagram is shown in

Figure 149. Here, the PI controller determines the conduction angle. In this structure, a speed error compensator is added to obtain a closed loop robust controller. The PI controller block takes the speed error into account while the neural network block decides the preferred advance angle for the silent operation. As seen in this block diagram, the control parameters are set independently by the neural network and PI controller. The neural network is trained by the simulation results. The training details are given in the next section.

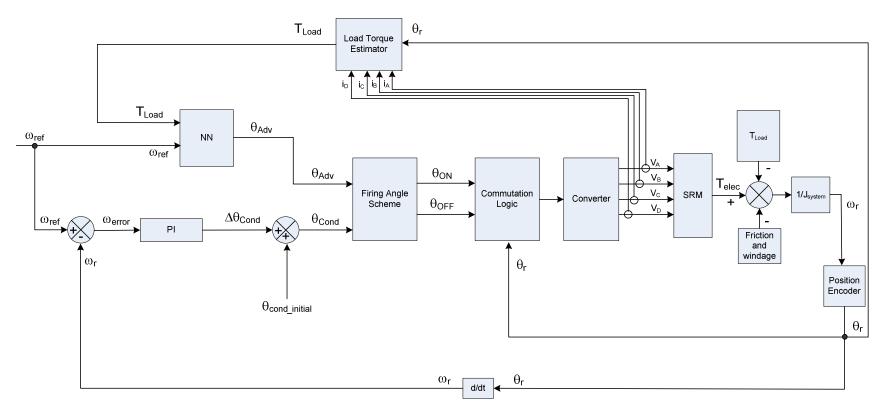


Figure 149 Proposed advance and conduction angle controller

#### 6.1.6.1 Neural Network Training

In this part of the study the neural network is trained by using the data obtained from simulations. The trained neuro-controller is designed such that the user can select the operating modes for minimizing the acoustic noise or increasing the efficiency.

The neurocontroller used in the study is built by using Matlab<sup>®</sup> neural network toolbox. By using the graphical user interface of *nntool*, the inputs and the targets are imported (Figure 150). The "New Network" creation toolbox allows the user to define the number of hidden layers and the type of the transfer functions (Figure 151). In "nntool", the network type is defined as feed-forward backpropagation and "Trainlm" is selected as training function. The adaption learning function is taken as "Learngdm" (Figure 151). In this study, a single hidden layer neural network with 20 tan-sigmoid transfer functions and a pure linear output function with bias satisfied the required advance angle calculation performance (Figure 152).

network1	network1_outputs
	Errors:
	network1_errors
	Layer Delay States
lp New Data	New Network
Export	View Delete
	elp New Data

Figure 150 Matlab nntool interface.

Network Type: Feed-forwa	rd backprop	<b>-</b>	
Input ranges:	) 2500;0.25 1]	Get from inp	•
Training function:	TRAINLM		•
Adaption learning function:	LEARNODM		•
Performance function:	MSE		٠
Number of layers:	2		
Properties for: Layer 1 Number of neurons: 20	<b>•</b>		
Transfer Function: TAN	ISIG		•

Figure 151 Matlab nntool neural network creation tool interface.

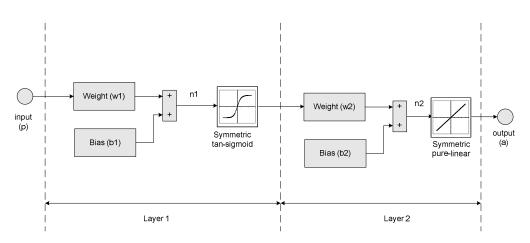


Figure 152 The neural network structure used for angle control.

By using the trained neural network, an advance angle surface is obtained for minimizing the acoustic noise (Figure 153). The trained neural network is capable of determining the advance angle for a load torque at a reference speed. For a silent operation, the advance angle is selected on this surface according to the load and speed of the motor. By doing this, the peak radial force so the motor acoustic noise will be minimized.

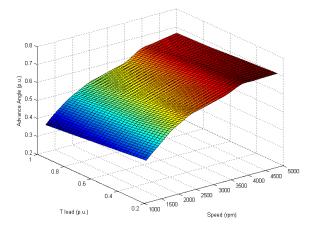


Figure 153 Minimum noise level surface

The second surface for the advance angle is also obtained by using the maximum torque per ampere points of the test motor mentioned in Chapter 4 to increase the SRM efficiency (Figure 154). This advance angle surface is obtained by the same training method given above for the minimum acoustic noise. This surface allows the user to maximize the average torque per ampere ratio of the motor in order to increase the SRM efficiency. The surfaces given in Figure 153 and Figure 154 are interchangeable. By switching between these two advance angle surfaces, the operating mode changes from silent to more efficient mode or vice versa. The relevant conduction angles are calculated by the PI controller for each operation mode. These surfaces are used to determine the advance angle by the NN block given in the controller block diagram (Figure 149).

The performance of the proposed controller for both reducing the acoustic noise and increasing the efficiency will be given in the next chapter.

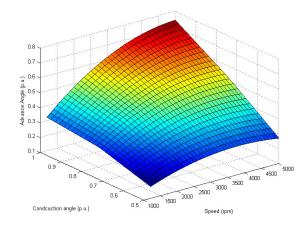


Figure 154 Advance angle surface for efficient operation.

# **CHAPTER 7**

# ACOUSTIC NOISE MEASUREMENTS AND CONCLUSIONS

In this chapter, after an overview of human perception of acoustic noise, the noise measurement results of the test motor are presented. The noise measurements are made between 1200 and 4000 rpm to see the effects of the noise mitigation performance of the controller designed in Chapter 6 is tested and evaluated.

# 7.1. Introduction to Acoustic Noise and its Measurement

Acoustic noise is the sound which is undesired by the recipient. Due to the natural limitations, perception of human ear is limited to 20 Hz and 20 kHz (Figure 155).

The sound heard everyday is mostly composed of different sources so the frequency components instead of a pure sound of one frequency. On the other hand, the difference between the sound and noise is not clear. Due to this combined and relative evaluation of sound, some definitions must be made to measure the acoustic noise.

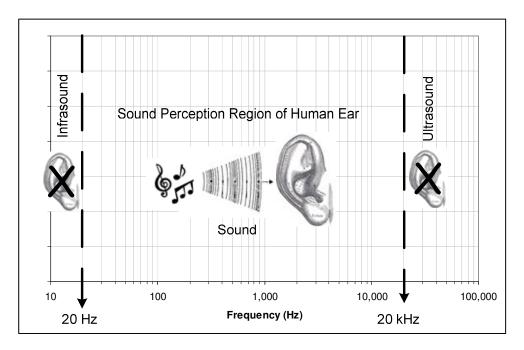


Figure 155 Audible frequency region from the point of the human ear perception

# 7.2. Quantification of Acoustic Noise

Measuring and quantifying methods of acoustic noise must be well defined to get rid of the subjective classification of noise. Generally, sound term is used for the quantification instead of noise because the decision of which frequencies are sound and which are noise is left to the recipient regardless of its intensity.

#### 7.2.1. Sound Power Level (SWL or L<sub>w</sub>)

The sound power level L<sub>w</sub> from a source is defined as follows:

$$L_{w} = 10.\log\left(\frac{W}{W_{ref}}\right) dB$$
(113)

Here, W is the average sound power from the source and  $W_{ref}$  is taken as 1 pW.

$$W_{ref} = 10^{-12} W$$

$$W_{ref} = 1 pW$$
(114)

The sound power level may also be measured in dBW which stands for decibel with the suffix for watts. Decibels are dimensionless.

Sound Source	Sound Power	Sound Power Level
souna source	P, [W]	$SWL or L_w, dB$
Saturn Rocket	30,000,000 W	195
Airliner (four propeller)	10,000	160
Siren	1,000	150
Heavy Truck Engine	100 W	140
Jackhammer	1 W	120
Excavator	0,3 W	115
Chain Saw, Truck Horn	0,1 W (10 <sup>-1</sup> )	110
Loud Record Play	0,01 W (10 <sup>-2</sup> )	100
Voice (Shouting)	0,001 W (10 <sup>-3</sup> )	90
Voice (Conversation)	0,00001 W (10 <sup>-5</sup> )	70
Whisper	0,0000001 W (10 <sup>-7</sup> )	50

Table 5 Power and power level from different sources

From Table 5, it is observed that the amount of acoustic power of the notable sound levels are very low so can be neglected in machine loss calculations.

### 7.2.2. Sound Pressure (SPL or L<sub>p</sub>)

The sound is a wave which carries an energy and applies a pressure to the surface which is exposed to it. If the sound pressure is known, the sound pressure level is defined as follows:

$$L_p = 20.\log\left(\frac{p}{p_{ref}}\right) dB \tag{115}$$

Here,  $P_{ref}$  is the reference sound pressure which is taken as 20 µPa as the normal threshold of hearing which is approximately equal to the RMS sound pressure of a pure tone at 1 kHz.

$$p_{ref} = 20\,\mu Pa \tag{116}$$

The sound pressure level  $L_p$  is the related with the sound power level  $L_w$  by the following equation:

$$L_w = 10.\log A + \overline{L}_p \tag{117}$$

Here, A is the whole area enclosing the sound generating object in  $m^2$ .

#### 7.2.3. Sound Intensity (I)

The sound power produced from the source goes to everywhere. Since the geometrical shape that has all points equal distance away from a source is a sphere, the loudness depends on the ratio of the area of the sound collector to the total area of the sphere surrounding the sound source. This motivates the introduction of another physical quantity associated with sound waves: intensity. The intensity of a sound wave is the amount of power in the wave per unit area and has units of  $W/m^2$ . The intensity of a sound wave depends on how far the recipient is from the source. Sound intensity *I* is defined as the average sound power passing through a unit area perpendicular to the specified direction at that point so it is just the ratio of the sound power to the surface area of a sphere of radius *r*, where *r* is the distance we are from the sound source.

Sound intensity = 
$$\frac{\text{Sound Power}}{4.\pi r^2}$$
 (118)

In this study the microphones are placed 0.5 m far from the central axis of SRM so r is taken as 0.5 m.

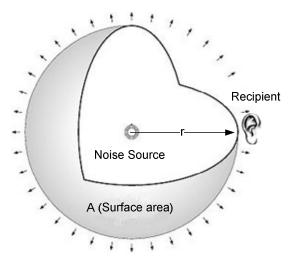


Figure 156 Sound power passing through the spherical surface from a distance of r.

The sound intensity I can be calculated by the following formula:

$$I = \frac{p^2}{\rho c} W m^{-2} \tag{119}$$

Here p is the RMS sound pressure,  $\rho$  is the constant equilibrium density of the medium and *c* is the velocity of sound in the medium. The product  $\rho$ .c is defined as the characteristic impedance of the medium. At 20<sup>0</sup> C and standard atmospheric pressure the characteristic impedance of air is  $\rho$ .c = 415 kgm<sup>-2</sup>s<sup>-1</sup>.

Sound will radiate spherically in free field so the sound intensity will decrease with the square of the distance from the source. The surface area of a sphere is given by (120):

$$A_{sphere} = 4.\pi r^2 \tag{120}$$

Here r is the radius of the sphere. Defining two sphere with radius r and R the relationship between the sound intensity is given by

$$\frac{I_r}{I_R} = \frac{R^2}{r^2} \tag{121}$$

By using this equation, to calculate the sound pressure level difference between two distances r and R is possible. It is obtained that if the distance is doubled, the sound pressure level decreases by 6 dB.

$$L_{p,r} - L_{p,R} = 10.\log \frac{I_r}{I_R} = 10.\log \frac{R^2}{r^2} = 20.\log \frac{R}{r} = 20.\log \frac{2.r}{r} \approx 6dB$$
 (122)

With the reference intensity defined as  $I_0 = 10^{-12}$  W/m<sup>2</sup>, the *sound intensity level* can be defined as follows:

$$L_I = 10.\log\left(\frac{I}{I_0}\right) \tag{123}$$

Since the intensity in a sound wave is proportional to the square of the amplitude of the sound wave, (123) is identical to (115).

$$\left(\frac{p^2}{p_{ref}^2}\right) = \left(\frac{I}{I_0}\right)$$

$$10.\log\left(\frac{p^2}{p_{ref}^2}\right) dB = 10.\log\left(\frac{I}{I_0}\right)$$

$$L_p = L_I$$
(124)

### 7.2.4. Add, subtract and average sound pressure:

Sound levels can also be added, subtracted or averaged. For instance it is sometimes important to subtract background noise or average different measured sound levels.

### **Adding**

The following equation can be used for adding n individual sound levels:

$$L_{p,add} = 10.\log\left(\sum_{i=1}^{n} 10^{0.1L_{pi}}\right) dB$$
(125)

### **Subtracting**

The following equation can be used for subtracting the background sound pressure level  $L_{pB}$  from the total measured sound pressure  $L_p$ :

$$L_{p,sub} = 10.\log(10^{0.1Lp} - 10^{0.1LpB})dB$$
(126)

#### Averaging

If there are n different sound levels to be averaged, the following equation can be used:

$$\overline{L_p} = 10.\log\left(\frac{1}{n}\sum_{i=1}^{n} 10^{0.1L_{pi}}\right) dB$$
(127)

#### 7.2.5. Octave Band Analysis

To identify frequency components of a sound, there is octave band analysis in which frequencies are segmented into proportionate widths (octave bands) and analyzed. The sound pressure level of a single octave band is called the *octave band level*, while that analyzed for 1/3 of the octave band is called a *1/3 octave band level*. The frequency band in the octave band and 1/3 octave band is expressed as the center frequency of that band. The relation between the upper and lower cutoff frequencies are defined as follows:

$$f_2 = 2.f_1$$
, (For 1 octave band)  
 $f_2 = \sqrt[3]{2.f_1}$ , (For 1/3 octave band) (128)

Using  $f_1$  and  $f_2$  as the upper and lower end frequencies of the band, the center frequency  $f_c$  is as follows:

$$f_c = \sqrt{f_1 \cdot f_2} \tag{129}$$

Table 7 lists the center frequency of octave bands and the frequency that cuts off the upper and lower ends of those bands. As the octave band increases by one, the frequency band width there contained doubles (because of proportioned widths, Table 7). For this reason, in the octave analysis of white noise, band level increases by 3 dB with every octave. Here, a sound with a spectrum pressure level in which all spectral band levels are equal is called a pink noise.

Center	Cutoff Frequency	Center Frequency
Frequency (Hz)	( <i>Hz</i> )	(Hz)
(112)	22.4	31.5
63	45	51.5
05	90	125
250	180	123
230	355	500
1000	710	500
1000	1400	2000
4000	2800	2000
+000	5600	8000
	11200	0000

Table 6 Center and cutoff frequencies of octave bands.

Center Frequency (Hz)	Cutoff Frequency (Hz)	Center Frequency (Hz)
20	14 18	- 16
20	22.4 28	- 25
31.5	35.5	- 40
50	<u>45</u> 56	
80	71	- 63
125	90 112	- 100
125	140 180	- 160
200	224	- 250
315	280 355	- 400
500	450 560	400
800	710	- 630
1050	<u>900</u> 1120	- 1000
1250	1400 1800	- 1600
2000	2240	- 2500
3150	2800 3550	
5000	4500	4000
8000	5600 7100	- 6300
0000	9000 11200	- 10000
12500	11200	

Table 7 Center and cutoff frequencies of 1/3 octave bands

From Table 6 and Table 7, it is seen that the resolution of the 1/3 octave band is higher than the 1 octave band.

#### 7.2.6. Sound Perception of Human Ear

,

As seen in Figure 155, human ear can perceive only the frequencies between 20 and 20.000 Hz. Besides, between these limits, the perception of ear is not uniform or linear. If human ear have had a uniform characteristics of perception, the sound level could be used directly but because of the human ear varies in sensitivity in a complex way that depends on frequency and level, some weighting scales have been developed to simulate or understand the various sensitivities. These weighting scales (or functions) are known as A, B, C or D weightings. The most commonly used weighting scale is the A-weighting.

The A weighting can be described as a function of the frequency by the following equation:

$$G_{A}(f) = 2.0 + 20.\log\left(\frac{12200^{2} \cdot f^{4}}{\left(f^{2} + 20.6^{2}\right)\left(f^{2} + 12200^{2}\right)\sqrt{\left(f^{2} + 107.7^{2}\right)\left(f^{2} + 737.9^{2}\right)}}\right)$$
(130)

Also this function characteristics can be implemented by the filter in the s domain by the transfer function given as follows:

$$G_A(s) = \frac{7.397 \times 10^9 \cdot s^4}{(s+129.4)^2 \cdot (s+676.7)(s+4636)(s+76655)^2}$$
(131)

 $G_A(f_j)$  is calculated for the one-third-octave frequencies and used to obtain the A-weighting values  $A_j$  by the following equation:

$$A_{j} = 10.\log\left[G_{A}\left(f_{j}\right)\right] \tag{132}$$

Here,  $f_j$  is the j<sup>th</sup> center frequency of the one-third-octave band. The results are given in Table 8, Figure 157 and Figure 158.

j	One-third-octave	Amplitude of the	A-weighting
	midband	frequency	values
	Frequencies	response	(A <sub>j</sub> )
	$(\mathbf{f_j})$	$(\mathbf{G}_{\mathbf{A}}(\mathbf{f}_{\mathbf{j}}))$	
	Hz		dB
1	20	0.000009	-50.4
2	25	0.000033	-44.8
3	31.5	0.000112	-39.5
4	40	0.000352	-34.5
5	50	0.000939	-30.3
6	63	0.002388	-26.2
7	80	0.005761	-22.4
8	100	0.012182	-19.1
9	125	0.024055	-16.2
10	160	0.047391	-13.2
11	200	0.082298	-10.8
12	250	0.135700	-8.7
13	315	0.216600	-6.6
14	400	0.333150	-4.8
15	500	0.473400	-3.2
16	630	0.644400	-1.9
17	800	0.832780	-0.8
18	1,000	1.000000	0.0
19	1,250	1.141800	+0.6
20	1,600	1.256900	+1.0
21	2,000	1.318700	+1.2
22	2,500	1.339900	+1.3
23	3,150	1.318600	+1.2
24	4,000	1.248300	+1.0
25	5,000	1.136100	+0.6
26	6,300	0.973680	-0.1
27	8,000	0.767870	-1.1
28	10,000	0.563410	-2.5
29	12,500	0.375480	-4.3
30	16,000	0.213490	-6.7
31	20,000	0.116230	-9.3

Table 8 Amplitude response of A-weighting function and A-weighting values,  $A_{j}$ .

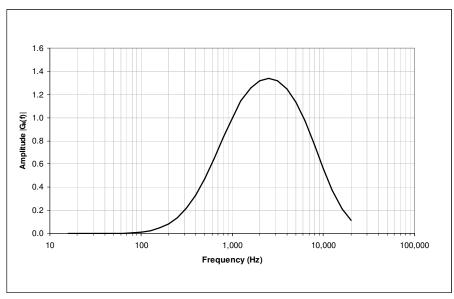


Figure 157 Amplitude response of A-weighting network, G<sub>A</sub>(f<sub>j</sub>).

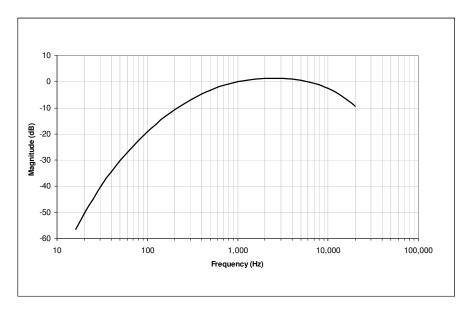


Figure 158 Magnitude response of A-weighting network in decibels.

As it is seen in both Table 8 and Figure 158, the perception of human ear is more sensitive to noise in the band of 1,000 and 5,000 Hz. The noise heard in this range is amplified by the natural response of human hearing mechanism while the others are suppressed.

# 7.2.7. Calculation of A-Weighted Sound Power Level from one-third-octaveband sound levels

The A-weighted sound power level is calculated from the following equation using the measurement levels that are included in the frequency range of interest:

$$L_{pA} = 10.\log\left(\sum_{j} 10^{0.1(L_{pj} + A_j)}\right) dB$$
(133)

 $L_{pj}$  is the frequency band pressure level measured in the j<sup>th</sup> one-third-octave band (in dB).

*j* is the midband frequency number of the one-third-octave band (Table 8).

 $A_j$  is the A-weighting value for the j<sup>th</sup> midband frequency (Table 8).

In this study, since the noise source emits strong discrete frequency components, the calculation is performed using one-third-octave band A-weighting values as it is recommended in [41].

In the projection of A-weighting scale, Figure 155 can be updated as seen in Figure 159 for taking the human perception of sound into account.

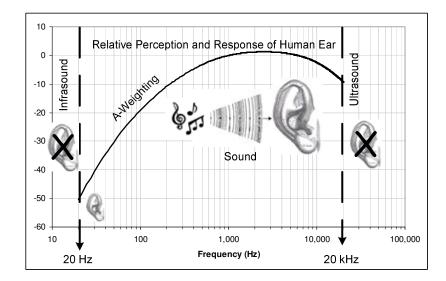


Figure 159 The sound region with taking the human perception of sound into account by A-weighting

### 7.3. Noise Measurements of the Test Motor

For the noise measurements of the SRM drive, the test bed seen in Figure 160 is taken to the Arçelik A.Ş. dish washer factory which has an anechoic test room for sound measurements. The aim of these measurements is to reveal the effects of the developed controller on the SRM acoustic noise. The experiments are made at 1200, 2000, 2500, 3500 and 4000 rpms. Although the test motor is designed to operate up to 15.000 rpm, the test equipments such as position encoder and the torque transducer is not suitable for high speed experiments. In each speed level, the drive is controlled by both conventional PI controller and the developed neuro-controller. The PI controller intrinsically tends to operate with minimum advance angle since it does not increase the advance or conduction angles if the reference speed command is carried out. On the other hand, the developed noise minimization algorithm of the new controller tries to operate the drive with minimum peak radial force or maximum torque per ampere value depending on the selection of the control mode. Both the minimum peak radial force and the

maximum torque per ampere operating points are different from the minimum advance angle point. The minimum peak radial force operating points falls into the largest advance angle advance angle point while the maximum torque per ampere resides between the maximum and minimum advance angles as seen in Figure 131 and Figure 132. As a result, the PI controller drives the load with minimum advance angle while the proposed controller tends to operate with maximum advance angle. Both controllers determine the proper conduction angles to make the SRM produced the required load torque.

Since the SRM should be loaded during acoustic noise measurements, the mechanical load must be coupled to the test motor (Figure 160). In this configuration, the noise emitted from the mechanical load must be suppressed as much as possible in order to minimize the noise contribution stemming from the induction motor. For this purpose, a custom made cabinet is used to attenuate the load noise (Figure 161).



Figure 160 Test setup used for loading SRM during sound measurements.

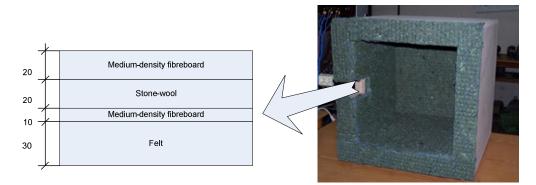


Figure 161 The cabinet for insulating the load noise. (Dimensions are given in millimeters).

The cabinet is composed of four layers. The outermost and the third layer are made of medium-density fibreboard (MDF) with a stone-wool slab between them. The innermost layer is made of felt in order to prevent the echo.

In Figure 160 and Figure 162, the test setup is seen in the anechoic test room with and without noise attenuation cabinet.



Figure 162 SRM test bed with noise attenuation cabinet

The total sound pressure level is obtained by four microphones. The microphone settlement and their distances from the SRM central axis is shown in Figure 163. As it is mentioned before in (118), the sound intensity I is defined as the average sound power passing through a unit area perpendicular to the specified direction at that point so it is just the ratio of the sound power to the surface area of a sphere of radius r. In this experiment the microphones are placed in equal distances to the central axis of SRM in order to represent an imaginary sphere surface.

The experiment procedure is given in Figure 164. To observe the noise minimization performance of the developed controller, sound measurements are made with and without controller under the same speed and load conditions. To compare the noise levels of the designed neuro-controller, SRM noise under PI control is also observed. The mechanical load torque is adjusted by the analog input of the induction machine drive and its error is observed from the torque transducer analog output to update the reference input.

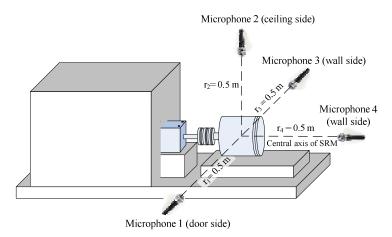


Figure 163 Acoustic noise measurement setup and the microphone distances from the SRM central axis.

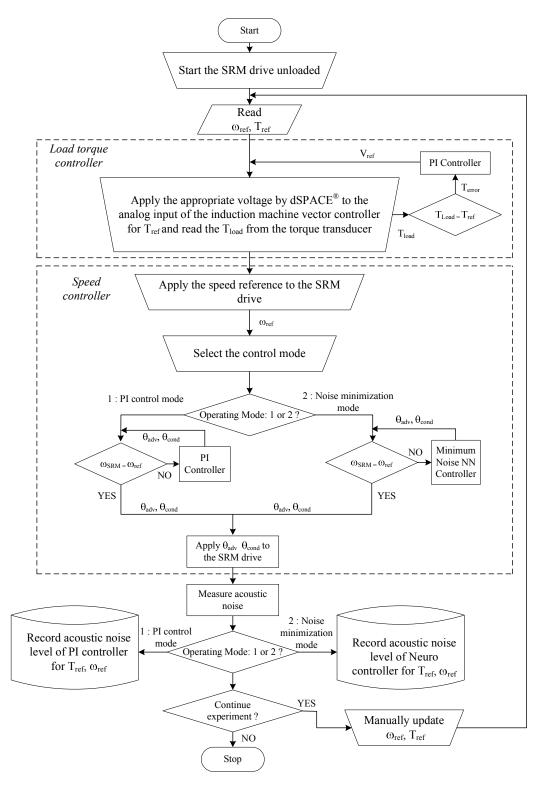


Figure 164 SRM acoustic noise measurement procedure.

The noise levels are obtained in one-third octave spectrum for each experiment. From this spectrum analysis, the dominant harmonics at the excitation frequencies are observed. At each speed, the excitation frequency changes. For example at 2000 rpm, the excitation frequency can be calculated as follows:

$$f_{excitation} = 2000 \, rpm. \frac{1 \, \text{min}}{60 \, \text{sec}}.24 \, ppr = 800 \, Hz$$
 (134)

In Figure 165 to Figure 168, one-third octave band spectrums are given for different levels of load at 2000 rpm. It is observed from these figures that, at 800 Hz a dominant harmonic exists. Near this main switching frequency, adjacent harmonic amplitudes are also high at 630 and 1000 Hz. This may be because of the stator body resonances coincide with the switching frequency at these points. For a complete analysis of the noise spectrum, the stator body mode resonances should be investigated together with the spectrum given in Figure 165 to Figure 168. The resonance mode frequencies are beyond the scope of this research. Here, the aim is to reduce the total sound pressure of the motor so the frequency spectrum of the noise is not considered as a key point of the study. Instead, the total sound pressure levels are investigated to observe the mitigation of the total acoustic noise.

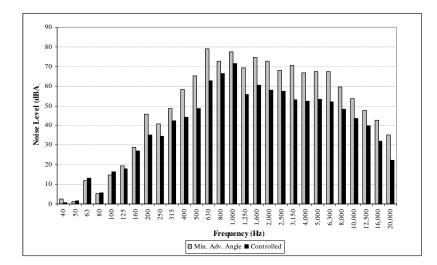


Figure 165 One-third octave spectrum of the acoustic noise under PI and noise controlled modes ( $T_{load} = 0.25$  p.u, n=2000 rpm).

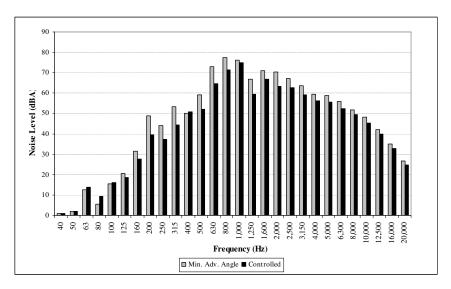


Figure 166 One-third octave spectrum of the acoustic noise under PI and noise controlled modes ( $T_{load} = 0.50$  p.u, n=2000 rpm).

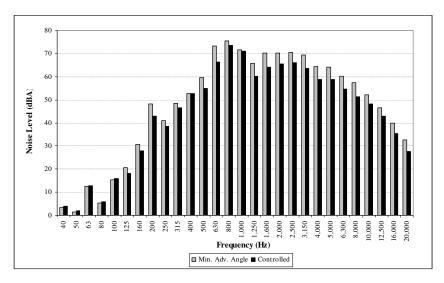


Figure 167 One-third octave spectrum of the acoustic noise under PI and noise controlled modes ( $T_{load} = 0.75$  p.u, n=2000 rpm).

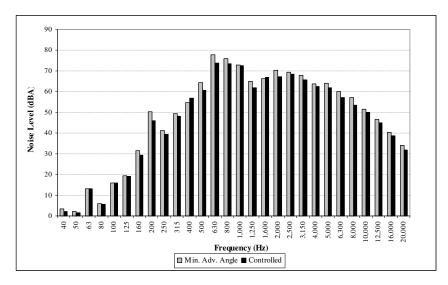


Figure 168 One-third octave spectrum of the acoustic noise under PI and noise controlled modes ( $T_{load} = 1 \text{ p.u, n=}2000 \text{ rpm}$ ).

The noise levels under PI and noise controlled modes are given in Figure 169 to Figure 172.

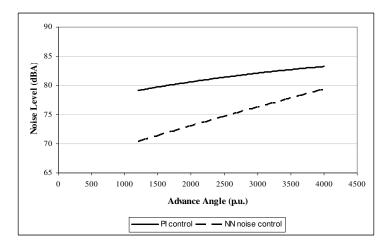


Figure 169 Noise levels under PI and noise controlled modes at 0.25 pu load.

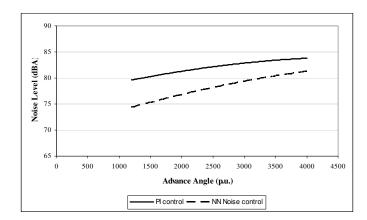


Figure 170 Noise levels under PI and noise controlled modes at 0.5 pu load.

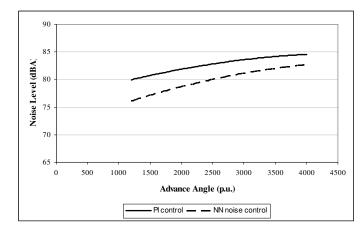


Figure 171 Noise levels under PI and noise controlled modes at 0.75 pu load.

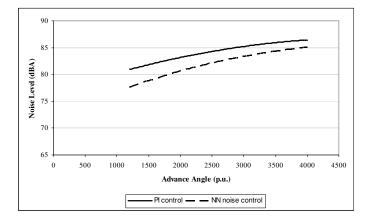


Figure 172 Noise levels under PI and noise controlled modes at 1.0 pu load.

In Figure 173, the amount of noise reduction is shown for different load levels. It is also observed from Figure 173 that the noise mitigation performance of the controller decreases with the increasing load and speed. This is an expected result since the radial force mitigation is smaller at high load levels as investigated in Chapter 6 (Figure 118 - Figure 120) Besides, near the maximum load torque, the control parameter possibilities become less. It is also noteworthy that the minimum advance angle is a trap for the conventional advance angle controllers as the drive goes on to operate at this point if the speed and torque command is satisfactorily carried out.

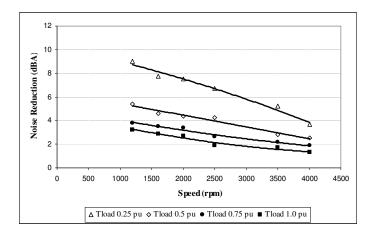


Figure 173 Noise reduction at different speed.

The measured drive efficiencies at 2000 rpm for different load levels are given in Figure 174. Here, it is seen that the proper selection of advance and conduction angles drastically changes the drive efficiency. In this study, to increase the SRM efficiency only the average torque per ampere value is tried to be maximized. It should be noted that this approach increases the drive efficiency but does not guarantee the most efficient operation since it doesn't take the core and copper losses into account which are not constant at different operating points. Although the efficiency approach used here needs some more investigations and has some deficiencies, it is observed from Figure 174 that the drive efficiency is increased

by maximizing the torque per ampere values of the SRM. It is also noteworthy that to operate the motor with minimum acoustic noise decreases the motor efficiency which may be considered as a sacrifice of the silent operation.

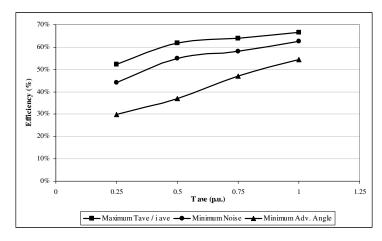


Figure 174 The efficiency level versus load torque for different modes of operation at 2000 rpm.

### 7.4. Conclusions

In this study, the key factors of SRM acoustic noise are investigated. The following summarizes the stages of this research:

- 1. As a starting point, the shaft torque ripple is considered as a source of acoustic noise and it is tried to be minimized,
- For this purpose, a sliding mode instantaneous torque controller is designed and implemented to minimize the shaft torque ripple by using only the phase voltage as the control parameter. In this controller, the switching angles are kept constant,
- 3. The deficiency of the developed sliding mode controller is the limited speed range because of having single control parameter ( $V_{phase}$ ) and keeping the switching angles ( $\theta_{adv}$ ,  $\theta_{cond}$ ) constant. The speed range should

be extended by including the advance and conduction angles as the control parameters,

- 4. The developed sliding mode controller reduced the acoustic noise but a careful investigation of the results indicated that the main reason of the noise mitigation is the reduction of the peak radial forces. With this understanding of the problem, it is deduced that the peak level of the radial forces should be minimized in order to reduce the acoustic noise emission,
- 5. The relation between the radial force and acoustic noise level is revealed via parametric sweep simulations and acoustic noise measurements. First the torque ripple levels are obtained via simulations. Then the acoustic measurements are made and the torque ripple levels are compared with the measured acoustic noise levels. It is deduced from this investigation that the torque ripple is not a major source of acoustic noise in SR motors (Figure 134). After this, the peak radial force levels are obtained via simulations and compared with the measured acoustic noise levels. As a result, a great consistency between the simulated peak radial force and the measured acoustic noise level is observed (Figure 131). This study indicated that the key factor of SR motor is the peak level of the radial forces,
- 6. Although the developed advance angle control is application dedicated, it helped to see whether the control satisfies the expectations or not,
- 7. The noise minimization performance of the new control method is experimentally tested and it is observed that with this controller, the acoustic noise is mitigated while the drive efficiency increases with the maximum torque per ampere operation (Figure 174). It should be noted that the feed-forward neuro-controller determines the advance angle for the minimum noise or maximum torque per ampere operation while the PI controller uses the speed feedback for obtaining the proper conduction angle for the selected operation mode. By using this closed loop

conduction angle controller, the possible deficiencies of the feed-forward controllers are avoided,

- 8. It is observed that to operate the SRM under maximum advance angle will decrease the noise since this kind of operation minimizes the peak radial forces (Figure 131),
- Minimization of torque ripple is important for the loads which are sensitive to the tangential shaft vibrations but its effect on the SRM acoustic noise is unimportant.
- 10. As a future study the developed controller should be modified in order to get rid of its application dependency. It is also desirable to investigate the behavior of the motor under dynamic conditions and develop a controller which can handle this operating mode,
- 11. In this study, the switching angle controller design and testing are made in a narrow speed range (1200 – 4000 rpm) due to the operating limits of the test equipment such as torque transducer, position encoder, mounting tolerances, etc. For the completeness of the study, it must be checked within the operating limits of the motor up to 15.000 rpm with a proper experiment setup.

### REFERENCES

- T. J. E. Miller, "Switched reluctance motor drives," *Intertec Communications Inc., PCIM Series in Power Electronics and Intelligent Motion*, Ventura, California, USA, 1988, pp.34-35.
- [2] J. M. Stephenson, J. Corda, "Computation of torque and current in doublysalient reluctance motors from nonlinear magnetization data," *IEE Proc., Part B, Electric Power Applicat.*, Vol. 126, No. 5, pp.393-396, May 1979.
- [3] P. J. Lawrenson, J. M. Stephenson, P. T. Blenkinsop, J. Corda, N. N. Fulton "Variable-Speed Switched Reluctance Motors" *Proc. IEE*, Vol.127, No.4, pp.253-265, July 1980.
- [4] D. A. Torrey, J. H. Lang, "Modelling a nonlinear variable-reluctance drive," *IEE Proc. B*, vol.137, no.5, pp.314-326, Sep.1990.
- [5] D. W. J. Pulle, "New data base for switched reluctance drive simulation," *IEE Proc. B*, vol. 138, no.6, pp.331-337, Nov. 1991.
- [6] T. J. E. Miller, M. McGilp, "Nonlinear theory of the switched reluctance motor for rapid computer-aided design," *IEE*, *Proc. B*, vol. 137, no.6, pp.337-347, Nov. 1990.
- [7] F. Soares, P. J. C. Branco, "Simulation of a 6/4 switched reluctance motor based on Matlab/Simulink environment," *IEEE Trans. Aerosp. Electron. Syst.*, vol.37, no.3, pp.989-1009, July 2001.
- [8] G. G. Lopez, J. Walters, K. Rajashekara, "Switched reluctance machine control strategies for automotive applications," *SAE Technical Paper Series*, Energix Center, Delphi Automotive Systems, 2001-01-0955.
- [9] E. Bizkevelci, K. Leblebicioğlu, H. B. Ertan, "A sliding mode controller to minimize SRM torque ripple and noise," in *Proc. IEEE Internat. Symp. on Ind. Electron.*, 2004, France, pp.1333–1338.

- [10] E. Bizkevelci, K. Leblebicioğlu, H. B. Ertan, "A control strategy for noise reduction in switched reluctance motors," in *Proc. SAEM*, 2006, Macedonia.
- [11] E. Bizkevelci, H. B. Ertan, K. Leblebicioğlu; "A Sliding-Mode Control Strategy for Noise Reduction in Switched Reluctance Motors", *IEEE Trans. Ind. Electron.*, to be published.
- [12] M. Ilic-Spong, T. J. E. Miller, S. R. MacMinn, and J. S. Thorp, "Instantaneous torque control of electric motor drives," *IEEE Trans. Power Electron.*, vol. 2, pp. 55–61, Jan. 1987.
- [13] M. Ilic-Spong, R. Marino, S. M. Peresada, D. G. Taylor, "Feedback linearizing control of switched reluctance motors," *IEEE Trans. Autom. Control*, vol.AC-32, no.5, 1987, pp. 371-379.
- [14] D. G. Taylor, "An experimental study on composite control of switched reluctance motors," *IEEE Control Syst. Mag.*, 1991, 11, (2) pp. 31-36.
- [15] D. S. Schramm, B. W. Williams, T. C. Green, "Optimum Commutation-Current Profile on Torque Linearization of SRM," *Proc. 1992, ICEM'92*, Vol.2, pp.484.
- [16] R. S. Wallace, D. G. Taylor, "A balanced commutator for SRM to reduce torque ripple," *IEEE Trans. Power Electronics*, vol.7, pp.617-626, Oct. 1992.
- [17] R. C. Kavanagh, J. M. D. Murphy, M. G. Egan, "Torque ripple minimization in SRM drives using self learning techniques" *Proc. IEEE IECON*, pp.289-294, 1991.
- [18] F. Filicori, G. C. L. Bianco, A. Tonielli, "Modeling and control strategies for a VR direct-drive motor," *IEEE Trans. Ind. Electron.*, vol. 40, pp. 105-115, 1993.
- [19] G. S. Buja, R. Menis, M. I. Valla, "Variable structure control of an SRM drive," *IEEE Trans. Ind. Electron.*, Vol. 40, No.1, pp. 56-63, Feb. 1993.
- [20] I. Husain and M. Ehsani, "Torque ripple minimization in switched reluctance motor drives by PWM current control," *IEEE Trans. Power Electron*, vol. 11, pp. 83–88, Jan. 1996.

- [21] P. C. Kjaer, J. J. Gribble, T. J. E. Miller, "High-Grade Control of SRM" *IEEE- IAS Annual Meeting*, pp. 92-100, 1996.
- [22] P. G. Barrass, B. C. Mecrow, "Flux and torque control of switched reluctance machines," *IEE Proc. Electr. Power Appl.*, Vol. 145, No.6, Nov. 1998, pp. 519-527.
- [23] K. Russa, I. Husain, M. Elbuluk, "Torque-ripple minimization in SRM over a wide speed range," *IEEE Trans. Ind. Applicat.*, vol.34, no.5, pp.1105-1112, Sep/Oct. 1998.
- [24] S. Mir, M. Elbuluk, I. Husain, "Torque-ripple minimization in SRM using adaptive fuzzy control," *IEEE Trans. Ind. Applicat.*, vol.35, no.2, pp. 461-468, March/April 1999.
- [25] K. Russa, I. Husain, M. Elbuluk, "A Self-Tuning Controller for SRM" IEEE Trans. Power Electron., vol. 15, pp. 545-552, 2000.
- [26] A. M. Osama, H. A. A. Fattah, A. M. Sakr, "Variable structure flux linkage controller for torque ripple minimization in switched reluctance motors," *American Control Conf., Proc. of the 2002*, vol.4, pp.3105–3110, 2002.
- [27] F. Şahin, H. B. Ertan, K. Leblebicioğlu, "Optimum geometry for torque ripple minimization of switched reluctance motors," *IEEE Trans. Energy Convers.*, vol.15, issue.1, pp.30-39, March 2000.
- [28] D. E. Cameron, J. H. Lang, S. D. Umans, "The origin of acoustic noise in doubly salient variable-reluctance motors," *IEEE Trans. Ind. Applicat.*, vol.28, no.6, pp.1250-1255, Nov/Dec 1992.
- [29] C. Y. Wu, C. Pollock, "Analysis and reduction of vibration and acoustic noise in the switched reluctance drive," *IEEE Trans. Ind. Applicat.*, vol.31, no.1, pp.91-98, Jan-Feb. 1995.
- [30] C. Pollock, C. Y. Wu, "Acoustic noise cancellation techniques for switched reluctance drives," *IEEE Trans. Ind. Applicat.*, vol.33, no.2, pp.477-484, March/April 1997.
- [31] A. Michaelides, C. Pollock, "Reduction of noise and vibration in SRM: New aspects," *IEEE Ind. Applicat. Conf.*, 31<sup>st</sup> IAS Annual Meeting, vol.2, pp.771-778, Oct. 1996.

- [32] R. S. Colby, F. M. Mottier, T. J. E. Miller, "Vibration modes and acoustic noise in a four-phase switched reluctance motor," *IEEE Trans. Ind. Applicat.*, vol.32, no.6, pp.1357-1363, Nov. 1996.
- [33] B. Fahimi, G. Suresh, K. M. Rahman, M. Ehsani, "Mitigation of acoustic noise and vibration in SRM drive using neural network based current profiling," *IEEE Ind. Applicat. Conf.*, 33<sup>rd</sup> IAS Annual Meeting, vol.1, pp.715-722, Oct. 1998.
- [34] P. O. Rasmussen, F. Blaabjerg, J. K. Pedersen, P. C. Kjaer, T. J. E. Miller, "Acoustic noise simulation for switched reluctance motors with audible output," *Proc. of EPE '99*, paper no.519, pp.1-13, Lausanne, 1999.
- [35] R. Krishnan, "Switched reluctance motor drives: Modeling, simulation, analysis, design, and applications", *CRC Press*, Industrial Electronics Series, 2001.
- [36] K. A. Kasper, J. O. Fiedler, D. Schmitz, R. W. Doncker, "Noise reduction control strategies for switched reluctance drives," in *Proc. IEEE Vehicle Power* and *Propulsion Conf.*, Sept. 2006, pp.1-6.
- [37] E. Bizkevelci, H. B. Ertan, K. Leblebicioğlu, "Effects of control parameters on SRM performance: A parametric search," in *Proc. ACEMP*, 2007, Turkey, pp.276–281.
- [38] E. Bizkevelci, H. B. Ertan, K. Leblebicioğlu; "A novel noise reduction technology for switched reluctance motors," *IEEE PES General Meeting*, Pittsburgh, PA, USA, July 2008.
- [39] H. C. Lovatt and J. M. Stephenson, "Measurement of magnetic characteristics of switched-reluctance motors," in *Proc. Int. Conf. Electrical Machines*, pp. 465-469, Manchester, U.K., Sept. 1992.
- [40] A. D. Cheok, Z. Wang "DSP-Based automated error-reducing flux-linkagemeasurement method for switched reluctance motors," *IEEE Trans. Inst. Meas.*, vol. 56, no. 6, pp. 2245-2253, Dec. 2007.
- [41] "Acoustics- Determination of sound power levels of noise sources using sound pressure," *International Standard*, ISO 3744:1994(E).

- [42] P. Debiprasad, V. Ramanarayanan, "Mutual coupling and its effect on steady-state performance and position estimation of even and odd number phase switched reluctance motor drive," *IEEE Trans. Magn.*, vol.43, no.8, pp.3445-3456, Aug. 2007.
- [43] Y. Liu, P. Pillay "Improved torque performance of switched reluctance machines by reducing the mutual saturation effect," *IEEE Trans. Energy Convers.*, vol. 19, no.2, pp.251-257, June 2004.

# **APPENDIX A**

# SPECIFICATIONS OF THE EQUIPMENT

# A.1. Dimensions, Electrical and Magnetic Properties of the Test Motor

	Value	Units
Rated power	750	Watt
Rated speed	15.000	rpm
Operating Voltage	300	V
Rated Current	3	А
Number of phases	4	-
Number of stator poles	8	-
Number of rotor teeth	6	-
Phase coil turn number	320	turns/stator pole
Phase coils connection type	Two coils in series	-
Nominal Average Torque (T <sub>base</sub> )	1.0	Nm

Table 9 The specifications of the SRM used as the test motor (SR3).

Rotor outer diameter	38.6 mm
Stator outer length (thicker part)	120.4 mm
Stator outer length (thinner part)	111.4 mm
Stator core inner diameter	99.99 mm
Stator pole tip width	8.35 mm
Tapering angle	2.2 degree
Rotor tooth width	8.4 mm
Airgap length	0.325 mm
Rotor tooth depth	7.2 mm
Stator pole depth	34.37 mm
Shaft diameter	16.5 mm
Shaft length	250 mm
Core length	41 mm

Table 10 Measured physical dimensions of SR3.

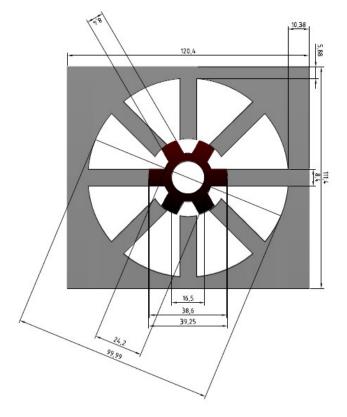


Figure 175 The cross-section and the measured physical dimensions of SR3.



Figure 176 The test motor (SR3) and the mechanical load.

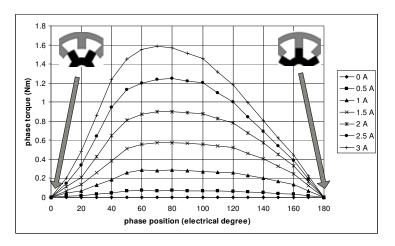


Figure 177 Measured static torque curves of SR3.

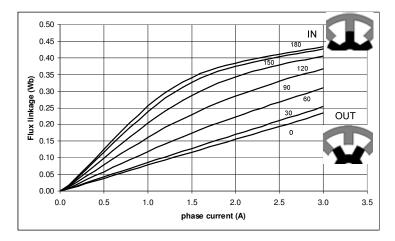


Figure 178 Measured flux-linkage characteristics of SR3.

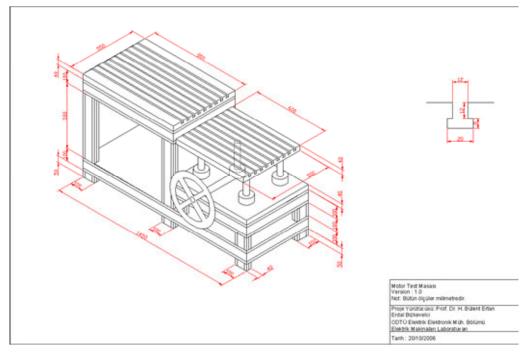


Figure 179 Dimensions of the test setup (All dimensions are given in mm).

# A.3 Other Test Equipment

Model	Description	Qty
Siemens <sup>®</sup> 1LA7 073 2AA	Induction machine (mechanical load)	1
Siemens <sup>®</sup> MM440 (11 kW)	Induction machine drive	1
Magtrol TM308	Torque transducer	1
Magtrol 6400A	Torque read-out	1
BK3-60-66	Coupling	2
E6C2-C Incremental encoder	Position encoder	1
dSPACE <sup>®</sup> 1104	Controller board	1

Table 11 Test equipment model numbers and descriptions.

### **APPENDIX B**

# CALCULATION OF THE ROTATIONAL INERTIA AND THE FRICTION CHARACTERISTICS OF THE DRIVE TRAIN

### **B.1 Rotational Inertia of the Drive Train:**

The inertia value of the SRM is calculated by its physical dimensions and material properties while the other test equipment inertia values are obtained from the manufacturer datasheets. The rotational inertia values of the test equipment are given in Table 12.

Item	Description	Qty	Rotational Inertia, J (kg.m <sup>2</sup> )	Method
SRM	Test Motor	1	5.23x10 <sup>-5</sup>	Calculation
Induction Machine (1LA7 073 2AA)	Mechanical Load	1	41x10 <sup>-5</sup>	Catalogue
Magtrol TM308	Torque Transducer	1	2.66x10 <sup>-5</sup>	Catalogue
BK3-60-66	Coupling	2	54x10 <sup>-5</sup>	Catalogue
E6C2-C Inc. Encoder	Position Encoder	1	$1 \times 10^{-6}$	Catalogue
Total			$157 \text{ x}10^{-5} \text{ kg.m}^2$	

Table 12 The rotational inertia values of the drive train components.

The rotational inertia of the test motor is calculated from the physical dimensions and material properties. For the sake of simplicity, the rotor is considered in three parts:

- 1. The motor shaft (Figure 180, region 1)
- 2. Cylindrical part of the rotor stack excluding the rotor teeth (Figure 180, region 2),
- 3. Rotor teeth, (Figure 180, dark sides of region 3),

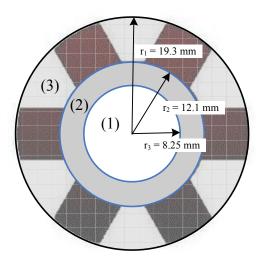


Figure 180 Three regions of the SRM rotor.

The total inertia of the rotor is the algebraic sum of the inertia values of these three parts.

Rotor shaft (Figure 180, region 1) is a solid cylinder and the inertia of this part about the central diameter is given as follows:

$$J_1 = \frac{1}{2} m_1 r_1^2 \tag{135}$$

Here  $m_1$  is the shaft mass. The shaft length of the test motor is 250 mm. By taking the shaft steel density as 7750 kg/m<sup>3</sup>, shaft mass can be calculated:

$$m_1 = \pi r_1^2 l_1 d_1 \tag{136}$$

Region 2 can be considered as an annular cylinder and the inertia about central axis is given as follows:

$$J_2 = \frac{1}{2}m_2\left(r_2^2 + r_1^2\right) \tag{137}$$

Where  $m_2$  is the mass of the annular cylinder:

$$m_2 = \pi \left( r_2^2 - r_1^2 \right) l_2 d_2 \tag{138}$$

Here *d* is the density of the laminated steel and taken as 7750 kg/m<sup>3</sup>. The stack length is taken as 41 mm.

The calculation of the rotor teeth inertia is achieved in two steps. First the inertia of region 3 is calculated by using (137) and then this result is multiplied by the area ratio between the teeth and the region 3:

$$J_{teeth} = \frac{1}{2} m_3 \left( r_3^2 + r_2^2 \right) \cdot \left( \frac{A_{teeth}}{A_3} \right)$$
(139)

The mass of the teeth is calculated as follows:

$$m_{3} = \pi \left( r_{3}^{2} - r_{2}^{2} \right) l_{3} d_{3} \cdot \left( \frac{A_{teeth}}{A_{3}} \right)$$
(140)

The total inertia of the rotor is obtained by the algebraic sum of these three components. By using these dimensions and formulation, total rotational inertia of the rotor is obtained as  $5.23 \times 10^{-5}$  kg.m<sup>2</sup>. The results are given in Table 13. The dimensions and the material properties are given in Table 14.

Table 13 The rotational inertia values of the SRM rotor components.

Part	Mass (kg)	Rotational Inertia, J (kg.m <sup>2</sup> )
Rotor shaft	4.14x10 <sup>-1</sup>	1.41x10 <sup>-5</sup>
Rotor cylinder (excluding rotor teeth region)	7.80x10 <sup>-2</sup>	8.36x10 <sup>-6</sup>
Rotor teeth	1.15x10 <sup>-1</sup>	2.98x10 <sup>-5</sup>
Total	6.52x10 <sup>-1</sup>	5.23 x10 <sup>-5</sup>

Dimension	Definition	Value	Unit
r <sub>1</sub>	Rotor bore radius	8.25x10 <sup>-3</sup>	m
r <sub>2</sub>	Rotor tooth bottom radius	12.1x10 <sup>-3</sup>	m
r <sub>3</sub>	Rotor outer radius	19.3 x10 <sup>-3</sup>	m
l <sub>1</sub>	Shaft length	$250 \text{ x} 10^{-3}$	m
$l_2, l_3$	Rotor stack length	41x10 <sup>-3</sup>	m
$d_1, d_2, d_3$	Shaft steel and laminated steel density	7750	kg/m <sup>3</sup>

Table 14 The dimensions and the material properties of the rotor.

### **B.2** Friction coefficients

During free deceleration of the drive train, the torque acting on the system originates from friction and windage losses. The braking effect of the losses can be used for the calculation of friction and windage loss coefficients of the drive train. In Figure 181, the deceleration characteristics of the system is given. At the beginning of the experiment, the motor is accelerated up to 2000 rpm and then the system is shut down. The speed versus time characteristics is recorded by the dSPACE<sup>®</sup> system and then exported to Matlab<sup>®</sup> workspace for fitting a polynom. The fitted curve equation is also shown in Figure 181. The differential equation valid for the deceleration period is given in (141). By using Matlab optimization toolbox, the friction coefficients of the system B<sub>1</sub> and B<sub>2</sub> are calculated. The equation obtain from this calculation and used in this study is given in (142).

$$0 = J \cdot \frac{d\omega}{dt} + B_1 \cdot \omega + B_2 \tag{141}$$

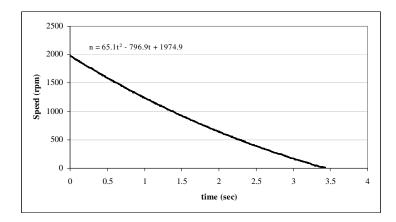


Figure 181 Free deceleration characteristics of the test motor and the fitted curve equation.

$$T_{f\&w} = 3.74.10^{-5}.n + 0.063 Nm \tag{142}$$

This equation then used for the verification of the solution. Substituting (142) into (141) the differential equation coefficients are obtained as follows:

$$0 = J \cdot \frac{d\omega}{dt} + 3.57 \times 10^{-4} \cdot \omega + 0.063$$
(143)

With the calculated coefficients and the initial conditions (143) is solved again. The solution obtained by simulation and the experimental results are shown in Figure 182. As it is seen from this figure, the differential equation solution and the experiment results are close to each other and the coefficients given in (142) can be used for the estimation of the friction and windage losses of the drive train.




Figure 182 The experimentally recorded and simulated deceleration characteristics.

# **CURRICULUM VITAE**

# PERSONAL INFORMATION

Surname, Name: Bizkevelci, Erdal Nationality: Turkish (TC) Date and Place of Birth: 26 April 1970, Erzurum Marital Status: Married Phone: +90 312 210 13 10 / 1158 Fax: +90 312 210 13 15 Email: erdal.bizkevelci@uzay.tubitak.gov.tr

# **EDUCATION**

Degree	Institution	Year of Graduation
MSc.	Gazi University Department of	1996
	Electrical and Electronics Engineering	
BS	Gazi University Department of	1992
	Electrical and Electronics Engineering	
High School	Erzurum Anadolu High School,	1988
-	Erzurum	

## WORK EXPERIENCE

Year	Place	Enrollment
1998 - Present 1993-1998	TUBITAK-UZAY	Chief Senior Researcher Research Assistant
1993-1998	Gazi University Electrical and Electronics Engineering	Research Assistant

## FOREIGN LANGUAGES

Advanced English

#### PUBLICATIONS

- 1. H. B. Ertan, E. Bizkevelci, B. Avenoğlu, "An induction motor design tool combining analytical and field solution techniques," in *Proc. ISEF*, 2001, Poland, pp.153-158.
- 2. H. B. Ertan, E. Bizkevelci, B. Avenoğlu, "An induction motor design tool combining analytical and field solution techniques," in *Proc. ICEMS*, 2001, Shenyang-China, Proceedings CD.
- 3. H. B. Ertan, E. Bizkevelci, B. Avenoğlu, "A design tool utilizing numerical field solution and analytical design and optimization techniques," in *Proc. ACEMP*, 2001, Turkey, pp.628-633.
- 4. H. B. Ertan, E. Bizkevelci, L.B. Yalçıner, "Measurement and calculation of leakage inductance and stray capacitance of high-frequency transformers," in *Proc. ELECTROMOTION*, 2003, Morocco, pp.120-125.
- 5. E. Bizkevelci, K. Leblebicioğlu, H. B. Ertan, "A sliding mode controller to minimize SRM torque ripple and noise," in *Proc. IEEE Internat. Symp. on Ind. Electron.*, 2004, France, pp.1333–1338.
- 6. H. B. Ertan, E. Bizkevelci, L. B. Yalçıner, "Measurement and prediction of parameters of high frequency transformers," in *Proc. ARWtr*, 2004, Spain, pp. 3-8.
- 7. E. Bizkevelci, K. Leblebicioğlu, H. B. Ertan, "A control strategy for noise reduction in switched reluctance motors," in *Proc. SAEM*, 2006, Macedonia.
- 8. E. Bizkevelci, H. B. Ertan, K. Leblebicioğlu, "Effects of control parameters on SRM performance: A parametric search," in *Proc. ACEMP*, 2007, Turkey, pp.276–281.
- 9. E. Bizkevelci, H. B. Ertan, K. Leblebicioğlu, "A novel noise reduction technology for switched reluctance motors," IEEE PES General Meeting, Pittsburgh, PA, USA, July 2008.
- 10. E. Bizkevelci, H. B. Ertan, K. Leblebicioğlu, "A sliding-mode control strategy for noise reduction in switched reluctance motors," *IEEE Trans. Ind. Electron.*, to be published.